

**Alma Mater Studiorum – Università di Bologna**

**DOTTORATO DI RICERCA IN**

**Chimica**

**Ciclo XXI**

**Settore Concorsuale: 03/A2**

**Settore Scientifico Disciplinare: CHIM/02**

**STUDY OF CERIA-BASED MATERIALS AND THEIR APPLICATION  
IN ELECTROCHEMICAL AND GAS-PHASE CATALYSIS**

**Presentata da: Verlato Enrico**

**Coordinatore Dottorato:**

**Prof. Aldo Roda**

**Supervisore:**

**Prof. Francesco Paolucci**

**Co-supervisore:**

**Dr. Marco Musiani**

**Esame finale anno 2019**

## Preface

This thesis is submitted in partial fulfilment for the degree of Doctor of Philosophy (PhD) in Chemistry at the University of Bologna (XXXI doctoral cycle). The majority of work reported here was carried out at the Institute of Condensed Matter Chemistry and Technologies for Energy (ICMATE) of National Research Council of Italy (CNR) in Padova and at EMFM (Electrochemistry of Molecular and Functional Materials) Electrochemistry Laboratory of the Chemistry Department “Giacomo Ciamician” under the supervision of Prof. Francesco Paolucci and Dr. Marco Musiani.

Part of the research reported in chapter 1, in particular regarding BDD electrodes preparation, was conducted in collaboration with the group of Prof. Yasuaki Einaga, during my stage at KEIO University, in November-December 2017, funded by a formation program of ICMATE-CNR.

The results obtained on gas-phase catalysis applications, reported on chapter 2, were achieved in collaboration with the Institute for Research on Combustion (IRC) of CNR in Napoli. In particular, Dr. Stefano Cimino performed all the catalytic tests on samples that I have prepared and characterized. Thanks to this profitable collaboration, we got inspiration for exploring ceria potentiality in the electrocatalysis of CO<sub>2</sub> reduction. The ICMATE-IRC collaboration was financially supported by the project “Bioenergia efficiente - WP 2 Tecnologie catalitiche per il risparmio energetico in impianti di piccola taglia (civili e industriali)” as a part of MiSE-CNR Agreement on National Electrical System between Italian Ministry for Economic Development (MiSE) and CNR.

The study of CO<sub>2</sub> reduction on copper-based nanocarbons, reported in chapter 3, was inspired by an ongoing collaboration with the group of Dr. Alain Penicaud of CNRS in Bordeaux. In particular, the syntheses of these materials were performed by Dr. Ferdinand Hof.

## Abstract

This thesis is focused on the preparation of nanostructured ceria catalysts with an electrochemical approach and on their use in reactions relevant to environmental issues, like CO<sub>2</sub> electrochemical reduction and low temperature catalytic combustion, in the gas phase. Supports with totally different compositions and geometries were used for the preparation of electrocatalysts and gas-phase catalysts, but in all cases ceria was cathodically deposited via an electroprecipitation process triggered by local pH increase.

To study CO<sub>2</sub> reduction, ceria was cathodically deposited on boron-doped diamond, obtaining control of its morphology and composition, both crucial aspect in ceria catalytic applications. Promising efficiency toward formate production was demonstrated, at very low overpotential.

To produce catalysts for low-temperature combustion of methanol and CO oxidation, platinum and ceria were sequentially deposited onto FeCrAlloy 3D foams, the support currently used in industrial structured catalysts.

To extend the scope of the studies on CO<sub>2</sub> reduction, copper oxide graphenide materials were investigated and compared to ceria. These materials were shown to effectively reduce CO<sub>2</sub> to formate, exhibiting good stability and resistance to poisoning. Their performance matched those of the best catalysts described in the literature.

# Table of Contents

Preface

**Abstract**

**Table of Contents**

List of Symbols and Abbreviations

**INTRODUCTION**

**I.1. A general picture: CO<sub>2</sub> and greenhouse gases**

**I.2. CO<sub>2</sub> conversion**

I.1.1 CO<sub>2</sub> electrochemical reduction

I.1.2 Low temperature catalysis

**I.3. Why Ceria?**

**I.4. Bibliography**

**CHAPTER 1: CO<sub>2</sub>RR on ceria**

**1.1. Introduction & motivations**

**1.2. Electrode preparation**

1.2.1. Support Choice: boron doped diamond

**1.3. Characterization of CeO<sub>2</sub>-BDD electrodes**

1.3.1. Morphology

1.3.2. Phase characterization

**1.4. CO<sub>2</sub> electrochemical reduction on Ceria-BDD electrodes**

**1.5. Conclusions & Perspectives**

**1.6. Bibliography**

**CHAPTER 2: ceria for gas phase catalysis**

**2.1. Introduction**

**2.2. Preparation of Pt-Fecralloy, CeO<sub>2</sub>-Fecralloy and CeO<sub>2</sub>-Pt-Fecralloy catalysts**

2.2.1 Preliminary experiments

2.2.2 Pulsed deposition of Pt onto Fecralloy

2.2.3 Cathodic deposition of CeO<sub>2</sub> onto Fecralloy

2.2.4 Pt loading and Pt surface area in Pt-Fecralloy and CeO<sub>2</sub>-Pt-Fecralloy catalysts

**2.3. Catalytic combustion of methanol on Pt-Fecralloy, CeO<sub>2</sub>-Fecralloy and CeO<sub>2</sub>-Pt-Fecralloy**

## **2.4. CO oxidation activity**

## **2.5. Thermal stability**

2.5.1. Characterization of used CeO<sub>2</sub>-Pt-Fecralloy catalysts

## **2.6. Conclusions**

## **2.7. Bibliography**

# **CHAPTER 3: CO<sub>2</sub>RR on Cu-based graphenide**

## **3.1. Introduction**

## **3.2. Preparation**

## **3.3. Characterization**

## **3.4. Study of electrochemical CO<sub>2</sub>RR**

## **3.5. Conclusions & Outlooks**

## **3.6. Bibliography**

# **APPENDIX**

## **Appendix Chapter 1**

A.1.1. Electrodes preparation details

A.1.2. Characterization techniques

A.1.3. Electrochemical Cell for the study of CO<sub>2</sub>RR

## **Appendix Chapter 2**

A.2.1. Preparation and characterization of catalysts

A.2.2. Methanol combustion tests

A.2.3. CO oxidation tests

## **Appendix Chapter 3**

A.3.1. Cu(nP)/nC preparation

A.3.2. Characterization

A.3.3. Electrochemical CO<sub>2</sub> reduction

# **ACKNOWLEDGMENTS**

## List of Symbols and Abbreviations

GHG	Greenhouse Gas
GWP	Greenhouse Gas
CO <sub>2</sub> RR	CO <sub>2</sub> Reduction Reaction
HER	Hydrogen Evolution Reaction
P(CO <sub>2</sub> )	CO <sub>2</sub> Partial Pressure
VOC	Volatile Organic Compound
LDH	Layered Double Hydroxides
HT	Hydrotalcite type
MRI	Magnetic Resonance Imaging
CNT	Carbon Nanotube
BDD	Boron Doped Diamond
CVD	Chemical Vapour Deposition
SCE	Saturated Calomel Electrode
CV	Cyclic Voltammetry
LSV	Linear Sweep Voltammetry
SEM	Scanning Electron Microscope
EDX	Energy-dispersive X-ray spectroscopy
HR-TEM	High-Resolution Transmission Electron Microscope
FTT	Fast Fourier Transform
XRD	X-Ray Diffraction
XPS	X-Ray Photoelectron Spectroscopy
NO <sub>x</sub>	Nitrogen Oxides
ICP-MS	Inductively Coupled Plasma Mass Spectrometry
Ag AgCl	Silver\Silver chloride reference electrode
RHE	Reversible Hydrogen Electrode
Hg HgO	Mercury\Mercury Oxide reference electrode
GIC	Graphite Intercalation Compound
AFM	Atomic Force Microscopy
EQCM	Electrochemical Quartz Crystal Microbalance
EIS	Electrochemical Impedance Spectroscopy
TON	Turnover Number

TOF	Turnover frequency
F.E.	Faradaic Efficiency
$Q_{dep}$	Deposition Charge
SHE	Standard Hydrogen Electrode
FeCrAlloy	Iron Chromium Aluminium alloy
$E_{dep}$	Deposition potential
PB	Phosphate buffer solution
CB	Carbonate buffer solution

# INTRODUCTION

## I.1 A general picture: CO<sub>2</sub> and greenhouse gases

Human impact on climate change is widely recognized as a worldwide issue of unsurpassed importance [1] Global warming, the first direct signal of climate change, is a direct consequence of increasing greenhouse gases (GHG) concentration in the atmosphere [2]. These gases, because of their long atmospheric lifetime (decades, centuries), accumulate in the atmosphere and build-up in concentrations. Increments are evident and they are evenly distributed across the globe; their measurement, looking to instrumental observations in bubbles of air trapped in ice cores and since 1958, directly in air samples, simplify the global monitoring (Fig.1) [3-9].

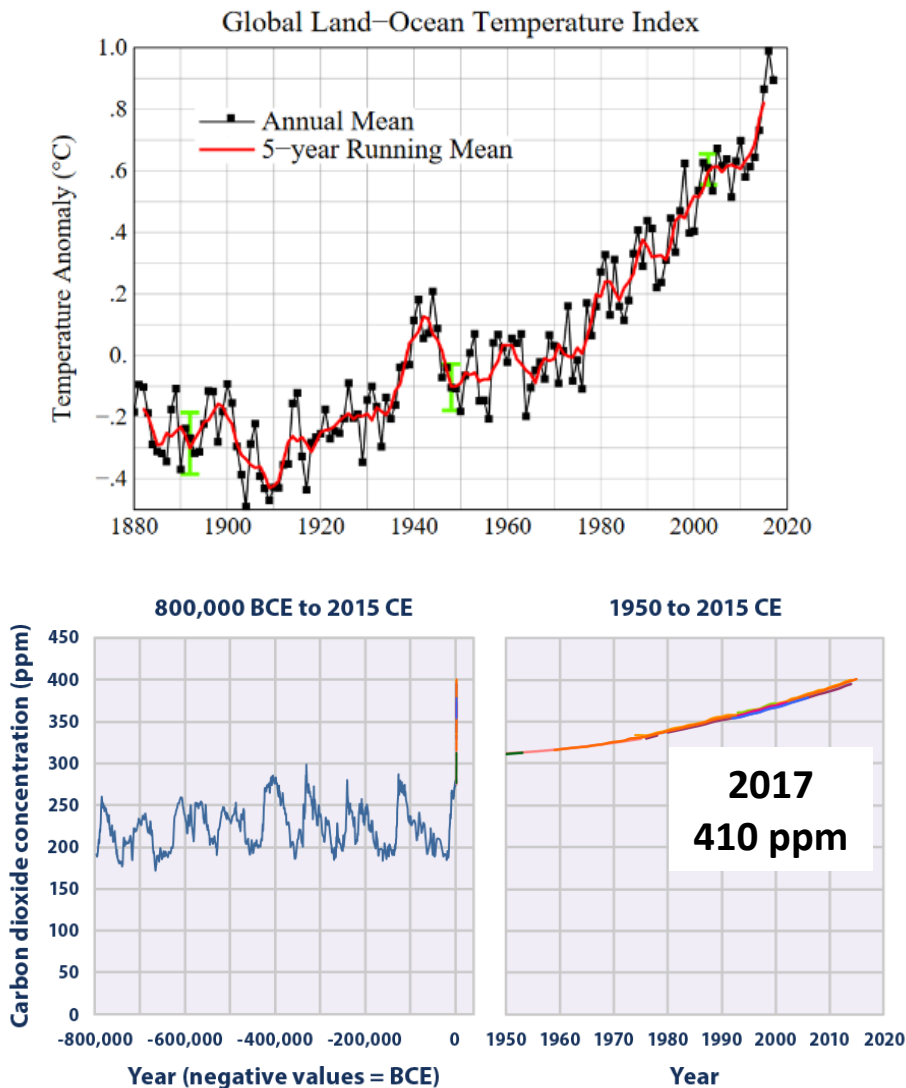


**Fig.1.** The global temperature trend, updated through 2016 [2] (top) and global atmospheric concentration measurements for carbon dioxide (bottom) [3-9]

Different GHGs variously affects global warming; they differ from each other for their ability to absorb energy (their "radiative efficiency"), and for how long they stay in the atmosphere (also known as their "lifetime"). United States Environmental Protection Agency (EPA) developed a Global Warming Potential (GWP) index that evidences emissions effects for different gases. Looking to GWP if CO<sub>2</sub> has an index of 1, methane is reported to have a factor around 30. This evidences that reducing total emissions, and not just concentrate on a single gas, is mandatory to prevent catastrophic consequences. [10-11]

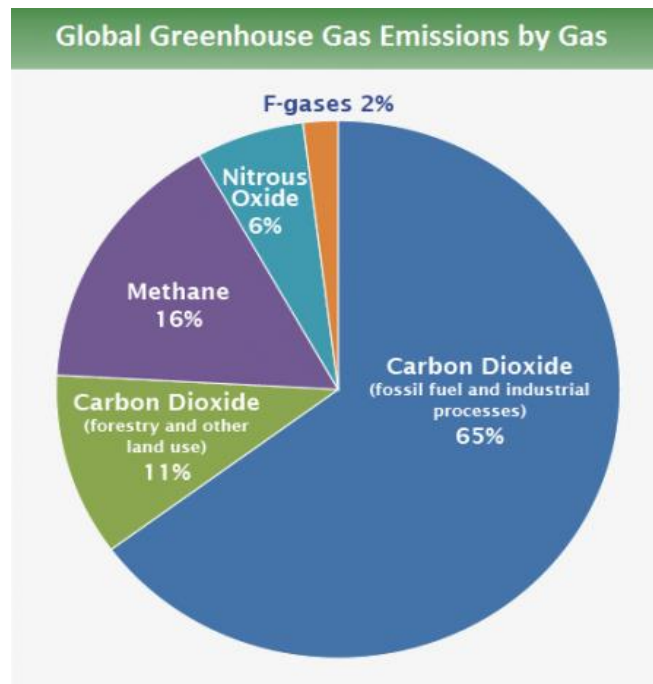


**Fig.2.** Distribution of key greenhouse gases emitted by human activities based on global emissions from 2010. [10]

Internationally, almost all the countries representing both developed and developing countries, decided to set objectives and actions to invert the tendencies and mitigate the effects of climate change by signing what is called the "Paris agreement" [12,13]. Crucial points of the document are:

"This Agreement, in enhancing the implementation of the Convention, including its objective, aims to strengthen the global response to the threat of climate change, in the context of sustainable development and efforts to eradicate poverty..."

"Holding the increase in the global average temperature to well below 2 °C above pre-industrial levels and to pursue efforts to limit the temperature increase to 1.5 °C above pre-industrial levels [...]"

"Parties aim to reach global peaking of greenhouse gas emissions as soon as possible [...] and to undertake rapid reductions thereafter in accordance with best available science..."

“Parties, noting the importance of technology for the implementation of mitigation and adaptation actions under this Agreement and recognizing existing technology deployment and dissemination efforts, shall strengthen cooperative action on technology development and transfer.”

Even before the publication of this agreement, most efforts were devoted to limit the concentration of greenhouse gas in the atmosphere by increasing the efficiency of fossil fuels and biofuels usage [14,15] and by capturing and/or converting CO<sub>2</sub> to fuels easy to store [16]. Both these processes will play a fundamental role to sustain the transition to a world powered by renewable energy sources. This transition predict to cover a big lapse of time before humanity will be able to change primary energy sources switching to non-fossil fuels. Therefore, in addition to increase the number of installations of renewable energy sources in different areas of the planet, there are great challenges in “recycling” carbon dioxide and in increasing the utilization efficiency of traditional fuels while reducing their impact on environment. Since fuels utilization, through catalytic combustion or transformation into energy vectors, is a mature technology, general effort concentrate on increasing efficiencies of processes including discovering new approaches to the preparation of materials involved. We also know, that traditional energy sources are limited and global reserves are difficult to estimate [17]; carbon dioxide is a cheap and abundant source of carbon and could be converted to important compounds, to be used in industrial processes as well as fuels [18,19]. Conversion can be performed by electrolysis powered by green or renewable energy sources, for example wind, tidal, solar or the so-called “blue energy” systems. Although carbon dioxide “recycling” can be performed by sequestration and storage, with biochars and by absorption, mimicking natural photosynthesis represents the most scientifically challenging avenue [20]. This thesis focus on both, the direct reduction of CO<sub>2</sub> and the enhancement of efficiency of fuels.

## **1.2 CO<sub>2</sub> conversion**

As a part of “Carbon Cycle”, plants transform radiant energy produced by sun into chemical energy in the form of sugars, starches, and other forms of organic compounds from carbon dioxide and water. Land plants through photosynthesis fix ca. 450 billion tonnes per year, a value affected by climate variables and vegetation properties. Just a small part is long term fixed, the most of the carbon is returned to cycle during respiration, leaf or wood decomposition and uncontrolled fires. In most cases, photosynthesis has slow kinetics that lead to low efficiencies; additionally, also due to strong deforestation, carbon fixation from plants is not high enough to balance CO<sub>2</sub> anthropogenic annual emissions, which is around 24 billion tonnes. The industry uses approximately 120 million tonnes CO<sub>2</sub> per year, which correspond to only 0.5% of the total anthropogenic CO<sub>2</sub> emissions. The usage can be divided into applications that take advantage of its physical

properties and chemical application. The list of “physical” application includes beverage industry, enhanced oil recovery, applications in reactions as solvent, use as a safe, inert or protective gas and as a fire extinguisher. As a solid, CO<sub>2</sub>, can be used for refrigeration to substitute CFCs. CO<sub>2</sub> chemical applications include the conversion into chemicals such as urea, salicylic acid, organic and inorganic carbonates, pigments and methanol synthesis additive [16,21].

In principle, CO<sub>2</sub> is also an abundant and renewable carbon source but its use is limited by the fact that it is a molecule in the most oxidized form which is why it is quite unreactive. High energies are required to transform CO<sub>2</sub> into other chemicals. Scheme 1 [21] summarize some of the possible compounds that can be produced through different chemical, physical or biological processes.

CO <sub>2</sub> transformations	{	(1) Chemical	Non-hydrogenative	Carbonates, carbamates, etc.
			Hydrogenative	Hydrocarbons, MeOH, EtOH, etc.
		(2) Photochemical		CO, HCO <sub>2</sub> H, CH <sub>4</sub>
		(3) Electrochemical		CO, HCO <sub>2</sub> H, MeOH
		(4) Biological		EtOH, Sugar, CH <sub>3</sub> CO <sub>2</sub> H
		(5) Reforming		CO + H <sub>2</sub>
	(6) Inorganic		Carbonates: M <sub>2</sub> CO <sub>3</sub>	

**Fig.3.** Different process for CO<sub>2</sub> recovering [21]

Electrochemistry, is widely considered an across-the-board science, thanks to its capability to supply several useful tools that spread from biological fields to energetics to environmental monitoring. Electrochemical conversion of CO<sub>2</sub> represents one of the most interesting and promising approaches to the “CO<sub>2</sub> issue”; its main advantages are:

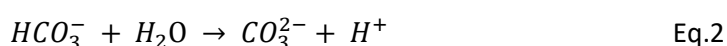
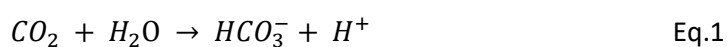
- controlling electrode potentials and cell temperature we can control the process;
- in most cases it’s a green process, where there is no need of harmful or polluting reagents;
- other industrial processes like water electrolysis can borrow their electrochemical apparatus for a modular approach or an easy scale-up;
- the electricity used to drive the process can be obtained from renewable sources that include solar, wind, hydroelectric, geothermal, tidal, and thermoelectric processes.

The last point entails that no CO<sub>2</sub> production is involved if the process is coupled with a green energy source; this aspect and the fact that CO<sub>2</sub> electrochemical reduction lead to useful compounds are probably the edges over other, still interesting, approaches like sequestering and storage or biological conversion.

### 1.1.1 CO<sub>2</sub> electrochemical reduction

As mentioned before, the chemical reactivity of CO<sub>2</sub> is low. Although its reduction potentials are not very negative compared to other important electrochemical reactions, e.g. hydrogen evolution reaction or oxygen reduction reaction, it is necessary to employ a catalyst to increase the reaction rate. Electrocatalysis play a fundamental role to reach, by means of lower energy routes, higher current densities close to equilibrium potential [23]. In case of CO<sub>2</sub>RR electrocatalysts require the formation of bonds between electrode surface and reagents, even so this interaction does not guarantee to obtain desired products with a reasonable yield. For example, electrochemical reduction over carbon electrodes usually gives a CO<sub>2</sub> radical anion that decompose to CO and carbonate, in a really high energy process. On the other hand, active metals, through surface adsorption over active sites, can directly reduce CO<sub>2</sub> to hydrogenated products at lower voltage because of the electrocatalytic effect [22]. There are several parameters that can be compared to evaluate different electrocatalysts: exchange current densities, Tafel slope, onset potential, TOF, current stability and so on. In general, a good electrode for CO<sub>2</sub>RR should be stable, very efficient (possibly toward a single product) and give product with high rate at low overpotentials. Despite many reports on electrochemical CO<sub>2</sub> reduction during last years many challenges remain [20,24-26]. Primarily, significant improvements are needed to fight the slow kinetics of reaction and the low efficiency of the process due to the parasitic HER. Synthetically we can say that researcher widely recognize that the biggest challenge in CO<sub>2</sub> electroreduction is the tailoring of high efficient electrocatalysts [27-28].

There are several variables that must be addressed when approaching electrochemical CO<sub>2</sub> reduction. For example, various electrolyte solutions are employed for CO<sub>2</sub> electrolysis, from water to organic solvents to ionic liquids with low or high pressure of CO<sub>2</sub> [22]. Since CO<sub>2</sub> cannot be present in basic aqueous solutions, its reduction has been studied with neutral to acidic solutions; pH strongly influences concentration of species involved in CO<sub>2</sub> dissolution (Fig.4):



In a buffered solution equilibria become more complicated; some studies reported how pH of buffering solutions can affect reaction pathways and the following products distributions [22]; however, using a buffered solution helps maintaining a stable pH value that ,especially for prolonged electrolysis, limits the expected local alkalisation close to the electrode surface. Most of recent fundamental research is performed in carbonate buffer, and with a CO<sub>2</sub> dissolved maximum concentration of ca 33 mM. To give an idea on how important the choice of electrolyte composition and concentration are, we report below a table

relating pH of solutions with different carbonate concentrations and under a  $P(\text{CO}_2)$  of 1 atm ( table 1[23]) and the speciation diagram of carbonate species[29].

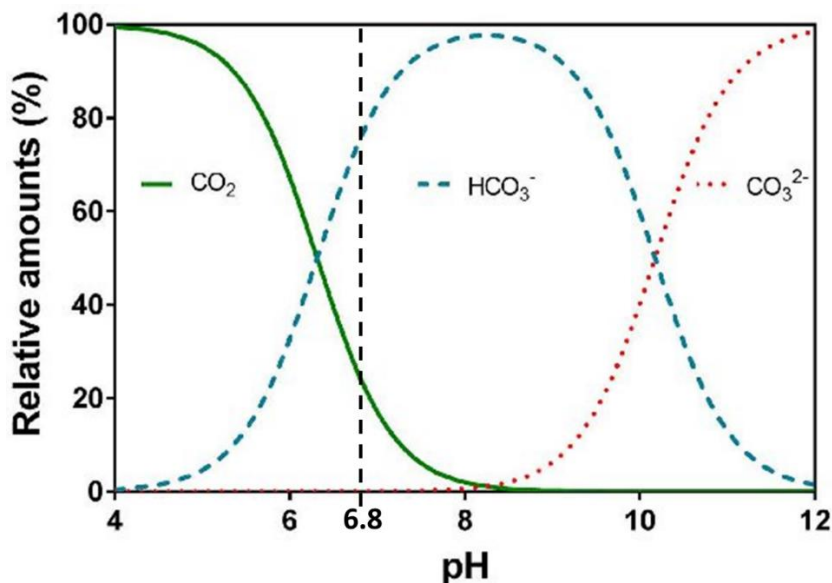


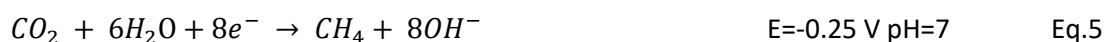
Fig.4. Relative speciation (%) of carbon dioxide, bicarbonate, and carbonate in water as a function of pH [29].

Table 1. pH of buffered solution made with reported concentration of bicarbonate saturated with  $\text{CO}_2$ .

**Values of pH of Solutions of Given Activity  $[\text{HCO}_3^-]$  under  $P(\text{CO}_2) = 1 \text{ atm}$**

$[\text{HCO}_3^-]/ \text{mol dm}^{-3}$	1	0.5	0.1	0.05	0.01
pH of the solution	7.82	7.52	6.82	6.52	5.82

Electrochemical reduction of  $\text{CO}_2$  can proceed through two-, four-, six-, and eight-electron reduction pathways in water solution; standard reduction potentials (calculated at pH=7) of semi-reactions leading to different products are the reported below:



These values, estimated from thermodynamic data, evidence how CO<sub>2</sub> standard potentials are generally quite negatives and they lay in the same region of HER, that is the main competitive reaction for experiment performed in water. This, indirectly confirm how kinetics can be considered the main limitations of the process. In alternative to direct electrolysis, homogeneous electrocatalysts can be used but, even if less prone to poisoning by electrolyte impurity, they have stability and durability issues, and moreover some systems use organic solvents that are not considered “green” [20]. Another big limitation of different catalysts is the wide distribution of products obtained during prolonged electrolysis. In most cases, catalysts give a mix of products that have to be separated to be used. Actually only few catalysts produce with high efficiency a single compound but they are limited by the high overpotential required or by their poor resistance to poisoning by solution impurities [30]. Usually, classification of different catalysts is related to principal product generated but there are major differences in potentials applied to reduce CO<sub>2</sub> amongst these materials. Metals, in particular transition metals, are the most studied electrodes for CO<sub>2</sub> reduction. They can be approximatively divided, with some exceptions, into two main categories: CO oriented and formate oriented metals. The first group includes Cu, Au, Ag, Zn, Pd, Ga, Ni, and Pt and the second group includes Pb, Hg, Tl, In, Sn, Cd, Bi. Periodic table below can schematically represent products distribution for catalysts within the periodic table of elements [20].

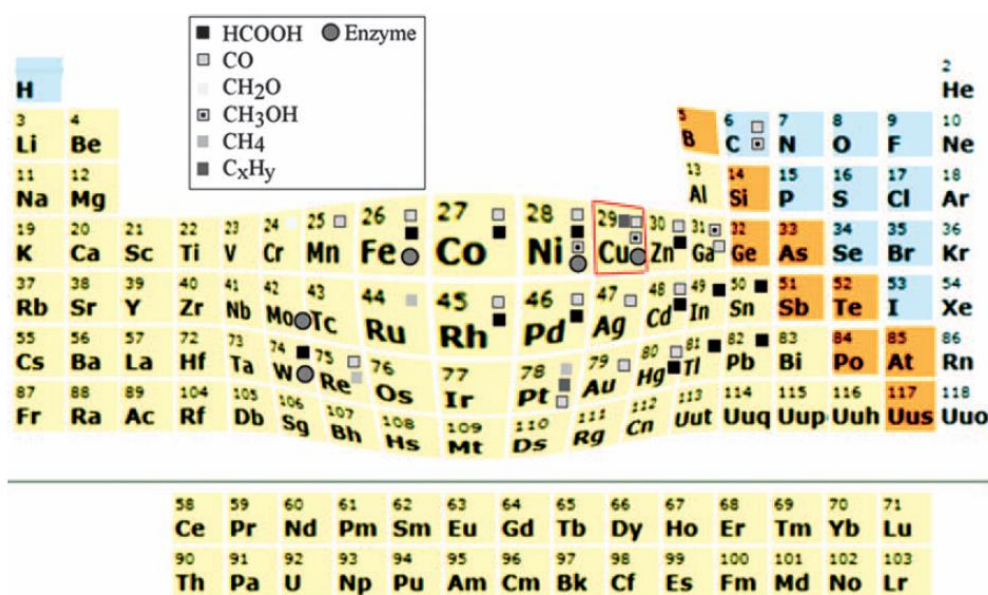
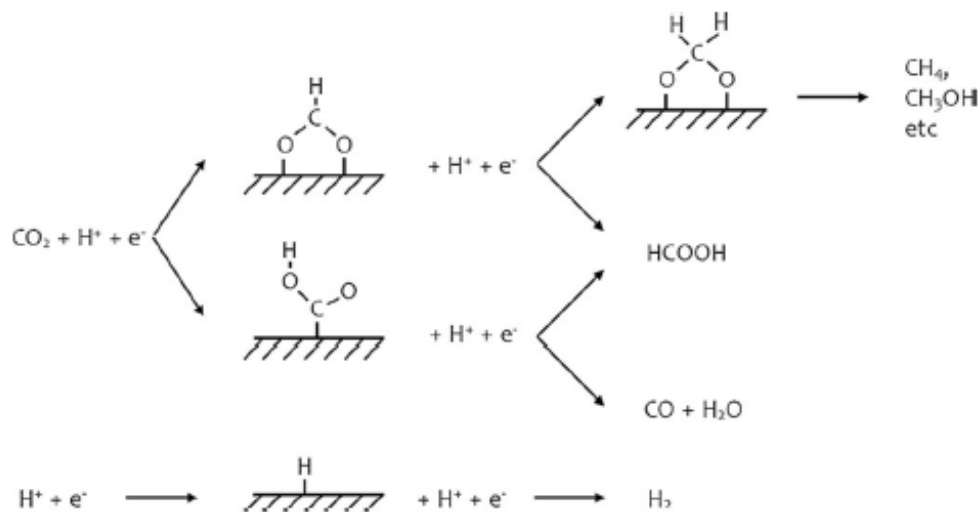


Fig.5. Schematic overview of CO<sub>2</sub> reduction catalytic activity across the periodic system of elements [20].

Often CO<sub>2</sub>RR proceed through the formation of two intermediates, a carboxyl (COOH\*) and a formate (HCOO\*) species. Considering reaction pathways, the first electron reducing CO<sub>2</sub> leads to a formation of either the formate (HCOO\*) or carboxyl (COOH\*) species. Both intermediates, further reduced, can give

formic acid but formate intermediate species can give also biformate ( $\text{H}_2\text{COO}^*$ ) and carboxyl adsorbed species can generate CO [27]. Always as a side reaction, contributing to reduce faradaic yield, there is HER. Since chemisorption energies of  $\text{COOH}^*$  and  $\text{H}^*$  are strongly linearly correlated, metals that produce selectively formic acid usually take a pathway through the adsorption of a  $\text{HCOO}^*$  species as schematically represented below (Fig.6). On the contrary, Ni, Pt and other platinum family metals that strongly adsorb CO on the electrode surface, prevent further reduction of  $\text{CO}_2$  enhancing efficiency toward HER [31].



**Fig.6.** Possible reaction pathways for the electroreduction of  $\text{CO}_2$  (top), and the competing hydrogen evolution reaction (bottom).

### 1.1.2 Low temperature catalysis

As stated in 1.0, contributing to greenhouse emissions there are, in addition to  $\text{CO}_2$ , methane and  $\text{N}_2\text{O}$ ; they have, respectively a GWP 28-36 and 265–298 times higher than that of  $\text{CO}_2$ . Moreover, CO and  $\text{NO}_2$  produced by transportation and fuels combustion contribute to particulate formation and directly affects air quality causing health disease and ecological effects (acid rains). The strategy that will lead to a world powered by renewable energy sources should include a progressive elimination of fossil fuels. During the transition period that we are already living, their utilization must be as efficient and clean as possible. Catalytic combustion of fuels generates much lower amounts of pollutants than small-scale flame combustion systems. For example, nitrogen oxides production is virtually zero. A successful example of catalysis devoted to environmental protection is the large-scale application of three-way-catalysts in automotive catalytic converters [32].

Methanol, together with ethanol, formic acid and other small molecules, is a promising energy feedstock. The reason is that, as a liquid at room temperature, it is easy to store and its combustion is considered clean, in particular for small-capacity power generation [33-36]. Methanol catalytic combustion at low temperature

can be sustained stably over a wide range of fuel/air ratios with ultra-low emissions, in contrast to conventional small scale flame combustion systems that have some intrinsic limitations on flame stability and pollutants formation. Pt-based nanostructured catalysts are considered the catalysts of choice for the deep oxidation of methanol either for power generation or for VOC destruction [37-39]. In general ceramic phases, like  $\gamma$ -Al<sub>2</sub>O<sub>3</sub>, promote the dispersion of the active noble metal phase. However, the deposition of a thin film of the ceramic phase, called washcoating, can be challenging; both a firmly anchorage and a uniform deposition must be achieved because they are of paramount importance in order to guarantee long catalyst durability and avoid pore blocking and additional pressure drops [40].

Recently some simple and innovative preparation methods, which take advantage of the metallic nature of Fe-c alloy support, have been proposed. Electrochemically induced precipitation, electrodeposition and spontaneous deposition through a galvanic displacement reaction have been shown capable to form small, well-dispersed and homogeneously distributed noble metal particles strongly interacting with the support. Electrodeposition is an interesting tool widely employed to modify 3D metallic foams depositing thin layers of metal oxides and hydroxides, as well as organoceramics and the so called layered double hydroxides (LDH)[]. Base generation deposition was first proposed by Switzer to prepare ceramic oxide films and powders [41]. Some of these materials, hydrotalcite-type compounds (HT), were successfully used to modify Fe-c alloy or Nickel foams for reforming and partial oxidation applications [42-44]. In fact, the electro-induced precipitation is very effective to coat metallic supports with HT-type materials. Unlike precipitation methods, where precipitation take place not only on the surface of the structured support but also in the bulk of the solution, with the electrochemical method the pH increases quickly near the surface of the support due to the reduction of nitrate, oxygen and water under a cathodic polarization. This technique is highly recommended to modify conductive 3D support in order to reach a good control of deposition. In addition, for some processes, for example for CO oxidation, the presence of a porous washcoat layer is not mandatory, since occurring under diffusion limitations. When a fair dispersion of the catalyst can be achieved and the active phase is not lost from/in the support, direct electrodeposition of active noble metal can be used as simple single step preparation.

### **I.3 Why Ceria?**

Heterogeneous catalysts employed for reactions taking place at solid/liquid interfaces (e.g. electrochemical processes), or at solid/gas interfaces (e.g. catalytic oxidations or reductions) share some common requirements. They must have a strong activity, resulting from an appropriate choice of morphology, size and nature of catalytic active phases and a good stability to grant a long service life. Cost, in terms of raw material, chemicals for preparation and conditioning (e.g. calcinations or thermal activation), determine if a process is accessible. Further requirement, specific to electrocatalysts, is a high electrical conductivity, whereas a strong resistance to degradation at high temperature and to thermal shocks is mandatory for catalysts for catalytic combustion or catalytic partial combustion.

Noble metals are the elements with the higher catalytic activity in most important electrochemical and gas-phase reactions, but they are very expensive and mining operation usually are linked to grave contamination of water sources and soil, human health impacts, and human rights abuse. However, using noble metal nanoparticles, that have an intrinsic large surface/volume ratio, or diluting by using noble metal and non-noble metal alloys are the only approaches to reduce the catalysts cost, still preserving, and even enhancing, their activity. Find alternative cheap catalysts to substitute noble metals or use co-catalyst that can enhance activity or stability of established materials is an approach that spreads over different catalysis-related research fields [45-48].

Cerium is the most abundant rare earth element and is not included into what is called “critical rare earths” category [49]. It is about as common as copper and its cost has decreased during last years. Cerium is the easiest lanthanide to extract from its minerals and as all rare earth elements, nowadays, it is crucial for a number of key technologies including: lasers, battery electrodes, magnets, MRI contrast agents, catalysts, uses in alloys, etc...

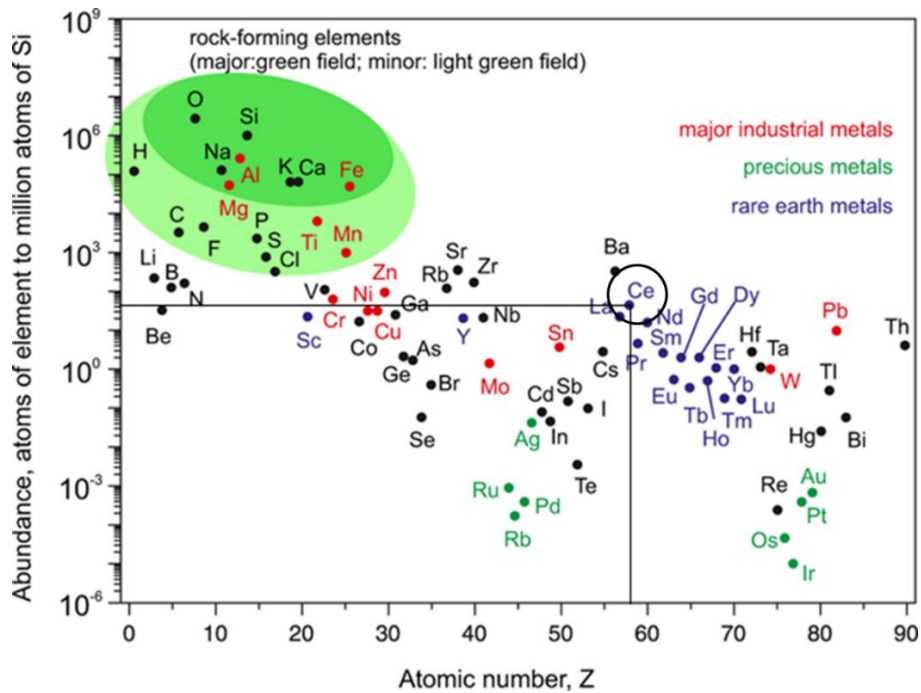


**Fig.7.** Abundance (atom fraction) of the chemical elements in Earth's upper continental crust as a function of atomic number, rare earth elements labelled in blue. Ceria position is highlighted by a black circle and its projection on axes. [49]

The most studied cerium compound is cerium dioxide, also called ceria. It is a pale yellow/white powder obtainable through calcination of a cerium precursors (oxalate or hydroxide), its common crystal structure is a fluorite-type face centred cubic.

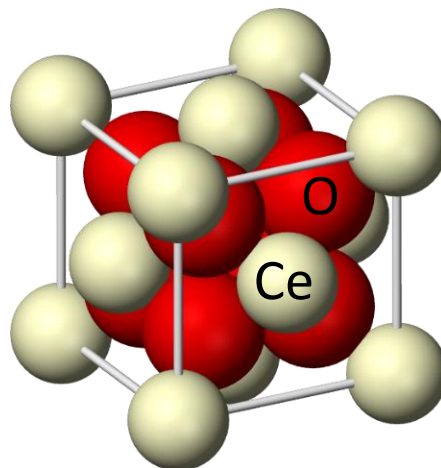


**Fig.8.** 3D representation of a ceria cubic crystal unit cell.

It is known that ceria forms, in a reducing environment, oxygen-deficient phases with nonstoichiometric CeO<sub>2-x</sub> oxides, x it's in between 0 and 0.5 [50]. In spite of the high oxygen depletion, ceria maintain its fluorite structure, and is easily reoxidised in oxidative conditions. One of the main consequences of this oxygen

deficiency is the capability to adsorb molecular oxygen on vacancies and to form radicals, called superoxides, that are fundamental intermediates in oxidation reactions. In the presence of a strong metal-ceria interaction, ceria can also chemisorb large amounts of  $H_2$  [51].

Ceria is a ubiquitous compound that can be found on literature regarding chemistry, material science, physics and even medicine. Most of literature regarding ceria-based materials is focused on energy and environmental processes, and the number of paper published every year is constantly increasing (Fig.9).

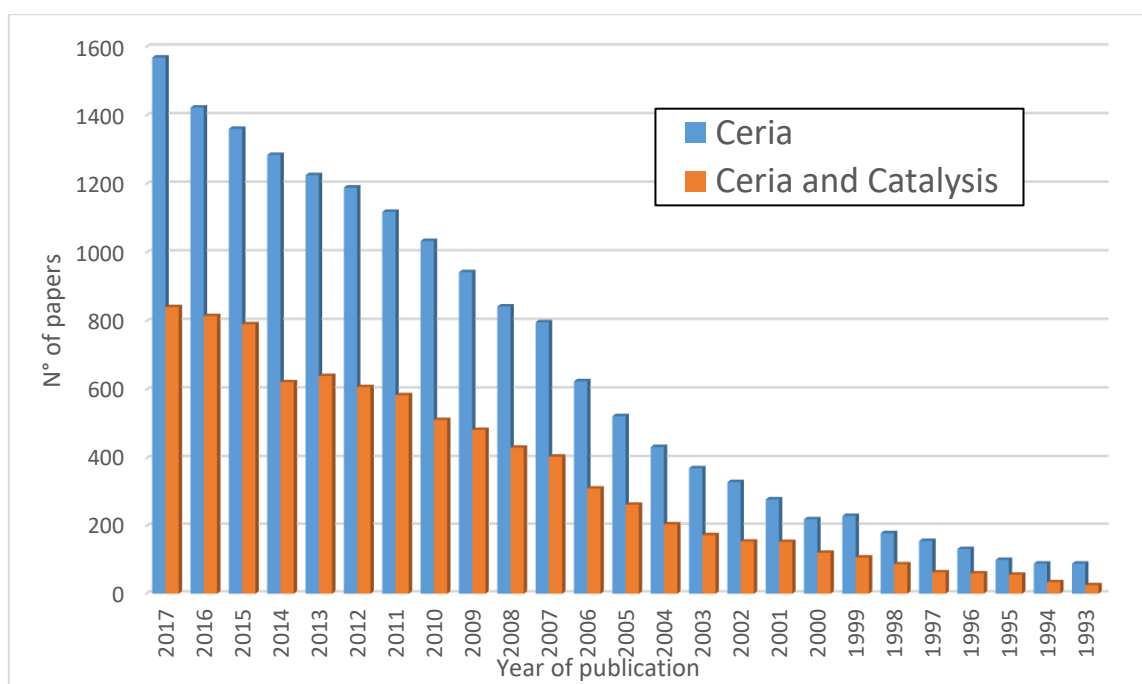


**Fig.9.** Histogram of number of publications on ceria (blue bars) and publications on ceria associated with catalysis (orange bars) from 1993 to 2017 (Source: Web of Science, October 2018).

Ceria-based materials are well known as catalysts or promoters for many heterogeneous catalytic applications. They have been used for oxidation reactions (CO, hydrocarbons, organics...), hydrogenation reactions (CO +  $H_2$ , organic compounds), elimination of SO and NO and in automotive exhaust catalysts [52,53]. Most of its catalytic properties are related to the lattice ion mobility and redox properties of Ce(III)/Ce(IV) system, together with the formation of adsorbed superoxides with high oxidizing power. Only a minor part of literature regarding ceria is focused on processes for low temperature electrocatalytic applications. Especially there are several papers describing the preparation of Pt-Ceria materials and their use as anodes for the electrochemical oxidation of alcohols in direct alcohol fuel cell applications [54-59]. To the best of our knowledge activity of electrochemically prepared Ceria toward  $CO_2$  electrochemical reduction was never reported.

Ceria can be prepared in several different methods that can be roughly divided in techniques to produce powders and techniques to deposit films [60]. Cerium oxide powders preparation methods include: sol-gel, hydrothermal, chemical homogeneous precipitation, thermal decomposition and electrochemical synthesis. For film deposition the list includes: chemical vapour deposition, physical vapour deposition, ion assisted beam deposition, electron beam deposition, molecular/atomic beam epitaxial, sol-gel methods, screen printing and liquid phase epitaxy and precipitation techniques. Other techniques employed to prepare film from solution or suspensions are: dip coating, spin coating, spray coating and electrophoresis. Electrochemical deposition can be used for both, powder or thin film preparation, but it became lately very attracting for the film deposition thanks to its intrinsic characteristics: mild temperature and pressure operational conditions (usually standard conditions are employed), easy control of film thickness and high purity. Nevertheless, calcination was always considered a necessary step to control ceria oxygen stoichiometry and morphology, probably due to homogeneity issues.

Ceria can be electrodeposited anodically [61,62] or cathodically [63-75]. Electrochemical anodic deposition consists in applying a positive current or potential to obtain a direct oxidation of  $Ce^{3+}$  to  $Ce^{4+}$  species at the electrode. This approach is widely used to obtain metal oxides but less studied for ceria preparation although it provides some interesting perspectives. In fact, ceria anodic deposition is a direct electrochemical oxidation that lead to purer deposits in terms of inclusion of precursors and in terms of homogeneity and adherence to substrates. Cathodic deposition follows the well-studied base generation electrodeposition path, a process that was first introduced by Switzer and co-workers in 1994 to prepare nanocrystalline  $CeO_2$  powders and at a later time to prepare films with the purpose of increasing resistance of metals and alloys to high temperature corrosion [41,64]. Most of literature on ceria electrodeposition was focused on the cathodic preparation of protective film for corrosion application, but SEM analyses clearly show how film morphologies present big cracks that are caused by the large mismatch between the substrates and the film during growth and by the drying process. This phenomenon is common on almost all wet chemical methods used to deposit  $CeO_2$  films. In the end, film cracking confirmed to be a major drawback of electrodeposition for corrosion applications and lately electrochemical preparation of ceria returned as a tool to prepare materials for polymer electrolyte membrane fuel cells [76], for sensing [77], for water treatment [78] and to prepare condensate microdrop self-propelling surfaces [79].

#### I.4. Bibliography

1. Johan Rockström, Will Steffen, Kevin Noone, Åsa Persson, F. Stuart Chapin, III, Eric F. Lambin, Timothy M. Lenton, Marten Scheffer, Carl Folke, Hans Joachim Schellnhuber, Björn Nykvist, Cynthia A. de Wit, Terry Hughes, Sander van der Leeuw, Henning Rodhe, Sverker Sörlin, Peter K. Snyder, Robert Costanza, Uno Svedin, Malin Falkenmark, Louise Karlberg, Robert W. Corell, Victoria J. Fabry, James Hansen, Brian Walker, Diana Liverman, Katherine Richardson, Paul Crutzen, Jonathan A. Foley, A safe operating space for humanity, *Nature* 461 (2009) 472-475.
2. Hansen, J., R. Ruedy, M. Sato, and K. Lo, Global surface temperature change. *Rev. Geophys.* 48 (2010) RG4004.
3. *EPICA Dome C and Vostok Station, Antarctica: approximately 796,562 BCE to 1813 CE*  
Lüthi, D., M. Le Floch, B. Bereiter, T. Blunier, J.-M. Barnola, U. Siegenthaler, D. Raynaud, J. Jouzel, H. Fischer, K. Kawamura, and T.F. Stocker. 2008. High-resolution carbon dioxide concentration record 650,000–800,000 years before present. *Nature* 453:379–382.  
[www.ncdc.noaa.gov/paleo/pubs/luethi2008/luethi2008.html](http://www.ncdc.noaa.gov/paleo/pubs/luethi2008/luethi2008.html).
4. *Law Dome, Antarctica, 75-year smoothed: approximately 1010 CE to 1975 CE*  
Etheridge, D.M., L.P. Steele, R.L. Langenfelds, R.J. Francey, J.-M. Barnola, and V.I. Morgan. 1998. Historical CO<sub>2</sub> records from the Law Dome DE08, DE08-2, and DSS ice cores. In: *Trends: A compendium of data on global change*. Oak Ridge, TN: U.S. Department of Energy. Accessed September 14, 2005.  
<http://cdiac.ornl.gov/trends/co2/lawdome.html>.
5. *Siple Station, Antarctica: approximately 1744 CE to 1953 CE*  
Neftel, A., H. Friedli, E. Moor, H. Lötscher, H. Oeschger, U. Siegenthaler, and B. Stauffer. 1994. Historical carbon dioxide record from the Siple Station ice core. In: *Trends: A compendium of data on global change*. Oak Ridge, TN: U.S. Department of Energy. Accessed September 14, 2005.  
<http://cdiac.ornl.gov/trends/co2/siple.html>.
6. *Mauna Loa, Hawaii: 1959 CE to 2015 CE*  
NOAA (National Oceanic and Atmospheric Administration). 2016. Annual mean carbon dioxide concentrations for Mauna Loa, Hawaii. Accessed April 14, 2016.  
[ftp://ftp.cmdl.noaa.gov/products/trends/co2/co2\\_annmean\\_mlo.txt](ftp://ftp.cmdl.noaa.gov/products/trends/co2/co2_annmean_mlo.txt).
7. *Barrow, Alaska: 1974 CE to 2014 CE*  
*Cape Matatula, American Samoa: 1976 CE to 2014 CE*  
*South Pole, Antarctica: 1976 CE to 2014 CE*  
NOAA (National Oceanic and Atmospheric Administration). 2016. Monthly mean carbon dioxide concentrations for Barrow, Alaska; Cape Matatula, American Samoa; and the South Pole. Accessed April 14, 2016. [ftp://ftp.cmdl.noaa.gov/data/trace\\_gases/co2/in-situ/surface](ftp://ftp.cmdl.noaa.gov/data/trace_gases/co2/in-situ/surface).
8. *Cape Grim, Australia: 1992 CE to 2006 CE*  
*Shetland Islands, Scotland: 1993 CE to 2002 CE*  
Steele, L.P., P.B. Krummel, and R.L. Langenfelds. 2007. Atmospheric CO<sub>2</sub> concentrations (ppmv) derived from flask air samples collected at Cape Grim, Australia, and Shetland Islands, Scotland. Commonwealth Scientific and Industrial Research Organisation. Accessed January 20, 2009.  
<http://cdiac.esd.ornl.gov/ftp/trends/co2/csiro>.
9. *Lampedusa Island, Italy: 1993 CE to 2000 CE*  
Chamard, P., L. Ciattaglia, A. di Sarra, and F. Monteleone. 2001. Atmospheric carbon dioxide record from flask measurements at Lampedusa Island. In: *Trends: A compendium of data on global change*. Oak Ridge, TN: U.S. Department of Energy. Accessed September 14, 2005.  
<http://cdiac.ornl.gov/trends/co2/lampis.html>.
10. Intergovernmental Panel on Climate Change, *Climate Change 2014, Synthesis Report*.
11. Karl, T. R.; Trenberth, K. E. *Modern Global Climate Change Science* 302 (2003) 1719.
12. IPCC. (2016a). Decision IPCC-XLIV/L-2. Retrieved from [https://www.ipcc.ch/meetings/session44/l2\\_adopted\\_outline\\_sr15.pdf](https://www.ipcc.ch/meetings/session44/l2_adopted_outline_sr15.pdf)

13. IPCC. (2016b). Decision IPCC-XLIV/Doc. 121.5. Retrieved from <https://www.ipcc.ch/apps/eventmanager/documents/40/210920161051-Doc.12-OutlineMethreport.pdf>
14. Hironori Arakawa, Michele Aresta, John N. Armor, Mark A. Barteau, Eric J. Beckman, Alexis T. Bell, John E. Bercaw, Carol Creutz, Eckhard Dinjus, David A. Dixon, Kazunari Domen, Daniel L. DuBois, Juergen Eckert, Etsuko Fujita, Dorothy H. Gibson, William A. Goddard, D. Wayne Goodman, Jay Keller, Gregory J. Kubas, Harold H. Kung, James E. Lyons, Leo E. Manzer, Tobin J. Marks, Keiji Morokuma, Kenneth M. Nicholas, Roy Periana, Lawrence Que, Jens Rostrup-Nielson, Wolfgang M. H. Sachtler, Lanny D. Schmidt, Ayusman Sen, Gabor A. Somorjai, Peter C. Stair, B. Ray Stults and William Tumas, Catalysis Research of Relevance to Carbon Management: Progress, Challenges, and Opportunities Chem. Rev. 101 (2001) 953–996.
15. Navarro, R.M., Peña, M.A., Fierro, J.L.G., Hydrogen production reactions from carbon feedstocks: Fossil fuels and biomass Chem. Rev. 107 (2007) 3952-3991.
16. Mette Mikkelsen, Mikkel Jørgensen and Frederik C. Krebs, The teraton challenge. A review of fixation and transformation of carbon dioxide Energy Environ. Sci. 3 (2010) 43–81.
17. C.E. McGlade, A review of the uncertainties in estimates of global oil resources Energy 47 (2012) 262-270.
18. Gabriele Centi, Siglinda Perathoner, Opportunities and prospects in the chemical recycling of carbon dioxide to fuels, Catalysis Today 148 (2009) 191–205.
19. Evgenii V. Kondratenko, Guido Mul, Jonas Baltrusaitis, Gastón O. Larrazábal, Javier Pérez-Ramírez Status and perspectives of CO<sub>2</sub> conversion into fuels and chemicals by catalytic, photocatalytic and electrocatalytic processes, Energy Environ. Sci. 6 (2013) 3112-3135.
20. Frank Marken, David Fermin, Electrochemical Reduction of Carbon Dioxide: Overcoming the Limitations of Photosynthesis, (The Royal Society of Chemistry 2018 ISBN: 978-1-78262-042-6)
21. T. Sakakura, J. Choi and H. Yasuda, Transformation of Carbon Dioxide, Chem. Rev. 107 (2007) 2365.
22. Hori Y. In: Vayenas C.G., White R.E., Gamboa-Aldeco M.E. Modern Aspects of Electrochemistry n°42 (Springer, New York 2008).
23. Richard C. Alkire, Dieter M. Kolb, Jacek Lipkowski, Electrocatalysis: Theoretical Foundations and Model Experiments, (John Wiley & Sons, 2013 ISBN: 978-3-527-33227-4).
24. C. M. Sánchez-Sánchez, V. Montiel, D. A. Tryk, A. Aldaz, A. Fujishima, Electrochemical approaches to alleviation of the problem of carbon dioxide accumulation, Pure Appl. Chem. 73 (2001) 1917–1927.
25. Qi Lu, Feng Jiao, Electrochemical CO<sub>2</sub> reduction: electrocatalyst, reaction mechanism, and process engineering, Nano Energy 29 (2016) 439–456.
26. Jinli Qiao, Yuyu Liu, Feng Hong, JiuJun Zhang, A review of catalysts for the electroreduction of carbon dioxide to produce low-carbon fuels, Chem. Soc. Rev. 43 (2014) 631.
27. Jong Suk Yoo, Rune Christensen, Tejs Vegge, Jens K. Nørskov, Felix Studt, Theoretical Insight into the Trends that Guide the Electrochemical Reduction of Carbon Dioxide to Formic Acid, ChemSusChem 9 (2016) 358 –363.
28. Xinyan Liu, Jianping Xiao, Hongjie Peng, Xin Hong, Karen Chan, Jens K. Nørskov, Understanding trends in electrochemical carbon dioxide reduction rates, Nature Communications 8 (2017) 15438.
29. Schwarzenbach G., Meier J., Formation and investigation of unstable protonation and deprotonation products of complexes in aqueous solution, J. Inorg. Nuclear Chem. 8 (1958) 302–312.
30. Y. Hori, H. Konishi, T. Futamura, A. Murata, O. Koga, H. Sakurai, K. Oguma, Deactivation of copper electrode” in electrochemical reduction of CO<sub>2</sub> Electrochim. Acta 50 (2005) 5354.
31. Y. Hori, H. Wakebe T. Tsukamoto and O. Koga, Electrocatalytic process of CO selectivity in electrochemical reduction of CO<sub>2</sub> at metal electrodes in aqueous media, Electrochim. Act. 39 (1994) 1833.
32. Kašpar, J., Fornasiero, P., Hickey, N., Automotive Catalytic Converters: Current Status and Some Perspectives. Catal. Today 77 (2003) 419–449.

33. M. Haruta, A. Ueda, S. Tsubota, R.M. Torres Sanchez, Low-temperature catalytic combustion of methanol and its decomposed derivatives over supported gold catalysts, *Catalysis Today* 29 (1996) 443–447.
34. N.S. Kaisare, D.G. Vlachos, A review on microcombustion: fundamentals, devices and applications, *Prog. Energy Combust. Sci.* 38 (2012) 321–359.
35. X. Wang, C. Zhang, Z. Zeng, Z. Hu, Preparation of supported noble metal catalysts for methanol catalytic combustion at room temperature, *Combust. Sci. Technol.* 184 (2012) 842–849
36. S. Cimino, R. Nigro, U. Weidmann, R. Holzner, Catalytic Combustion of Methanol over La, Mn-Hexaaluminate Catalysts, *Fuel Process. Technol.* 133 (2015) 1-7.
37. S. Imamura, T. Higashihara, Y. Saito, H. Aritani, H. Kanai, Y. Matsumura, N. Tsuda, Decomposition of methanol on Pt-loaded ceria, *Catal. Today* 50 (1999) 369±380
38. G. Avgouropoulos, J. Papavasiliou, T. Ioannides, Hydrogen production from methanol over combustion-synthesized noble metal/ceria catalysts, *Chem. Eng. J.* 154 (2009) 274–280.
39. G. Avgouropoulos, Isotopic transient study of methanol decomposition over noble metal/ceria catalysts, *Catal. Comm.* 10 (2009) 682–686.
40. V. Meille, Review on methods to deposit catalysts on structured surfaces. *Appl. Catal. A Gen.* 315 (2006) 1–17.
41. Switzer J., Electrochemical Synthesis and Sintering of Nanocrystalline Cerium(IV) Oxide Powders, *J. Am. Ceram. Soc.* 78 (1994) 981.
42. Basile F., Benito P., Fornasari G., Rosetti V., Scavetta E., Tonelli D., Vaccari A., Electrochemical synthesis of novel structured catalysts for H<sub>2</sub> production, *Appl Catal B Environ* 91 (2009) 563–572.
43. Basile F., Benito P., Fornasari G., Monti M., Scavetta E., Tonelli D., Vaccari A. Novel Rh-based structured catalysts for the catalytic partial oxidation of methane, *Catal Today* 157 (2010) 183-190.
44. P. Benito, G. Nuyts, M. Monti, W. De Nolf, G. Fornasari, K. Janssens, E. Scavetta and A. Vaccari, Stable Rh particles in hydrotalcite-derived catalysts coated on FeCrAlloy foams by electrosynthesis, *Appl. Catal. B Environ.* 179 (2015) 321–332.
45. Herman, R.G., Klier, K., Simmons, G.W., Finn, B.P., Bulko, J.B.a, Kobylinski, T.P, Catalytic synthesis of methanol from CO H<sub>2</sub>. I. Phase composition, electronic properties, and activities of the Cu/ZnO/M<sub>2</sub>O<sub>3</sub> catalysts, *Journal of Catalysis* 56 (1979) 407-429.
46. W.B. Li, J.X. Wang, H. Gong, Catalytic combustion of VOCs on non-noble metal catalysts, *Catalysis Today* 148 (2009) 81–87.
47. Du P., Eisenberg R., Catalysts made of earth-abundant elements (Co, Ni, Fe) for water splitting: Recent progress and future challenges, *Energy Environ. Sci.* 5 (2012) 6012.
48. Liang, Y., Li, Y., Wang, H., Zhou, J., Wang, J., Regier, T., Dai, H., Co<sub>3</sub>O<sub>4</sub> nanocrystals on graphene as a synergistic catalyst for oxygen reduction reaction, *Nature Materials* 10 (2011) 780–786.
49. Haxel, G. B., Hedrick, J. B., Orris, G. J. Supporting Sound Management of Our Mineral Resources: Rare Earth Elements Critical Resources for High Technology; United States Geological Survey Fact Sheet; 087–02; USGS: Reston, VA, (2002) 4.
50. R. Kijrner, M. Ricken, J. Nijlting, I. Riess, Phase transformations in reduced ceria: determination by thermal expansion measurements, *Journal of Solid State Chemistry* 78 (1989) 136-147.
51. Bernal, S., Calvino, J.J., Cifredo, G.A., Gatica, J.M., Pérez Omil, J.A., Pintado, J.M, Hydrogen chemisorption on ceria: Influence of the oxide surface area and degree of reduction, *Journal of the Chemical Society, Faraday Transactions* 89 (1993) 3499-3505.
52. A. Trovarelli, Catalytic properties of ceria and CeO<sub>2</sub>-containing materials, *Catal. Rev.* 38 38 (1996) 439–520.
53. Tiziano Montini, Michele Melchionna, Matteo Monai, Paolo Fornasiero, Fundamentals and Catalytic Applications of CeO<sub>2</sub>-Based Materials, *Chem. Rev.* 116 (2016) 5987–6041.
54. C. Xu, P.K. Shen, Electrochemical oxidation of ethanol on Pt-CeO<sub>2</sub>/C catalysts, *J. Power Sources* 142 (2005) 27–29.

55. C.L. Campos, C.Roldan, M. Aponte, Y. Ishikawa, C.R. Cabrera, Preparation and methanol oxidation catalysis of Pt-CeO<sub>2</sub> electrode, *J. Electroanal. Chem.* 581 (2005) 206–215.
56. D.J. Diaz, N. Greenleitch, A. Solanki, A. Karakoti, S. Seal, Novel nanoscale ceria-platinum composite electrodes for direct alcohol electro-oxidation, *Catal. Lett.* 119 (2007) 319-326.
57. J. Wang, X. Deng, J. Xi, L. Chena, W. Zhua, X. Qiu, Promoting the current for methanol electro-oxidation by mixing Pt-based catalysts with CeO<sub>2</sub> nanoparticles, *J. of Power Sources* 170 (2007) 297–302.
58. M.A. Scibioh, S.-K. Kim, E.A. Cho, T.-H. Lim, S.-A. Hong, H.Y. Ha, Pt-CeO<sub>2</sub>/C anode catalyst for direct methanol fuel cells, *Appl. Catal. B: Environ.* 84 (2008) 773–782.
59. Y. Zhou, Y. Gao, Y. Liu, J. Liu, High efficiency Pt-CeO<sub>2</sub>/carbon nanotubes hybrid composite as an anode electrocatalyst for direct methanol fuel cells, *J. Power Sources* 195 (2010) 1605–1609.
60. Chunwen Sun, Hong Liab, Liquan Chen, Nanostructured ceria-based materials: synthesis, properties, and applications, *Energy Environ. Sci.* 5 (2012) 8475.
61. A.Q. Wang, T.D. Golden, Anodic Electrodeposition of Cerium Oxide Thin Films I. Formation of Crystalline Thin Films, *J. Electrochem. Soc.* (2003) 150 C616-C620.
62. T.D. Golden, A.Q. Wang, Anodic Electrodeposition of Cerium Oxide Thin Films II. Mechanism studies, *J. Electrochem. Soc.* (2003) 150 C621-C624.
63. A. J. Aldykiewicz, Jr., A. J. Davenport, H. S. Isaacs, Studies of the Formation of Cerium-Rich Protective Films Using X-Ray Absorption Near-Edge Spectroscopy and Rotating Disk Electrode Methods, *J. Electrochem. Soc.* 143 (1996) 147-154.
64. Y. Zhou, Jay A. Switzer, Growth of Cerium(IV) oxide films by the electrochemical generation of base method, *Journal of Alloys and Compounds* 237 (1996) 1-5.
65. F.-B. Li, R. C. Newman, G. E. Thompson, In situ atomic force microscopy studies of electrodeposition mechanism of cerium oxide films: nucleation and growth out of a gel mass precursor, *Electrochim. Acta*, 42 (1997) 2455-2464.
66. J. Creus, F. Brezault, C. Rebere, M. Gadouleau, Synthesis and characterisation of thin cerium oxide coatings elaborated by cathodic electrolytic deposition on steel substrate, *Surface & Coatings Technology* 200 (2006) 4636 – 4645.
67. Y. Hamlaoui, F. Pedraza, L. Tifouti, Investigation of electrodeposited cerium oxide based films on carbon steel and of the induced formation of carbonated green rusts, *Corrosion Science* 50 (2008) 2182–2188.
68. V. Fernandes, J. J. Klein, W. H. Schreiner, N. Mattoso, D. H. Mosca, Electrodeposition of Nanocrystalline CeO<sub>2</sub> on Si(001), *J. Electrochem. Soc.* 156 (2009) E199-E204.
69. Y. Hamlaoui, F. Pedraza, C. Remazeilles, S. Cohendoz, C. Rébéré, L. Tifouti, J. Creus, Cathodic electrodeposition of cerium-based oxides on carbon steel from concentrated cerium nitrate solutions Part I. Electrochemical and analytical characterisation, *Materials Chemistry and Physics* 113 (2009) 650–657.
70. Y. Hamlaoui, L. Tifouti, C. Remazeilles, F. Pedraza, Cathodic electrodeposition of cerium based oxides on carbon steel from concentrated cerium nitrate. Part II: Influence of electrodeposition parameters and of the addition of PEG, *Materials Chemistry and Physics* 120 (2010) 172–180.
71. B. Bouchaud, J. Balmain, G. Bonnet, F. Pedraza, Optimizing structural and compositional properties of electrodeposited ceria coatings for enhanced oxidation resistance of a nickel-based superalloy, *Applied Surface Science* 268 (2013) 218– 224.
72. B. Bouchaud, J. Balmain, G. Bonnet, F. Pedraza, Correlations between electrochemical mechanisms and growth of ceria based coatings onto nickel substrates, *Electrochimica Acta* 88 (2013) 798–806.
73. D. Stoychev, Corrosion protective ability of electrodeposited ceria layers, *J. Solid State Electrochem.* 17 (2013) 497–509.
74. F. Faisal, A. Toghan, I. Khalakhan, M. Vorokhta, V. Matolin, Jörg Libuda, Characterization of thin CeO<sub>2</sub> films electrochemically deposited on HOPG, *Applied Surface Science* 350 (2015) 142–148.
75. P. Bocchetta, M. Santamaria, F. Di Quarto, Cerium Oxyhydroxide Nanowire Growth via Electrogenation of Base in Nonaqueous Electrolytes, *Electrochem. Solid-State Lett.* 11 (2008) K93-K97.
76. D.-J. Guo, Z.-H. Jing, A novel co-precipitation method for preparation of Pt-CeO<sub>2</sub> composites on multi-walled carbon nanotubes for direct methanol fuel cells, *J. Power Sources* 195 (2010) 3802–3805.

77. Cristina Ispas, John Njagi, Meghan Cates, Silvana Andreescu, Electrochemical Studies of Ceria as Electrode Material for Sensing and Biosensing Applications, *J. Electrochem. Soc.*, 155 (2008) F169-F176.
78. Xi-hong Lu, De-zhou Zheng, Jia-yong Gan, Zhao-qing Liu, Chao-lun Liang, Peng Liu, Ye-xiang Tong, J. Porous CeO<sub>2</sub> nanowires/nanowire arrays electrochemical synthesis and application in water treatment, *Mater. Chem.* 20 (2010) 7118-7122.
79. Yuting Luo, Juan Li, Jie Zhu, Ye Zhao, Xuefeng Gao, Fabrication of Condensate Microdrop Self-Propelling Porous Films of Cerium Oxide Nanoparticles on Copper Surfaces, *Angew. Chem. Int. Ed.* 54 (2015) 4876-4879.

# CHAPTER 1: CO<sub>2</sub>RR on ceria

## 1.1 Introduction & motivation

Formic acid has been proposed as a valuable energy feedstock that can be used directly on a fuel cell or as a H<sub>2</sub> source through catalytic decomposition [1]. To produce formic acid (or formate) selectively reducing CO<sub>2</sub> could be really appealing considering its high volumetric (53.4 gL<sup>-1</sup>) and moderate gravimetric (4.4 wt.%) hydrogen storage capacity in ambient conditions. In Fig.1, the Pourbaix diagram for CO<sub>2</sub>/HCOOH system, calculated on the basis of thermodynamic data, shows that operating at neutral pH region, formate can be generated directly by reducing CO<sub>2</sub>, limiting HER (prevailing in acidic media) and carbonate formation generated from equilibrium with CO<sub>2</sub> in alkaline [2]. Most of papers studying CO<sub>2</sub>RR in water used phosphate or carbonate buffered solutions with pH close to 7 [2,3,4].

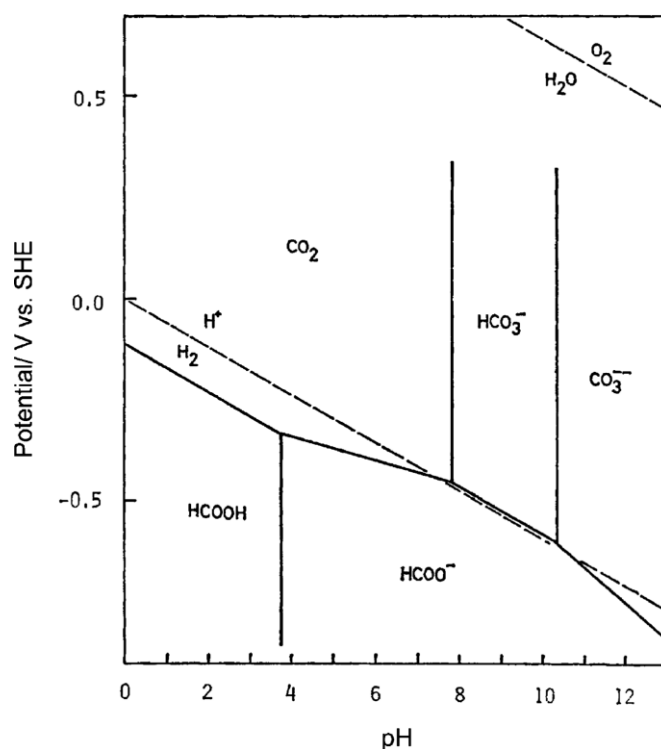


**Fig.1.** Pourbaix diagram for CO<sub>2</sub>/HCOOH system, calculated on the basis of thermodynamic data. pH potential relations for water are shown in broken lines.

As mentioned in 1.2, several electrodes can generate formate through CO<sub>2</sub>RR; Pb, Hg, Tl, In, Sn, Cd, Bi all can give formate with efficiency higher than 70% in carbonate at potential lower than -1V vs SHE [2,5-8] (Cu unique properties toward CO<sub>2</sub>RR will be addressed on chapter 3) but obtaining higher efficiencies with low overpotential it's very difficult. Kanan and co-workers reported some results on CO<sub>2</sub> reduction over SnO<sub>x</sub>

electrodes to give formate at -0.7V reaching over 40% of efficiency toward formate [6]; they also reported a very promising study on Pb-based electrodes obtained reducing thick PbO<sub>2</sub> layers gives almost 100% conversion with potential from -0.7V to -1V [9]. Very recently Li and co-workers published some results regarding Bi nanostructures prepared from BiO nanosheet reduced in-situ to give a high efficient electrode that produce HCOOH with almost 100% efficiency at overpotentials of 0.7V [5]. Furthermore, electrodes show a good efficiency (around 40%) at overpotential of 0.3-0.4V and are stable for several hours of electrolysis. Like some review already evidenced, application limits of almost all these materials seems to be the high overvoltage required to have high selectivity toward formate and the fact that some of them, for example Pb, are toxic or not green-friendly. In addition to non-noble transition metals, Pd is recognized as a catalyst that can produce formate at potential close to standard reduction potential, but early works reported low faradaic efficiencies. More recently, application of nanostructures and alloys increased sensibly efficiency to reach high efficiencies. For example Kanan and co-workers reported values of over 90% at potential as low as -0.1V vs SHE for Pd nanoparticles on carbon support [10] but with strong poisoning of surface due to adsorbed CO once overpotential is increased. Kortlever and co-workers reported an accurate study of Pt-Pd alloys in function of the size of nanoparticles that shown high conversion to formate at low overpotential and with good stability [11]. What is generally reducing the appealing of Pd-based catalyst, other than high cost compared to non-noble metals, is the fast decay of polarization currents, generally due to surface poisoning or structure reconstruction. Very recently Melchionna and co-workers showed how Pd@TiO<sub>2</sub> nanoparticles supported on single wall carbon nanotubes were able to reduce CO<sub>2</sub> to formic acid at near zero overpotential and simultaneously to evolve H<sub>2</sub> via dehydrogenation of formic acid obtained electrochemically [12]. Authors claim a so-called "circular catalysis" of CO<sub>2</sub> and catalyst stability was measured in 24h test that showed almost no current decreasing. Pd activity toward electrochemical CO<sub>2</sub>RR is due probably to the formation of surface Pd-H that can selectively hydrogenate CO<sub>2</sub> to formic acid at low overpotentials; this is also confirmed by Tafel plot that give 2 different slopes at low and high overpotentials. Recently Gao and co-workers confirmed this mechanism correlating the polarization potential and the consequent H coverage of Pd surface with CO<sub>2</sub> reduction products intermediates [13]. Boni and co-workers worked on a similar system consisting of Pd/CeO<sub>2</sub> supported on Carbon Nanotubes (CNTs). They reported a higher formic acid production in carbonate and in nitric acid for MWCNT@CeO<sub>2</sub> electrodes compared to MWCNT@Pd/CeO<sub>2</sub>. These results seem to be in contrast with some papers published recently but the authors explained their lack of activity of Pd containing electrodes by poor Pd dispersion and very low Pd loading in their system compared to literature catalysts [14]. What is more interesting is that they measured very high efficiency for MWCNT@CeO<sub>2</sub> with no palladium. This was something never observed before and they speculated about a mechanism involving formation of ceria hydride species that can hydrogenate CO<sub>2</sub> to formic acid, similar to the one observed for palladium. The work for this part of the thesis was partially inspired by these results and partially inspired by

curiosity to explore analogies between ceria unique properties in gas phase heterogeneous catalysis and electrocatalysis. In particular, we want to explore properties of ceria films prepared with an electrochemical approach, toward CO<sub>2</sub> electrochemical reduction in neutral media. We especially focused on formate production at very low overpotentials and on the relation, if any, with ceria oxygen stoichiometry.

## 1.2 Electrode preparation

### 1.2.1 Support choice: boron doped diamond

The aim of this work was to study electrochemical deposition of ceria and its application to electrocatalytic reduction of CO<sub>2</sub> in water, the first step was to choose the right support that can be functionalized with ceria.

Support should have the following characteristics:

- Should not be active toward CO<sub>2</sub>RR, especially in the potential window explored
- Should not be catalytic toward HER, otherwise it will be difficult to calculate reactions efficiencies
- Should be conductive, to prevent the slowing down of reaction by electron transport limitations.

One of the few, if not the only class of material, that respected the previous conditions are doped diamond electrodes. In particular, thanks to a collaboration with Prof. Einaga, we had a chance to work with some Boron Doped Diamond (BDD) prepared in Einaga's Group at Keio University [15]. BDD became a major argument of research since its development in the seventies. The stimulus behind such push could be attributed to their wide potential window, low background current, chemical inertness, and mechanical durability [16,17]; these features suit perfectly to electrochemical applications, especially for electroanalytical chemistry and electrochemical water treatment.

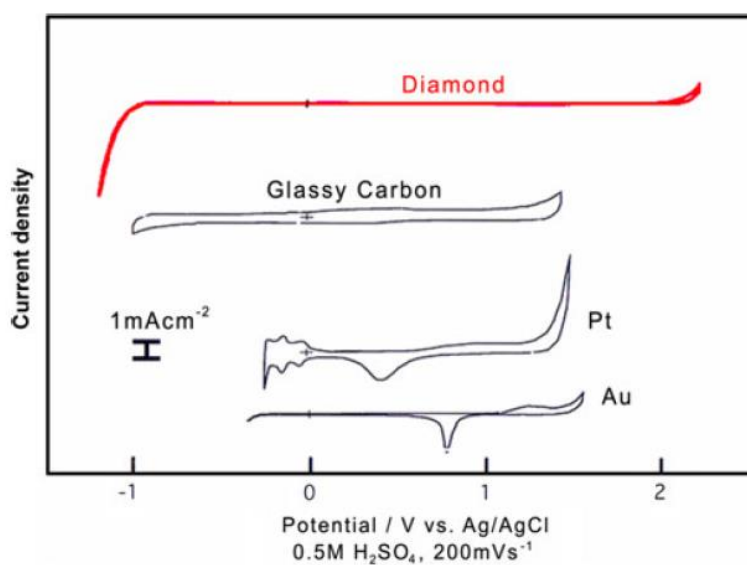
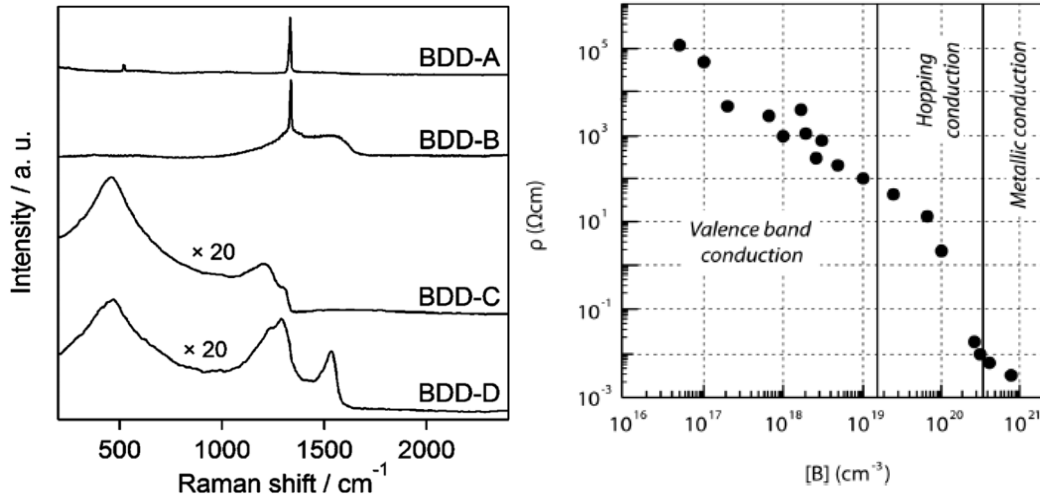


Fig.1. Electrochemical properties of various electrodes [17].

Diamond with its  $sp^3$  hybridization is known to be non-electroactive. When boron is added as doping agent, a disorder is generated with the consequent variation of diamond structure; Raman Spectroscopy confirms this effect [15] (Fig.2). There are several types of BDD obtained with different preparation modes, amount of doping and size of crystallites.



**Fig.2.** (Left) Raman spectra of BDD films with a B/C ratio of 0.1% with the absence (BDD-A) and presence (BDD-B) of  $sp^2$ , BDD with B/C ratios of 1% (BDD-C) and 5% (BDD-D) [15]. (Right) Room-temperature resistivity as a function of boron doping [18].

Our BDD films were deposited on Si wafer through a microwave plasma-assisted chemical vapour deposition (CVD), had a crystals range from 1 to 8  $\mu\text{m}$  with a 5  $\mu\text{m}$  average and were doped with 1% of Boron. Increasing boron content increases conductivity but also gives higher background current and a narrower potential window, 1% of Boron correspond to a concentration of ca  $1.7 \times 10^{21}$  boron atoms per  $\text{cm}^3$ , and is sufficient to impart BDD metal-like conduction [18]. Grain size of BDD crystals are not influenced by the B/C ratio, instead CVD conditions, such as pressure, temperature, and deposition time, strongly affect the grain size of the BDD film.

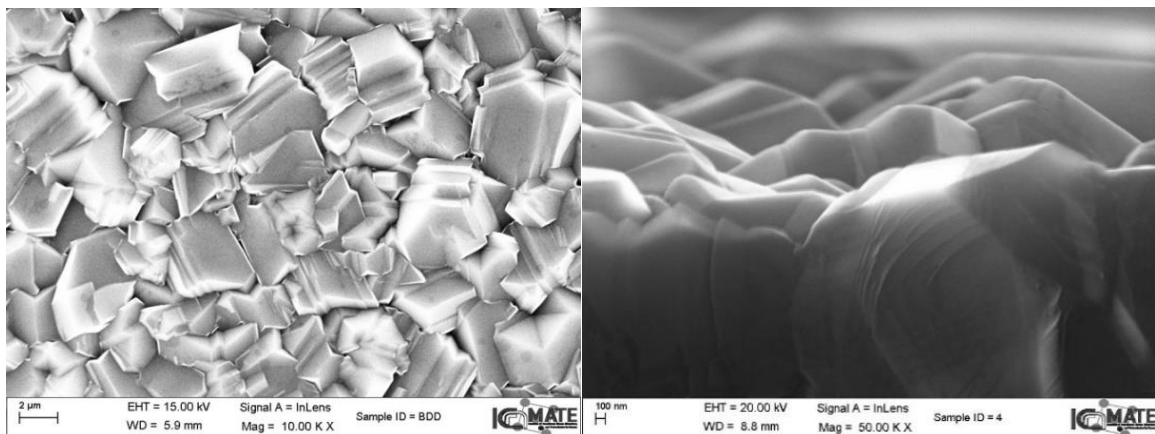


**Fig.3.** SEM images of a bare BDD electrode (left) and of a cross section of a bare BDD (right).

Carbon  $sp^2$  impurities in the BDD film are often considered the active sites for electrochemical reactions, albeit they are responsible of decreasing the stability of electrode surface and reducing free potential window [19]. They tend to be formed in the grain boundaries and defects during the CVD. These impurities make electrodes more electroactive, that in case of electrocatalysis applications, could be beneficial, even though surface can potentially become more susceptible to fouling. In our case, since we want to measure the activity of a phase deposited on BDD toward a reaction that it is known to be surface sensitive, impurities amount must be reduced as much as possible. Cleaning was performed by scanning at 0.3 V/s in  $HClO_4$  0.1M for 20 cycles. Figure 4 report cyclic voltammtries performed to clean the electrode; the insert highlights a region that shows an oxidation peak generated by oxidation of  $sp^2$  carbon defects. Relative intensity of this peak provide indications on the grade of BDD quality in terms of carbon purity.

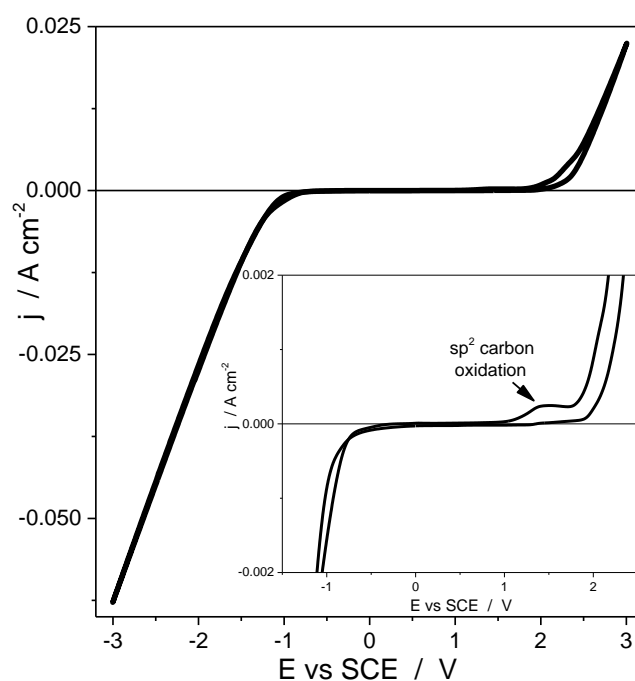


**Fig.4.** Cyclic voltammetry performed on a BDD electrode in  $HClO_4$  0.1M, scan rate 0.300 V/s, 20 cycles. Zoom of the potential window with carbon  $sp^2$  oxidation peak.

Surface termination of BDD is an important parameter to evaluate for “in solution” electrochemical measurements, because it can influence electron transfer kinetics, wettability of the electrode. Usually BDD prepared with a  $H_2$  plasma CVD process leaves the deposition chamber with H-termination. By treating with hydrogen or oxygen plasma BDD after the growth its surface will be terminated respectively with H or O. H-termination usually is stable for long time but, if necessary, can be restored by cathodically cycling the electrode in acidic media. Surface termination can be measured by contact angle measurements, a high value

of contact angle means that surface is hydrophobic and the surface is H-terminated, to the contrary a value less than  $65^\circ$  correspond to a O-termination [16]. Before any experiment, after cleaning, we performed a surface activation by cycling the electrode between 0 and -3V vs SCE in  $\text{HClO}_4$  to restore H-termination. For our electrochemical measurements, that include cathodic scans and polarizations, having a H-termination was mandatory to maintain a good reproducibility; O-termination would have guaranteed a better wettability but increasing boron doping over a certain value, the  $\text{sp}^2$  increases generating defects at the film grain boundaries and in the diamond lattice this usually increases wettability. Fig.5 below shows H-termination restoring evidenced by hydrogen evolution current increasing toward cycling.

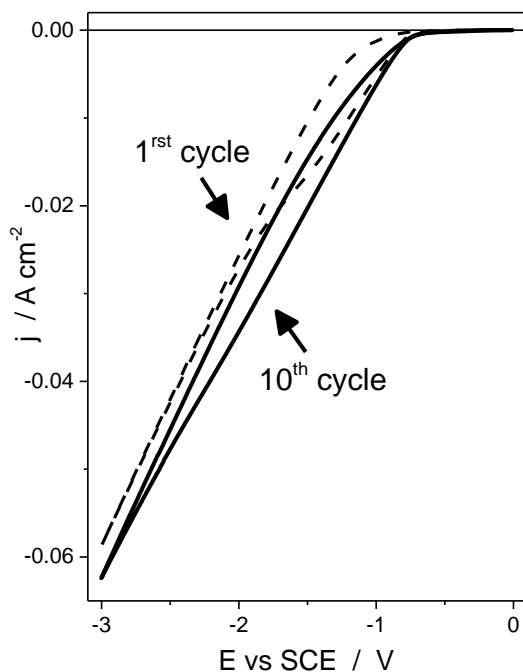


**Fig.5.** Cyclic voltammetry performed on a BDD electrode in  $\text{HClO}_4$  0.1M, scan rate 0.300 V/s, 1<sup>st</sup> and 10<sup>th</sup> cycles reported.

### 1.2.2 Ceria deposition on BDD electrodes

As we stated in 1.3, ceria has been electrodeposited cathodically or anodically. Mechanism of cathodic deposition method remains in some aspect unclear; we can divide the process in two steps: the surface alkalinisation and the  $Ce^{3+}$  to  $Ce^{4+}$  oxidation. A scheme of electrodeposition process is reported below.

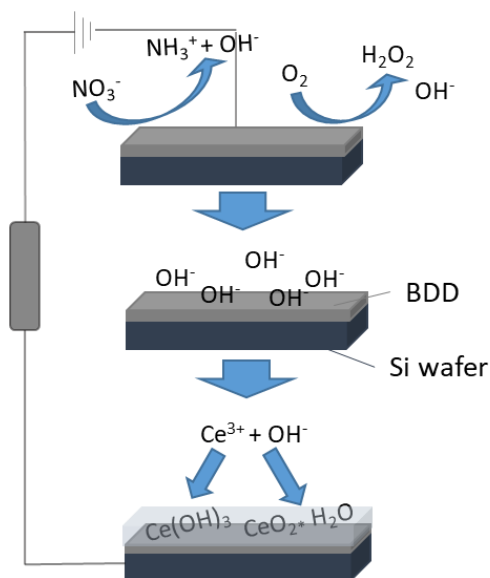
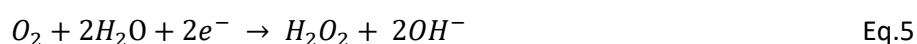


**Fig.6.** Scheme representing the electroprecipitation process on BDD electrodes

Alkalinisation strongly depend on electrolyte composition and pH; we used nitrate-based solution but in literature other solutions can be found, including chloride or acetate based baths with or without  $H_2O_2$  as additive [20-33]. Starting from a nitrate deposition bath several reduction reactions can produce  $OH^-$  at the electrode:



It is clear that the concentration of species and applied potentials decide the amount of  $OH^-$  produced at the electrode enhancing the pH of the whole solution, starting with basification of a thin layers close to the electrode. Starting pH of the bulk solution is approximatively 4.5 and some papers report pH 10-12 close to the electrode surface under cathodic polarization [22,34]. Fig.7 is a sketch of the concentration profiles of species involved in the electrodeposition mechanism, as a function of distance from the electrode. Something that must be evidenced is the fact that the cell used has no separation between working and counter

electrode, so oxygen produced at Pt anode can diffuse in the solution enhancing the concentration of oxygen dissolved.

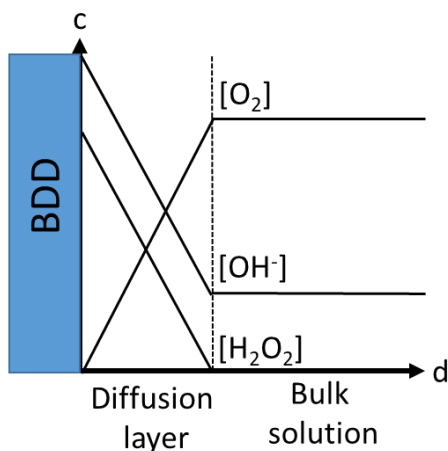


**Fig.7.** Concentration profile of species involved in the electroprecipitation in function of distance from electrode surface.

A linear sweep voltammetry registered on a BDD electrode in a 0.1M NaNO<sub>3</sub> deposition bath is reported in Fig.8. Based on literature, one can recognize several different processes: at around -1V the reduction of nitrate to nitrite described by Eq.2 (a), at around 1.3V the reduction of nitrite to ammonium (b), below -1.5V the predominant hydrogen evolution reaction (c) In the potential window between 0 and -1V, highlighted in the magnified insert of Fig.8, there are two diffusion limited plateaux, the first around -0.4 correspond to hydrogen peroxide formation (d) and the second, less pronounced is attributed to further reduction of H<sub>2</sub>O<sub>2</sub> (e) [34]. All these reactions participate in solution alkalisation and in principle we can affirm that the more negative is the potential applied the higher is the basification of the solution next to the electrode surface.

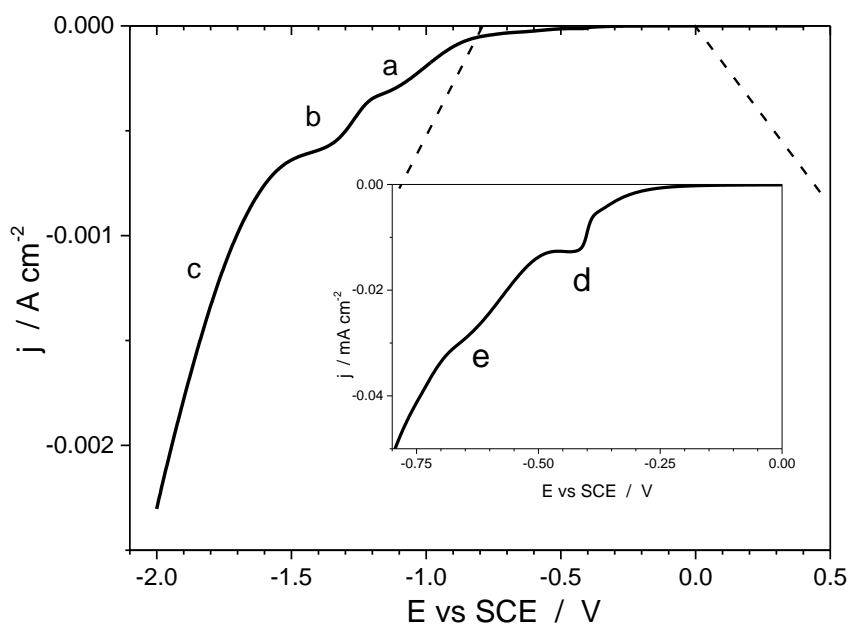
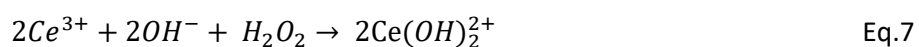
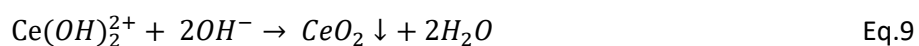
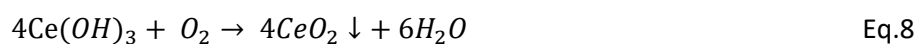


**Fig.8.** Linear sweep voltammetry registered in 0.1M NaNO<sub>3</sub>, 0.4mM Ce(NO<sub>3</sub>)<sub>3</sub>, scan rate 1 mV/s. Insert correspond to a magnification of a narrower potential window.

The mechanism of deposition of ceria over several supports was studied extensively in literature; many authors suggested that the mechanism of reaction is related to the oxygen reduction on the electrode that is present in non-deaerated solutions [24, 27, 34]. Mechanism of deposition is considered almost independent of the electrode material. As shown in Fig.8, oxygen is reduced on BDD at potentials close to the ones used to deposit ceria. The  $Ce^{3+}$  cations in proximity of to the electrode, can react following two different pathways: they can be hydrolysed by  $OH^-$  (Eq.6-7) or they can be oxidized by  $H_2O_2$  formed at the electrode(Eq.5), direct oxidation of  $Ce^{3+}$  precursors by molecular oxygen is thermodynamically not permitted[].



Then  $Ce(OH)_3$  can be further oxidized following Eq.8 or precipitate as is, Ce (IV) hydroxyl complex hydrolyses to give  $CeO_2$  that precipitates on the electrode surface as shown in Eq.9:



To summarize, we can obtain two phases, cerium (III) hydroxide obtained through direct precipitation of  $Ce^{3+}$  precursors and cerium (IV) oxides obtained through oxidation by hydrogen peroxide. According to the Pourbaix diagram below (Fig.9),  $Ce(OH)_3$  is the favourite precipitate obtained within the potential window we explored (red band). These deposition potentials were chosen to insure sufficient nitrate reduction to obtain an adequate alkalinisation of the solution which is essential to precipitate cerium species. Henceforth we report data for three potentials (-1, -1.5 and -2V vs SCE) that are representative of three regions a, b, c present in Fig.8 corresponding to equation 1, 2 and 3. Onset potential of curve on Fig.8 agree with standard potential for Eq.1 (blue line in the Pourbaix diagram), deposition potential adopted here were more negative than nitrate reduction even when strong alkalinisation occurred [35].

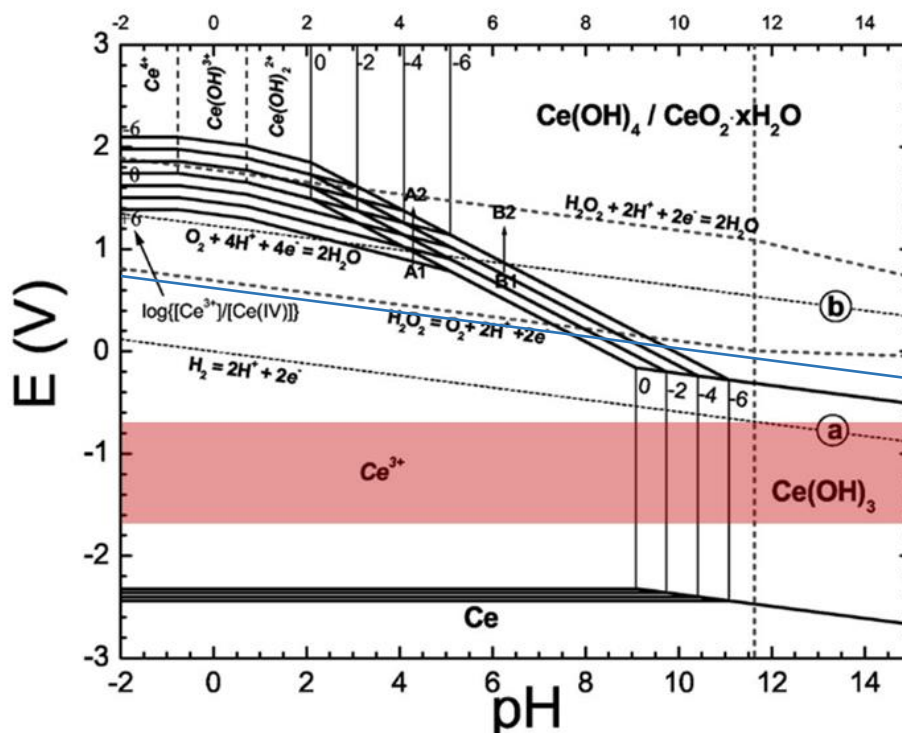


**Fig.9.** Pourbaix diagram for the Ce-H<sub>2</sub>O-H<sub>2</sub>O<sub>2</sub> system,[35]. Red band represents deposition potential window studied in this thesis and blue line shows Eq.1 pH dependence.

We used electro-precipitation technique to deposit thin films of ceria from solutions containing 0.1M NaNO<sub>3</sub> and concentrations from 0.1mM to 4mM of Ce(NO<sub>3</sub>)<sub>3</sub>. pH of the solution was between 4 and 5. Electrodeposition of CeO<sub>2</sub> on either BDD or other supporting materials was carried out in a two-compartment cell. The working electrode and a Pt wire counter electrode were placed in the main cell compartment; a Saturated Calomel Electrode (SCE) was in a compartment separated by a glass frit. Working electrode was placed mainly face up, but we performed depositions with working electrode immersed vertically in the solution obtaining same results in terms of film thickness and morphology. This also excludes that our deposits were made of species precipitated in the bulk solution.

As we already reported shifting, between different supports means that potential deposition must be changed to have the desired currents; Pt containing catalyst, for example, are more active toward nitrate reduction and therefore to obtain the same deposition charge and a similar film thickness, we have to apply a consistently less negative potential. Fig.10a shows two LSV registered in the deposition bath over BDD and Pt electrodes; in the figure insert are reported two potentiostatic electrodepositions that gave similar currents though they were obtained with two very different potentials ( $\Delta = 800\text{mV}$ ). To conclude to have the same grade of alkalisation, i.e. electroprecipitation, over different electrodes we have to directly impose the same deposition current or applying a potential that will lead to the same stationary current.

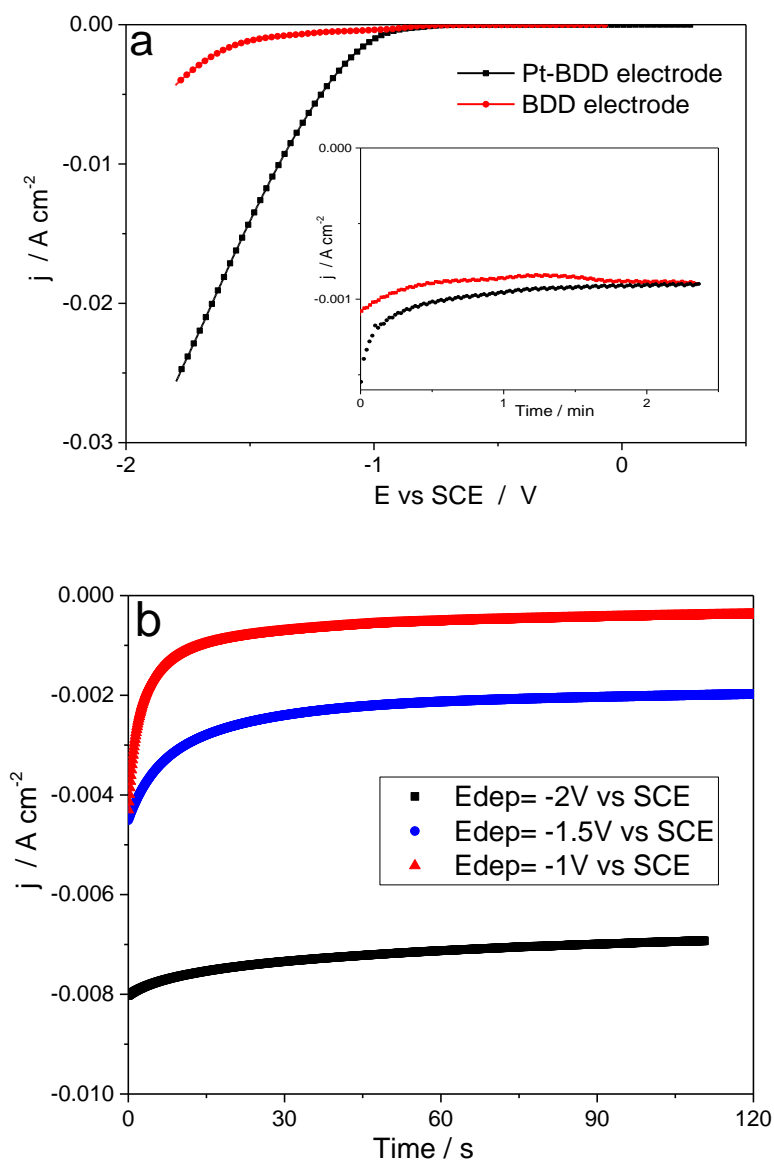


**Fig.10.** (a) LSV registered with two different electrodes in 0.1M NaNO<sub>3</sub>, 0.4mM Ce(NO<sub>3</sub>)<sub>3</sub>, scan rate 50 mV/s, in the insert there are two chronoamperograms registered at E=-1V and -1.5V vs SCE respectively for Pt-BDD and BDD in the same solution (b) chronoamperograms registered at different potentials with BDD electrode in 0.1M NaNO<sub>3</sub>, 4mM Ce(NO<sub>3</sub>)<sub>3</sub>,

In Fig.10b, we reported three chronoamperograms registered on BDD electrodes at three different potential -1, -1.5 and -2V vs SCE. Currents after a rapid drop due to double layer charging and to the local increase of pH on the electrode, reach a steady state, indicating that the process of deposition is not hindered by the formation of a poorly conductive film. In addition to potential effect, we studied relation between deposition charge and film thickness. Table 1 resume data collected for upper and lower limits of deposition potential, regarding deposition charge and film thickness measured by SEM analysis. We can observe that less negative potentials give higher deposition efficiencies compared to more negative potentials. Such behaviour seems to be in contrast with the fundamental rule that the more negative is the potential the higher is the pH close

to electrode and the higher is the deposition rate. This rule is probably true until is reached a potential where HER becomes heavily favorited. At that point, gas evolution on the electrode probably limits the precipitation process by mechanically removing precipitates or by preventing precipitation at the electrode.

**Table1**

Deposition Potential V vs SCE	Deposition Charge C/cm <sup>2</sup>	Film thickness
-1	-0.02	≈7nm
-1	-0.1	≈300nm
-1	-0.2	≈1μm
-2	-0.4	≈10nm
-2	-1	≈30nm

### 1.3. Characterization of CeO<sub>2</sub>-BDD electrodes

#### 1.3.1. Morphology

We performed several experiments changing potentials and deposition charges. Control of the charge allows to obtain homogeneous films with thickness from 10-20 nm to several hundreds of nm. To characterize films we performed SEM-EDX analysis directly on the surface of electrode and of cross sections after breaking the electrode. EDX analysis confirm the presence of cerium on the electrodes.

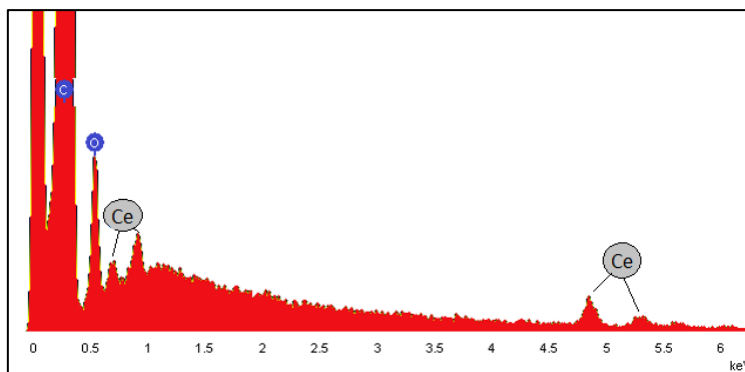


**Fig.11.** EDX analysis of a BDD modified with a ceria layer

Over a certain thickness, film growth became fibrous and present vast cracks; as literature report, this seems to be quite common for thick layers, cracking is due to drying, or support/film interaction during deposition process itself [24, 25, 27, 29]. In general, higher thickness gave less compact film with numerous cracks due to drying process (refer to chapter 2). Fig.12 show a cross section image registered with secondary (a, c) and backscattered (b) electrons detectors to highlight ceria film distribution on BDD surface. Decreasing thickness to few hundreds of nanometres let us obtain deposits that showed some major porosity but could become unstable and brittle after prolonged electrolysis with marked gas evolution. As evidence by SEM in fig 12d, we were able to modify quite uniformly large area BDD electrodes.

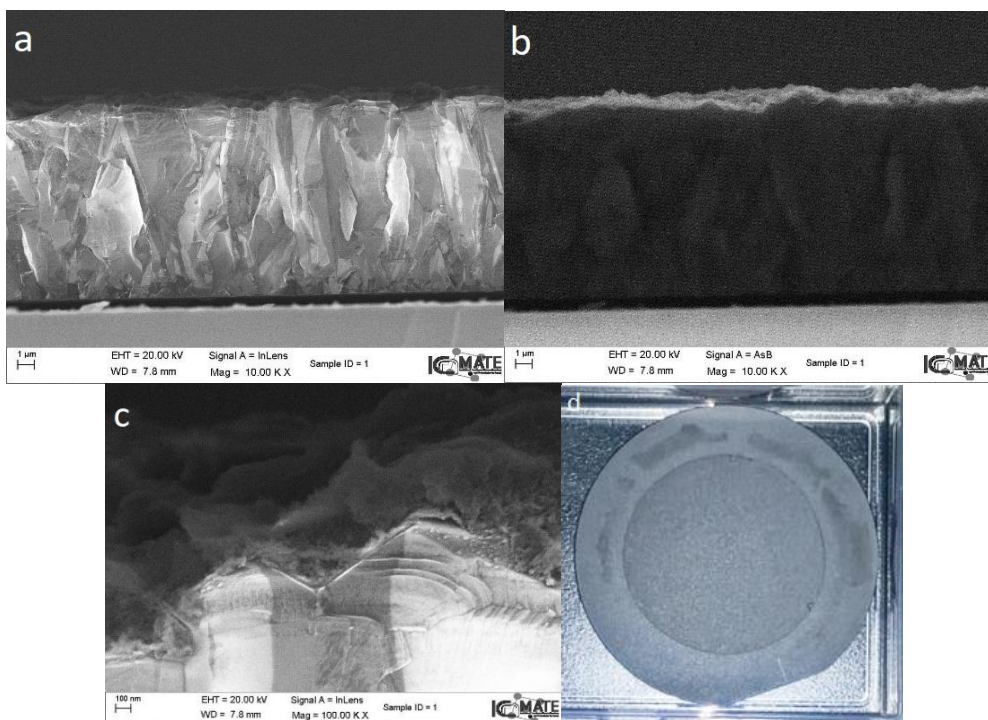


**Fig.12.** (a, b, c) SEM cross section images of CeO<sub>2</sub>-BDD electrodes obtained at  $E_{dep}=-1V$  vs SCE,  $Q_{dep}=-0.1C/cm^2$ , (d) image of an as prepared BDD electrode modified with ceria (OD= 50 mm), ceria deposit is visible in the center.

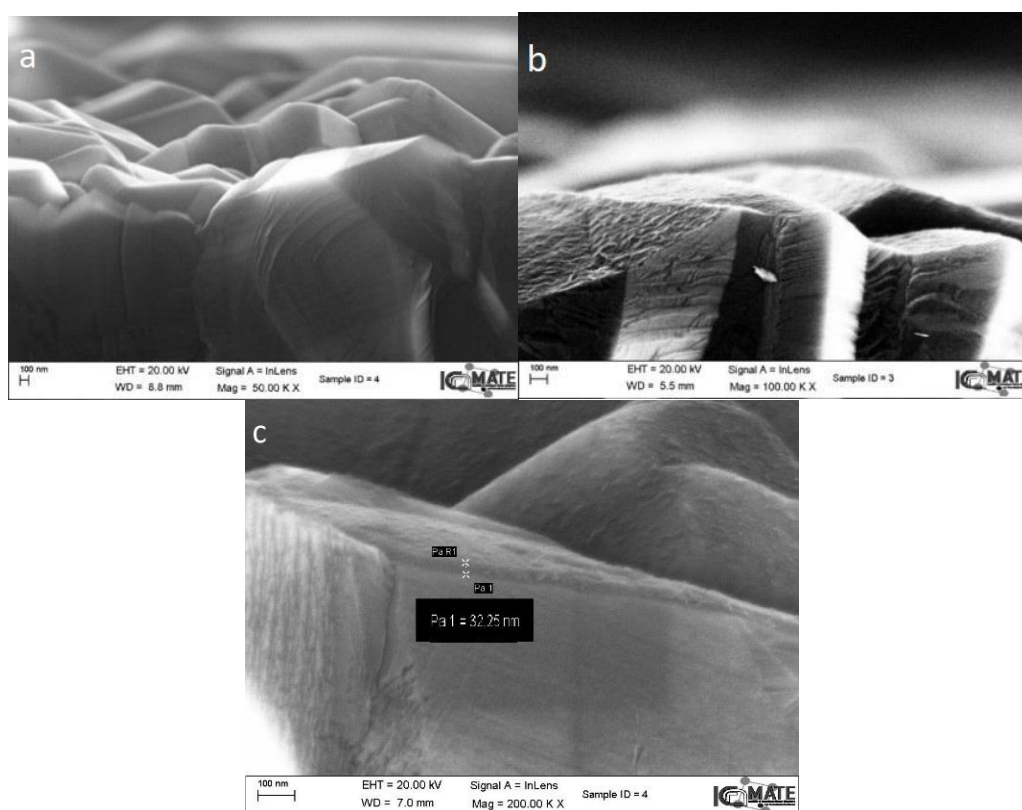


**Fig.13.** SEM cross section images of (a) bare BDD electrode, (b) CeO<sub>2</sub>-BDD electrodes obtained at  $E_{dep}=-1V$  vs SCE,  $Q_{dep}=-0.02C/cm^2$ , (c) CeO<sub>2</sub>-BDD electrodes obtained at  $E_{dep}=-2V$  vs SCE,  $Q_{dep}=-1C/cm^2$ .

Reducing deposition charges, we can obtain film with thickness of few nanometres, cross section images show that they are uniform and compact and with a very good adhesion to BDD surface. In addition, they are very stable remaining unaltered after prolonged experiment also in flow electrochemical cells. Fig. 13 a and b show BDD as such and CeO<sub>2</sub> modified BDD, while Fig.13c shows an in situ evaluation of thickness performed while registering SEM images.

TEM analysis were performed on samples that were prepared by gently removing films from the surface and transferring on transparent conductive grids. They showed CeO<sub>2</sub> nanoparticles agglomeration with an average dimension of less than 4 nm. Cubic structure Fm-3m with crystal dimension a=5,4 Å was confirmed by Fourier Transform Analysis (FTT) of Fig.14a. Particle size distribution is reported in Fig.14b, data highlight a very narrow particle distribution.

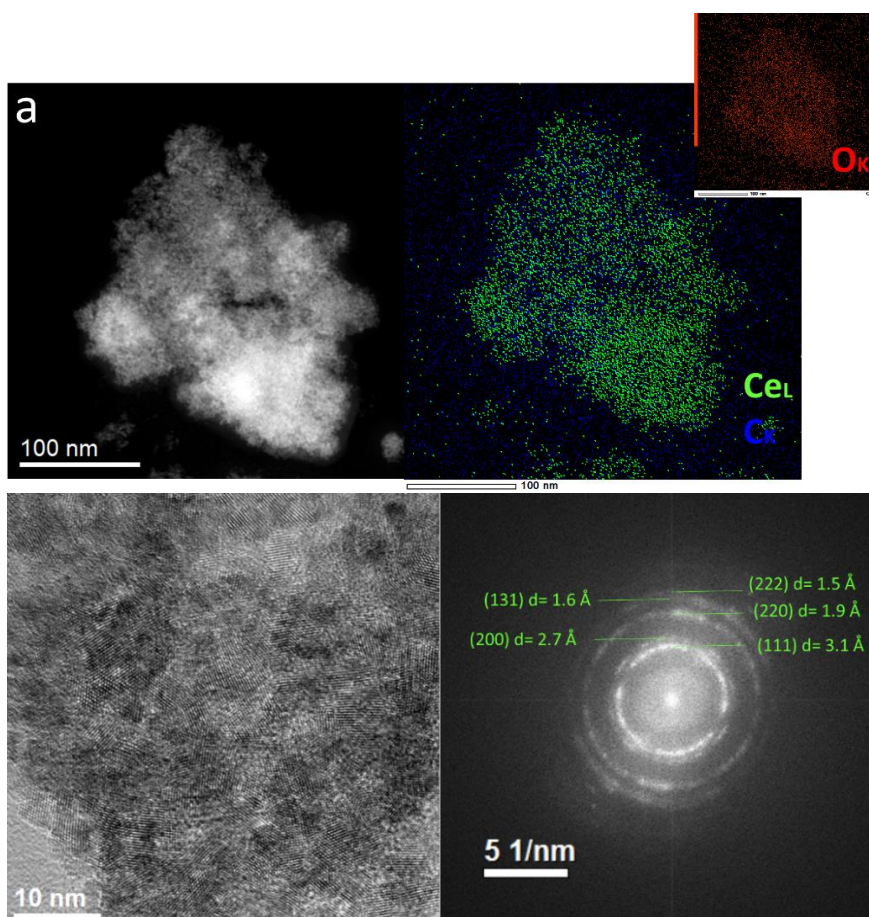


**Fig.14a.** (a top) HRTEM image and corresponding EDX map for C, O, and Ce (a bottom) HRTEM image of CeO<sub>2</sub> film obtained at E=-1V with corresponding FTT.

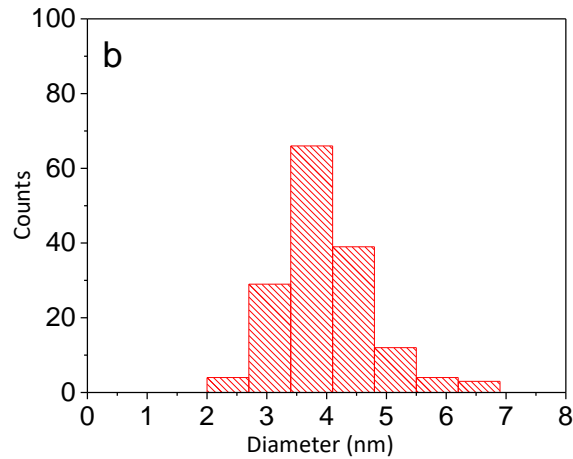


**Fig.14b.** Size distribution plot of ceria nanoparticle.

FTT analysis of single nanoparticles confirmed the Fm-3m cubic structure of CeO<sub>2</sub> deposits. Nanocrystallinity is a key feature because conductivity of cerium oxide is related to its microstructure; preferential sites for electronic conductivity are known to be distributed on grain boundaries and nanocrystalline phase materials show a much higher grain boundary density compared to microcrystalline materials. This means that conductivity increases with decreasing of crystal size [36]. In addition, it is widely recognized that for electrocatalysis, nanoparticles supply large numbers of reactive coordination sites due to their high number of surface atoms located at steps, corners and edges. Fig.15 shows HRTEM image with a highlighted magnification of a single nanoparticle and its FFT analysis for a deposit obtained at E<sub>dep</sub>=-2V.

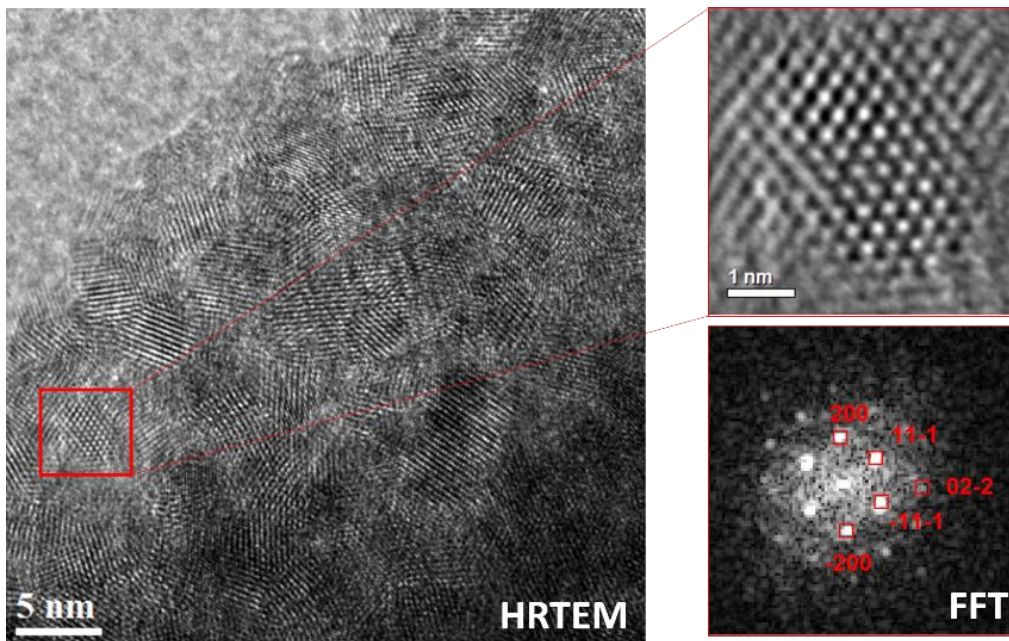


**Fig.15.** HRTEM image of CeO<sub>2</sub> film obtained at E<sub>dep</sub>=-2V with a higher magnification zoom and an FFT analysis.

Fig.16 show a single nanoparticle analysis with zone axis (110) and (111) obtained with deposition potential of  $E_{dep}=-1V$ ; we did not observe any difference in terms of crystal size with different deposition potentials.

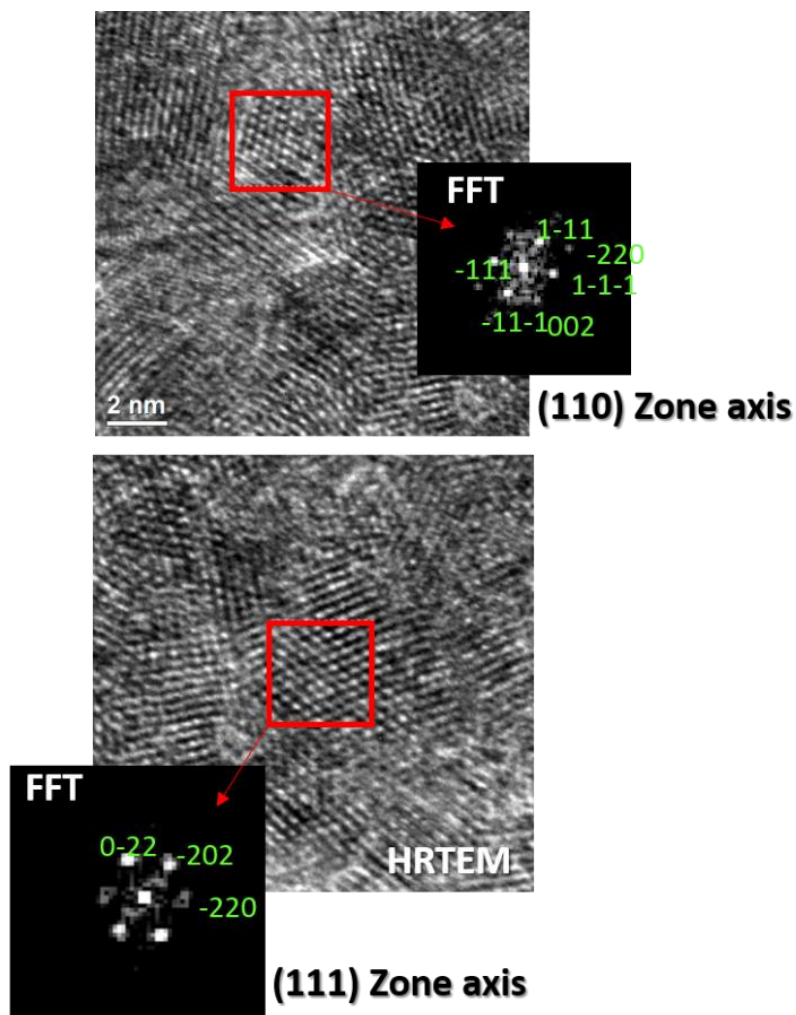


**Fig.16.** HRTEM image of single CeO<sub>2</sub> nanoparticle obtained at  $E_{dep}=-1V$  with a higher magnification zoom and an FFT analysis of different zone axis.

### 1.3.2. Phase characterization

The two parameters that we can control during electroprecipitation are applied potential and concentration of species in the deposition bath. Nitrate is the species that induce alkalisation on the electrode so it must be concentrated enough to be reduced at a constant rate during experiments. This will guarantee the same pH profile for the whole duration of experiment that in general is in the order of minutes. Changing Ce<sup>3+</sup> concentration we can control the rate of nucleation of cerium species precipitating on the electrode. Looking deep into literature and comparing data with our experiments it seems that the higher the concentration of Cerium precursors the bigger is the size of crystals obtained and the more dendritic is the morphology obtained. Our experiments here revealed also that there is no effect of Ce<sup>3+</sup> concentration on composition.

To study the phase composition of films in function of deposition potential we registered some diffraction spectra directly on film deposited on BDD and on powders obtained by mechanically removing the material from BDD surface. Such sample preparation was necessary due to very small thickness and low density of ceria deposits. XRD spectra of deposits obtained at  $E_{\text{dep}}=-1\text{V}$  vs SCE (Fig.17 a) shows only one phase with a low grade of crystallinity, confirming the existence of a nanometric powder, attributed to  $\text{CeO}_2$  cubic fluorite-type structure [37]. For a sample prepared at  $E_{\text{dep}}=-2\text{V}$  vs SCE (Fig.17 b), we obtained reflections attributed to ceria but also some weak reflections that corresponded to peaks related to  $\text{Ce}(\text{OH})_3$  [38]. We can affirm that when we used a more negative potential we obtained the simultaneous formation of Ceria and cerium hydroxide. Our opinion is that when high cathodic current are employed the partial reduction of oxygen to hydrogen peroxide, that is diffusion limited, become restricted by competitive nitrate reduction, that is present in higher concentrations and by HER that is not limited by diffusion at all. With a limited amount of hydrogen peroxide produced, precipitation process can take both pathways, through eq.6 and through eq.7 producing, in addition to ceria, some cerium hydroxide.

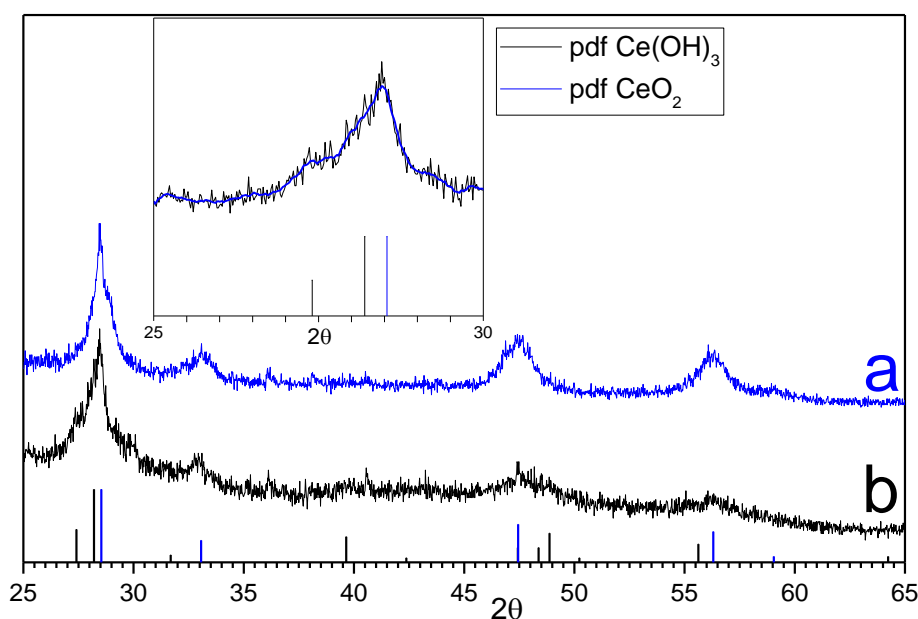


**Fig.17.** XRD patterns of  $\text{CeO}_2$  films removed from BDD electrodes obtained at (a)  $E_{\text{dep}}=-1\text{V}$  and (b) at  $E_{\text{dep}}=-2\text{V}$ . Insert show a zoom of most intensive reflections of pattern (b).

As stated in I4, ceria exceptional activity in catalysis is related to oxygen vacancies. Composition of ceria films are reported to be dependent on electroprecipitation potential [30, 33]. Some authors report that ceria defectiveness depends on deposition potential; i.e. when a more negative potential is applied a lower oxygen stoichiometry is obtained. To the best of our knowledge, nobody studied doping through the control of electrochemical deposition process. XPS analysis were performed on samples freshly prepared with the different potential values (-1V, -1.5V, -2V) and with different deposition charges. Photoelectron spectroscopy

has been systematically used to determine the electronic states of cerium in ceria [32, 39, 40]. Figure 18 shows the Ce 3d<sub>3/2,5/2</sub> spectra collected from electrodeposited films. The CeO<sub>2</sub> 3d-spectrum is composed of two multiplets that correspond to the spin-orbit split 3d<sub>5/2</sub> and 3d<sub>3/2</sub> core holes. On each spectra of Fig.18 we can distinguish peaks related to Ce 3d<sub>5/2-3/2</sub> doublet-pair of Ce(IV) coloured in grey and some features related to 3d<sub>3/2</sub>-3d<sub>5/2</sub> spin-orbit-split doublets which are characteristic for Ce(III) coloured in red.

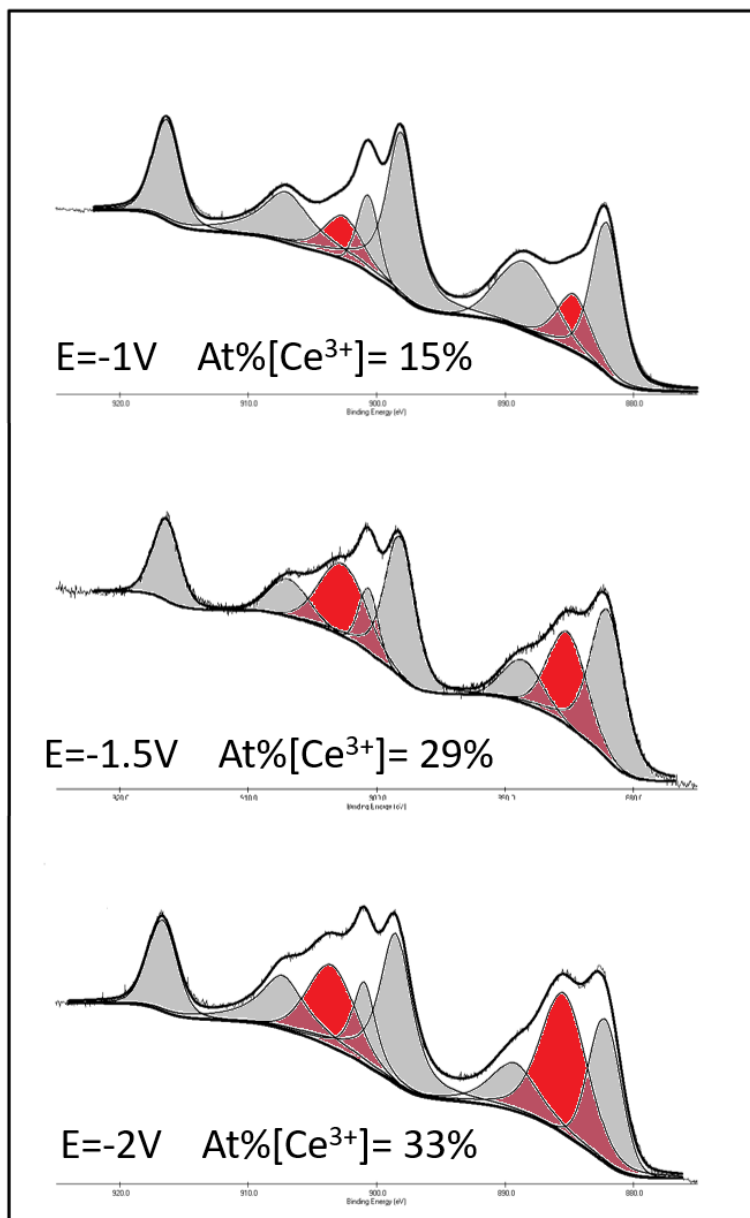


**Fig.18.** XPS high-resolution measurements and spectral fits of the Ce 3d<sub>3/2-5/2</sub> region.

In Fig.19 are shown spectra of O 1s for the three potentials; we can distinguish two peaks, one at 529 eV (blue) generated from lattice oxygen and one at 531 eV (grey) attributed to OH<sup>-</sup> and to oxygen vacancies. We can exclude nitrate adsorption or inclusion because nitrogen is not present in XPS wide energy scan.

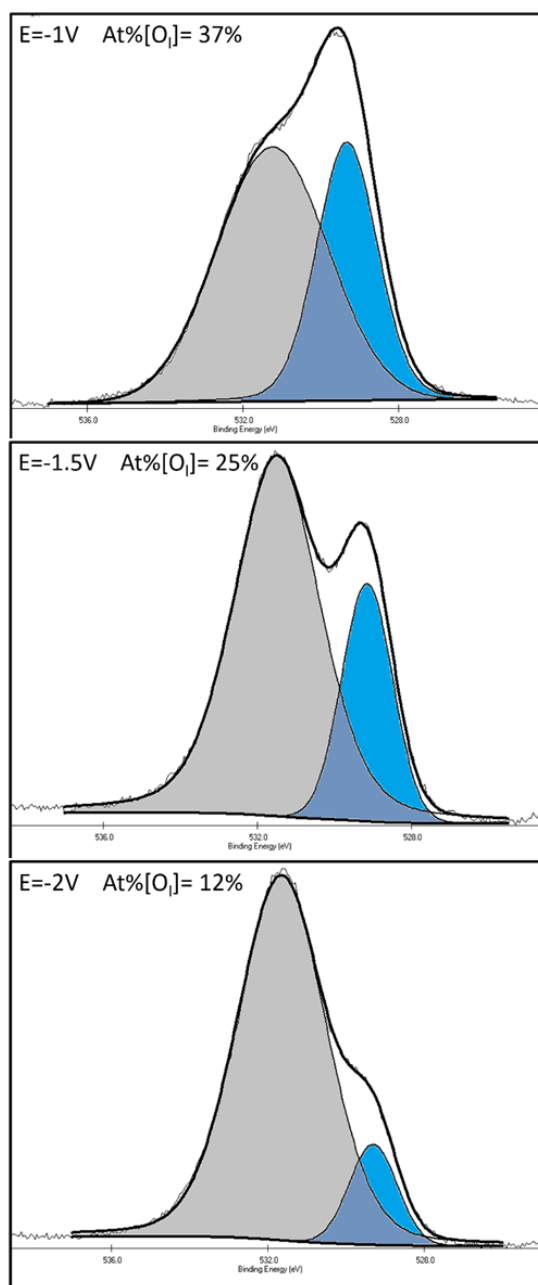


**Fig.19.** XPS high-resolution measurements and spectral fits of the O1s.

We integrated peaks area that were obtained by fitting XPS spectra with Gaussian-Lorentzian peak shape after subtracting background obtained with a Shirley-type function. Data is resumed in tab.2. In particular, we calculated  $CeO_x$  stoichiometry based on Ce(III) relative peak. Parameter x was calculated with following formula:

$$x = \frac{Ce(IV)At. \%}{100} \times 2 + \frac{Ce(III)At. \%}{100} \times 1.5$$

Where Ce(IV)At.% is the atomic percentage of  $Ce^{4+}$  ions, Ce(III)At.% is atomic percentage of  $Ce^{3+}$  ions, 2 and 1.5 represent, respectively, the oxygen stoichiometry of  $CeO_2$  and  $Ce_2O_3$ .

**Table 2**

Deposition Potential V vs SCE	Ce(III) from XPS At.%	Ce(IV) from XPS At.%	Lattice Oxygen O <sub>1s</sub> , XPS At.%	Parameter x on CeO <sub>x</sub>
-1	15	85	37	1.925
-1.5	29	71	25	1.85
-2	33	67	12	1.835

Decreasing the deposition potential we increased the level of oxygen vacancies. We suppose that their formation was partly due to the electrochemical reduction of Ce(IV) to Ce(III) during deposition process. As reported by Cummings and co-workers, electroprecipitated cerium (IV) species can be reduced in solution at potential around 0.2V vs SCE [41]. In our case film obtained is not fully reduced because electrochemical reduction of ceria is a process confined to the outer layers of a film; since precipitates are continuously deposited, only the outer layer it is exposed to the solution and for a very small time. Another consideration we made is related to the presence of the cerium hydroxide phase on sample prepared at -2V. In literature many authors reported that CeO<sub>x</sub> cubic phase is stable for  $2 > x > 1.7$  values [42], this exclude that electrochemical induced doping can generate a phase separation during electrodeposition to give cerium hydroxide. Unfortunately, we were not able to separate the contribution of oxygen vacancies and adsorbed species to 531 eV peak of O 1s, thus we were not able to quantify directly by integration, the ratio between lattice oxygen and oxygen related to vacancies. However we can see that the trend of lattice oxygen respect what we expected, it decreases when deposition potential becomes more negative. Ceria composition changes very little increasing the thickness of deposits confirming the formation of a layer with constant pH close to the electrode.

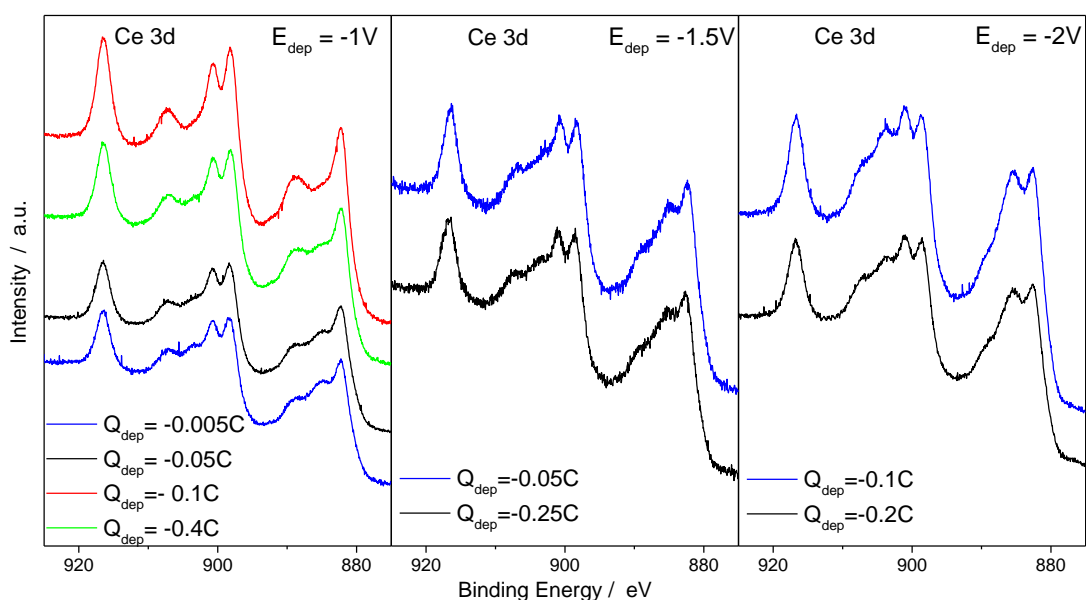
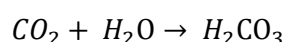


**Fig.20.** XPS high-resolution measurements of the Ce 3d<sub>3/2-5/2</sub> obtained at three potentials ( $E_{dep}$ ) each with different deposition charges ( $Q_{dep}$ ).

#### 1.4. CO<sub>2</sub> electrochemical reduction on Ceria-BDD electrodes

BDD electrodes main characteristic is their electrochemical inertness, however some groups studied electrochemical CO<sub>2</sub>RR on BDD. Einaga and co-workers obtained high faradaic yield toward different products like formaldehyde [43], methanol [44], and formic acid [45] in several media like seawater, buffered solutions, methanol or ammonia. They obtained high efficiency for electrolysis performed at potential no higher than -1.5V vs Ag/AgCl. Regarding formic acid their best results were obtained using a flow cell configuration, with yields close to 100% at potential of less than -2V vs Ag/AgCl. Cuellar and co-workers reduced CO<sub>2</sub> at potential from -1.5V to less than 2V vs Ag/AgCl without obtaining yield of CO higher than a few percent [46]. Saha and co-workers converted carbon dioxide to peroxy carbonate in KOH with high efficiency but with a cell voltage of over 5V [47]. Recently Birdja and Koper demonstrated that methanol and formic acid are obtained at BDD electrode at very negatives potentials, were HER induce a strong local alkalinisation of solution. They explain these results as due to base-catalysed Cannizzaro-type disproportionation reactions [48]. For potentials lower than -1V vs RHE, BDD produced methane. BDD modified electrodes were also used as a support for deposition of metal [49] and metal oxides [50] for CO<sub>2</sub> reduction. All these reports showed that BDD is not active toward CO<sub>2</sub>RR as transition metal are.

We report here our study of electrochemical CO<sub>2</sub> reduction on ceria modified BDD electrodes. The choice of electrolyte is usually quite important; in literature most of papers used KHCO<sub>3</sub> that once saturated with CO<sub>2</sub> form a buffered solution with pH between 6 and 10. We used a 0.1M KHCO<sub>3</sub> concentration that lead to a buffer pH=6.8. This electrolyte has also the peculiarity to act as a reservoir for aqueous CO<sub>2</sub>, thanks to the following equilibria:



This choice is ideal for prolonged electrolysis but it is problematic when a voltammetric study of process is necessary; without CO<sub>2</sub> saturation pH is over 8 so all reaction that are pH dependant shift their equilibrium potentials and compare electrode activity with or without CO<sub>2</sub> becomes complicated. In addition, as stated by Hori [2], comparing results obtained from voltammetries has a major drawback: CO<sub>2</sub> reduction and HER usually proceed at the same potentials and are not independent of each other. For example, when CO covers the electrode, can happen that current densities are lower than in argon-saturated solution. Therefore, without any evidence that the current corresponds to a single electrochemical reaction, it is misleading to consider only current/potential measurements. In our electrolyte, currents in some regions can be higher in N<sub>2</sub> saturated than in CO<sub>2</sub> saturated solutions. This is due to the fact that: i) in carbonate pH is different once

the solution is saturated with CO<sub>2</sub> and ii) electrodes could be covered with adsorbed CO during the reduction of CO<sub>2</sub> to CH<sub>4</sub> or other hydrocarbons in aqueous media, electrode surface becomes blocked and total current and competitive HER are both suppressed. So we decided to study CO<sub>2</sub>RR on both 0.1M KHCO<sub>3</sub> (CB) and 0.1M phosphate buffer solutions (PB) at the same pH of 6.8 with the aim not to compare different current densities but to verify the presence of reduction peaks that can be ascribed to CO<sub>2</sub>RR process. Electrolyte must be pre-electrolysed before use to guarantee an elevated degree of purity; it is known that even small amount of metal impurities can lead to surface interference with electrochemical reactions. This is even more important for electrodes with small area, like the ones we used, that without pre-electrolysis are poisoned very quickly. BDD as such, as previously described, is almost inactive toward CO<sub>2</sub> reduction for potential above -1V vs RHE. Low scan rate LSV in Fig.21 show curves for BDD and ceria-BDD electrodes in carbonate solution with and without CO<sub>2</sub>. CO<sub>2</sub> reduction at bare BDD begins around -1.15V vs Hg|HgO, while LSV registered in N<sub>2</sub> saturated solution present onset of HER at potentials around -1.25 vs Hg|HgO.

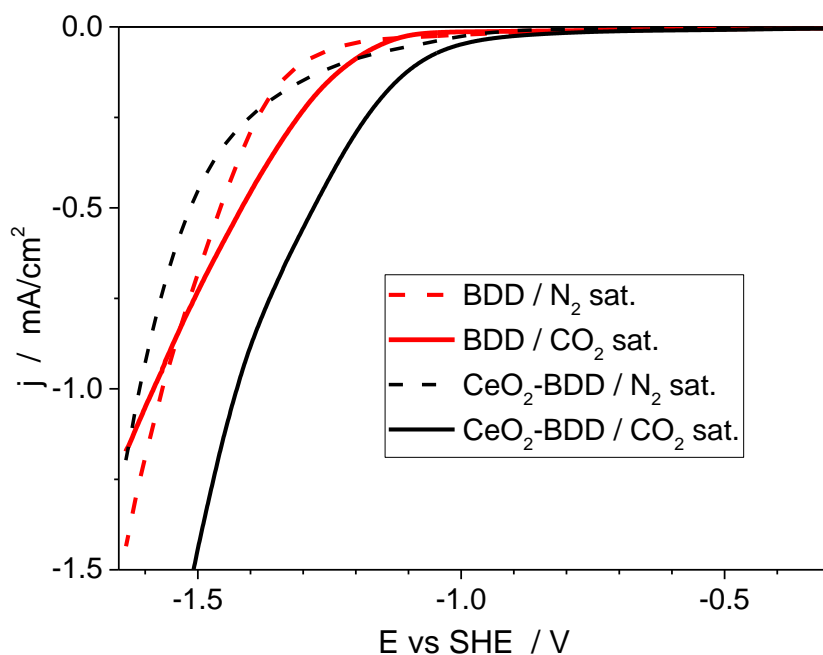


**Fig.21.** LSV of BDD (red) and CeO<sub>2</sub>-BDD (black) electrodes in 0.1M KHCO<sub>3</sub> with or without CO<sub>2</sub> saturation registered at 1mV/s.

On ceria-modified electrodes, there is a weak reduction peak that begins at -0.45V vs SHE (i) in CO<sub>2</sub> saturated solution that is not present in N<sub>2</sub>. This is something never observed in previous report [14] and it is something that drove our attention. LSV on Ceria modified BDD, in both carbonate solution (Fig.22a) and phosphate buffer solution (Fig.22b), show the weak peak (i) that we attributed to CO<sub>2</sub> electrochemical reduction. In phosphate solution there is also a reduction system at around -0.9V (ii) present both in the presence and in the absence of CO<sub>2</sub>, that in our opinion is related to the reduction of cerium phosphate formed by reacting

with  $\text{Ce}^{3+}$  present in the deposit. Cummings and co-workers reported a higher reduction potential for cerium phosphate and no  $\text{Ce}^{3+}/\text{Ce}^{4+}$  system without presence of phosphate, but this can be explained by the very different nature of ceria deposits that they obtained and maybe by presence of binders on the electrode [41]. When we registered a CV in CB solution (Fig.22c) we obtained, similarly to Nagarale and co-workers, a system due to  $\text{Ce}^{3+}/\text{Ce}^{4+}$  equilibrium, confirming that when negative potentials typical of  $\text{CO}_2$  reduction are applied, all  $\text{Ce}^{3+}$  produced react with phosphate inactivating the electrode surface [51].

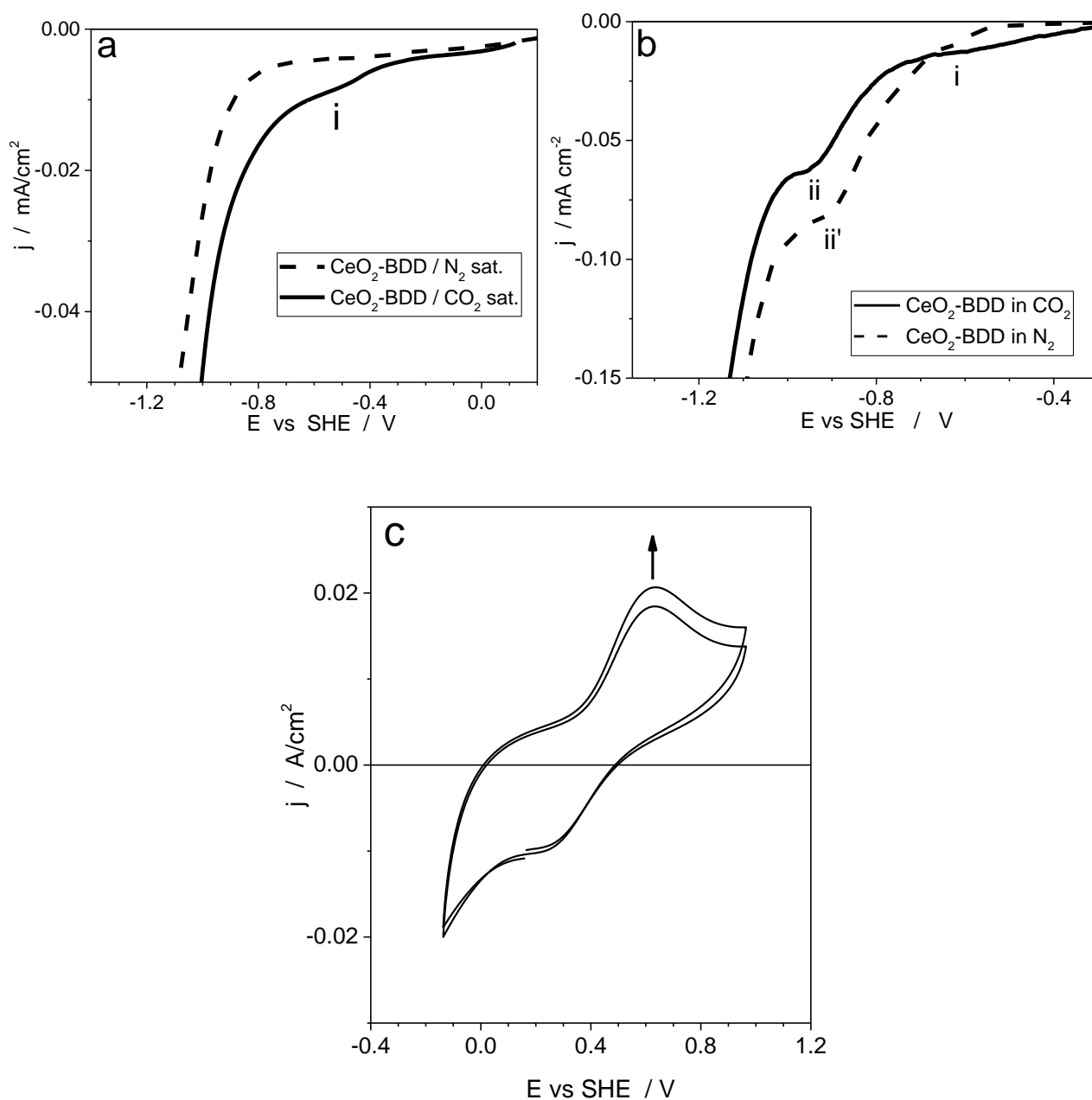


**Fig.22.** LSV of  $\text{CeO}_2$ -BDD electrodes registered at 1mV/s with or without  $\text{CO}_2$  saturation in (a) 0.1M  $\text{KHCO}_3$  (b) 0.1M phosphate buffer solution. (c) CV of a  $\text{CeO}_2$ -BDD electrode in 0.1M  $\text{KHCO}_3$  with a scan rate of 10mV/s.

Chronoamperograms in Fig.23 were recorded during prolonged electrolysis experiments. To collect quantity of products that could be analysed with sufficient accuracy, we performed CO<sub>2</sub> electrolysis for at least 16h. Solution was kept under CO<sub>2</sub> bubbling for all the duration of experiments but temperature was not, even so in the room there were small temperature variations. Current behaviours strongly depend on potential applied; for electrolysis at -0.44V, we can observe a slight activation of the electrode after several hours of polarization. For -0.59V electrolysis after initial stability, few hours long, current start to decay to reduce after 10 hours to almost 50% of initial values. Experiments at -0.736V show a very rapid decay during first few seconds that lead to low currents that decrease constantly.

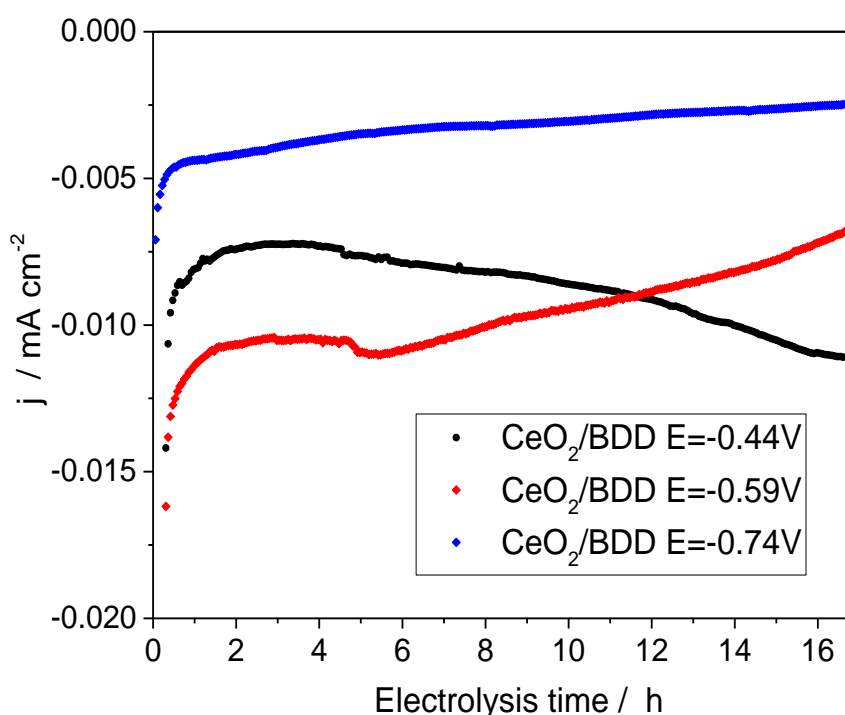


**Fig.23.** Chronoamperograms registered during CO<sub>2</sub> reduction at three different potentials (ref. SHE) in a CO<sub>2</sub> saturated 0.1M KHCO<sub>3</sub> solution on CeO<sub>2</sub>-BDD electrodes prepared at  $E_{\text{dep}} = -1\text{V}$ ,  $Q_{\text{dep}} = -0.02 \text{ C/cm}^2$ .

Electrolysis performed, at the same potential of -0.44V, on electrode with different compositions show very different current evolution. Opposite to the one with higher oxygen vacancies, the one obtained at  $E_{\text{dep}} = -2\text{V}$  show very poor stability, current after few hours decay almost to zero (Fig.24). When we compare product efficiency of the two electrodes, we see that both generate formate at low overpotential, but the latter in minor amount. This confirm how activity depend on oxygen deficiency of the ceria phase.

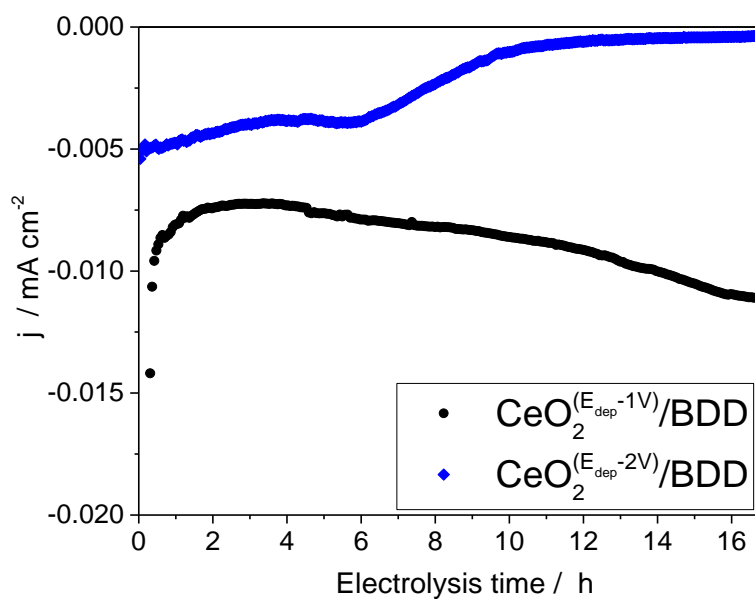


**Fig.24.** Chronoamperograms registered during CO<sub>2</sub> reduction at E=-0.44V vs SHE in a CO<sub>2</sub> saturated 0.1M KHCO<sub>3</sub> solution on CeO<sub>2</sub>-BDD electrodes prepared at E<sub>dep</sub>=-1V, Q<sub>dep</sub>=-0.02 C/cm<sup>2</sup> (black) and E<sub>dep</sub>=-2V, Q<sub>dep</sub>=-0.4 C/cm<sup>2</sup>

Products in liquid phase were analysed with ion chromatography as described in Appendix. An attempt to analyse gas phase was done with a micro gas chromatographer but cell geometry, in addition to low currents generated, prevented any reliable determination of CO or CH<sub>4</sub>, the only gas we measured was a small amount of hydrogen that, as expected, increased for increasing overpotential. Results, reported in Fig.25, show that maximum efficiency toward formic acid (>40%) was obtained at very low overpotential (≈40mV) with electrode with small ceria layers (10-20 nm). All electrolysis are referred to thin films electrodes, when we performed experiments with thicker films, no matter what their composition was, we obtained smaller currents. Reasons for this inactivity are related to poor conductivity, lower mechanical stability under operational conditions but also by limited diffusion of species from and to the electrode due to increased thickness of films. Increasing overpotential, the formate efficiency rapidly decrease. Some test performed on ceria deposited on glassy carbon electrode, even if they generated higher currents, did not produce formic acid at all at low overpotential. This could prove that ceria is fundamental acting as a co-catalyst adsorbing CO<sub>2</sub> on oxygen vacancies but it is BDD surface that reduces adsorbed CO<sub>2</sub> to formate. That oxygen vacancies play a fundamental role is evidenced also by the fact that films obtained at more negative potentials, that we know contain less oxygen vacancies than other deposits, showed lower efficiencies to formate.

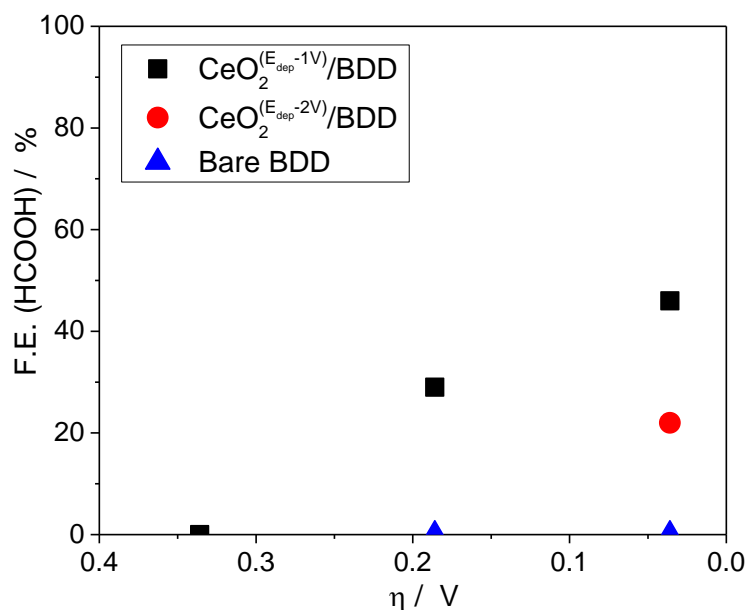


**Fig.25.** Formic acid faradaic efficiency calculated from CO<sub>2</sub> electrochemical reduction experiments at different overpotentials.

The mechanism we propose is related to ceria adsorption capability. Ceria supplied CO<sub>2</sub> to the BDD electrode surface where H termination or perhaps metal impurities that deposited during electrolysis reduce CO<sub>2</sub> to formate at low overpotentials (green pathway). At higher overpotentials it produce some species that poison the electrode, presumably CO (orange pathway), leading to a suppression of formate production [52]. This speculation, although supported by some different ceria-substrate combination experiments, could be confirmed only by in situ spectroscopic techniques that can evidence CO<sub>2</sub> low temperature adsorption on oxygen vacancies or with a deep study of intermediates of reaction; this last option should be problematic due to low turnover frequencies obtained with this system.

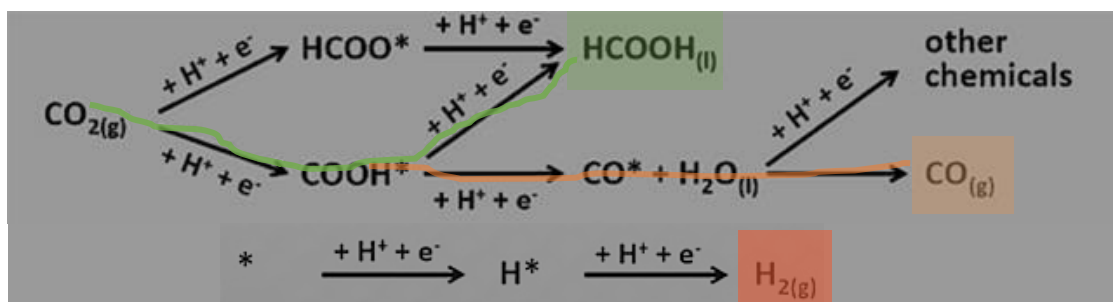


**Fig.26.** Scheme of different reaction pathways for CO<sub>2</sub> electrochemical reduction.

### 1.5. Conclusions & Perspectives

We studied the evolution of ceria film obtained with electrochemical base generation method in function of deposition charge and potential, and correlated such parameters with morphology, phase formation and oxygen vacancies density. Prolonged CO<sub>2</sub> electrolysis showed low but stable currents. We evidenced how strong composition and morphology of electroprecipitated ceria can influence the activity toward CO<sub>2</sub> leading to a very promising conversion to formate at very low overpotential. We suggested a mechanism of reaction were both CO<sub>2</sub> adsorption on ceria and BDD hydrogenation are necessary to obtain CO<sub>2</sub> conversion. To further confirmation of mechanism proposed, some in-situ analysis of Ce<sup>3+</sup>/Ce<sup>4+</sup> interconversion could enable to verify CO<sub>2</sub> adsorption and analysis of reaction intermediates can clarify reaction steps involved in the reduction process at BDD surface. Potential match of ceria with other metals that are active toward CO<sub>2</sub> reduction can lead to an increase of selectivity and a decrease of overpotential required. A manuscript related to results reported in this chapter is under preparation.

## 1.6. Bibliography

1. Jong Suk Yoo, Rune Christensen, Tejs Vegge, Jens K. Nørskov, Felix Studt, Theoretical Insight into the Trends that Guide the Electrochemical Reduction of Carbon Dioxide to Formic Acid, *ChemSusChem* 9 (2016) 358–363.
2. Hori Y. In: Vayenas C.G., White R.E., Gamboa-Aldeco M.E. *Modern Aspects of Electrochemistry* n°42 (Springer, New York 2008).
3. M. Azuma, K. Hashimoto, M. Hiramoto, M. Watanabe, T. Sakata, Electrochemical Reduction of Carbon Dioxide on Various Metal Electrodes in Low-Temperature Aqueous  $\text{KHCO}_3$  Media, *J. Electrochem. Soc.*, 137 (1990) 1772–1778.
4. Lei Zhang, Zhi-Jian Zhao, Jinlong Gong, Nanostructured Materials for Heterogeneous Electrocatalytic  $\text{CO}_2$  Reduction and their Related Reaction Mechanisms, *Angew. Chem. Int. Ed.* 56 (2017) 11326 – 11353.
5. Na Han, Yu Wang, Hui Yang, Jun Deng, Jinghua Wu, Yafei Li & Yanguang Li, Ultrathin bismuth nanosheets from in situ topotactic transformation for selective electrocatalytic  $\text{CO}_2$  reduction to formate, *Nature Communications* 9 (2018) 1320.
6. Yihong Chen, Matthew W. Kanan, Tin Oxide Dependence of the  $\text{CO}_2$  Reduction Efficiency on Tin Electrodes and Enhanced Activity for Tin/Tin Oxide Thin-Film Catalysts, *J. Am. Chem. Soc.* 134 (2012) 1986 – 1989.
7. Zhiqiao He, Jie Shen, Zhili Ni, Juntao Tang, Shuang Song, Jianmeng Chen, Li Zhao, Electrochemically created roughened lead plate for electrochemical reduction of aqueous  $\text{CO}_2$ , *Catalysis Communications* 72 (2015) 38–42.
8. Y. Hori, H. Wakebe T. Tsukamoto, O. Koga, Electrocatalytic process of  $\text{CO}$  selectivity in electrochemical reduction of  $\text{CO}_2$  at metal electrodes in aqueous media, *Electrochim. Acta* 39 (1994) 1833.
9. Chang Hoon Lee, Matthew W. Kanan, Controlling  $\text{H}^+$  vs  $\text{CO}_2$  Reduction Selectivity on Pb Electrodes, *ACS Catal.* 5 (2015) 465–469.
10. Xiaoquan Min, Matthew W. Kanan, Pd-Catalyzed Electrohydrogenation of Carbon Dioxide to Formate: High Mass Activity at Low Overpotential and Identification of the Deactivation Pathway, *J. Am. Chem. Soc.* 137 (2015) 4701–4708.
11. Ruud Kortlever, Ines Peters, Sander Koper, Marc T. M. Koper, Electrochemical  $\text{CO}_2$  Reduction to Formic Acid at Low Overpotential and with High Faradaic Efficiency on Carbon-Supported Bimetallic Pd–Pt Nanoparticles, *ACS Catal.* 5 (2015) 3916–3923.
12. Melchionna, M., Bracamonte, M.V., Giuliani, A., Nasi, L., Montini, T., Tavagnacco, C., Bonchio, M., Fornasiero, P., Prato, M., Pd@TiO<sub>2</sub>/carbon nanohorn electrocatalysts: Reversible  $\text{CO}_2$  hydrogenation to formic acid, *Energy Environ. Sci.* 11 (2018) 1571–1580.
13. Dunfeng Gao, Hu Zhou, Fan Cai, Dongniu Wang, Yongfeng Hu, Bei Jiang, Wen-Bin Cai, Xiaoqi Chen, Rui Si, Fan Yang, Shu Miao, Jianguo Wang, Guoxiong Wang, and Xinhe Bao, Switchable  $\text{CO}_2$  electroreduction via engineering active phases of Pd nanoparticles, *Nano Res.* 10 (2017) 2181–2191.
14. Boni, Alessandro (2016) *Electrochemistry of Nanocomposite Materials for Energy Conversion*, Alma Mater Studiorum Università di Bologna. <http://dx.doi.org/DOI 10.6092/unibo/amsdottorato/7510>
15. Tribidasari A. Ivandini, Yasuaki Einaga, Polycrystalline boron-doped diamond electrodes for electrocatalytic and electrosynthetic applications, *Chem. Commun.* 53 (2017) 1338.
16. Macpherson J., A practical guide to using boron doped diamond in electrochemical research *Phys. Chem. Chem. Phys.* 17 (2015) 2935–2949.
17. Yasuaki Einaga, Diamond electrodes for electrochemical analysis, *J Appl Electrochem* 40 (2010) 1807–1816.
18. J.-P. Lagrange, A. Deneuve, E. Gheeraert, Activation energy in low compensated homoepitaxial boron-doped diamond films, *Diamond and Related Materials* 7 (1998 ) 1390–1393.
19. John H. T. Luong, Keith B. Maleb, Jeremy D. Glennon, Boron-doped diamond electrode: synthesis, characterization, functionalization and analytical applications, *Analyst* 134 (2009) 1965–1979.

20. Switzer, Electrochemical Synthesis and Sintering of Nanocrystalline Cerium(IV) Oxide Powders, *J. Am. Ceram. Soc.* 78 (1994) 981.
21. A. J. Aldykiewicz, Jr., A. J. Davenport, H. S. Isaacs, Studies of the Formation of Cerium-Rich Protective Films Using X-Ray Absorption Near-Edge Spectroscopy and Rotating Disk Electrode Methods, *J. Electrochem. Soc.* 143 (1996) 147-154.
22. Y. Zhou, Jay A. Switzer, Growth of Cerium(IV) oxide films by the electrochemical generation of base method, *Journal of Alloys and Compounds* 237 (1996) 1-5.
23. F.-B. Li, R. C. Newman, G. E. Thompson, In situ atomic force microscopy studies of electrodeposition mechanism of cerium oxide films: nucleation and growth out of a gel mass precursor, *Electrochim. Acta*, 42 (1997) 2455-2464.
24. J. Creus, F. Brezault, C. Rebere, M. Gadouleau, Synthesis and characterisation of thin cerium oxide coatings elaborated by cathodic electrolytic deposition on steel substrate, *Surface & Coatings Technology* 200 (2006) 4636 – 4645.
25. Y. Hamlaoui, F. Pedraza, L. Tifouti, Investigation of electrodeposited cerium oxide based films on carbon steel and of the induced formation of carbonated green rusts, *Corrosion Science* 50 (2008) 2182–2188.
26. V. Fernandes, J. J. Klein, W. H. Schreiner, N. Mattoso, D. H. Mosca, Electrodeposition of Nanocrystalline CeO<sub>2</sub> on Si(001), *J. Electrochem. Soc.* 156 (2009) E199-E204.
27. Y. Hamlaoui, F. Pedraza, C. Remazeilles, S. Cohendoz, C. Rébéré, L. Tifouti, J. Creus, Cathodic electrodeposition of cerium-based oxides on carbon steel from concentrated cerium nitrate solutions Part I. Electrochemical and analytical characterisation, *Materials Chemistry and Physics* 113 (2009) 650–657.
28. Y. Hamlaoui, L. Tifouti, C. Remazeilles, F. Pedraza, Cathodic electrodeposition of cerium based oxides on carbon steel from concentrated cerium nitrate. Part II: Influence of electrodeposition parameters and of the addition of PEG, *Materials Chemistry and Physics* 120 (2010) 172–180.
29. B. Bouchaud, J. Balmain, G. Bonnet, F. Pedraza, Optimizing structural and compositional properties of electrodeposited ceria coatings for enhanced oxidation resistance of a nickel-based superalloy, *Applied Surface Science* 268 (2013) 218– 224.
30. B. Bouchaud, J. Balmain, G. Bonnet, F. Pedraza, Correlations between electrochemical mechanisms and growth of ceria based coatings onto nickel substrates, *Electrochimica Acta* 88 (2013) 798–806.
31. D. Stoychev, Corrosion protective ability of electrodeposited ceria layers, *J. Solid State Electrochem.* 17 (2013) 497–509.
32. F. Faisal, A. Toghian, I. Khalakhan, M. Vorokhta, V. Matolin, Jörg Libuda, Characterization of thin CeO<sub>2</sub> films electrochemically deposited on HOPG, *Applied Surface Science* 350 (2015) 142–148.
33. P. Bocchetta, M. Santamaria, F. Di Quarto, Cerium Oxyhydroxide Nanowire Growth via Electrogeneration of Base in Nonaqueous Electrolytes, *Electrochem. Solid-State Lett.* 11 (2008) K93-K97
34. Myriam Nobial, Olivier Devos, Oscar Rosa Mattos, Bernard Tribollet, The nitrate reduction process: A way for increasing interfacial pH, *Journal of Electroanalytical Chemistry* 600 (2007) 87–94.
35. Pu Yu, Scott A. Hayes, Thomas J. O’Keefe, Matthew J. O’Keefe, James O. Stoffer, The Phase Stability of Cerium Species in Aqueous Systems II. The Ce(III/IV)–H<sub>2</sub>O–H<sub>2</sub>O<sub>2</sub>/O<sub>2</sub> Systems. Equilibrium Considerations and Pourbaix Diagram Calculations, *J. of The Electrochem. Soc.*, 153 (2006) C74-C79.
36. Y.-M. Chiang, E.B. Lavik, I. Kosacki, H.L. Tuller, Nonstoichiometry and Electrical Conductivity of Nanocrystalline CeO<sub>2-x</sub>, *Journal of Electroceramics* 1 (1997) 7-14.

37. ICDD Card 34-0394.
38. ICDD Card 74-0665.
39. Yuting Luo, Juan Li, Jie Zhu, Ye Zhao, Xuefeng Gao, Fabrication of Condensate Microdrop Self-Propelling Porous Films of Cerium Oxide Nanoparticles on Copper Surfaces, *Angew. Chem. Int. Ed.* 54 (2015) 4876–4879.
40. Eric Beche, Patrice Charvin, Danielle Perarnau, Stephane Abanades, Gilles Flamant, Ce 3d XPS investigation of cerium oxides and mixed cerium oxide ( $Ce_xTi_yO_z$ ), *Surf. Interface Anal.* 40 (2008) 264–267.
41. Charles Y. Cummings, Susan J. Stott, Michael J. Bonné, Karen J. Edler, Pauline M. King, Roger J. Mortimer, Frank Marken, Underpotential surface reduction of mesoporous  $CeO_2$  nanoparticle films, *J Solid State Electrochem.* 12 (2008) 1541-1548.
42. M. Ricken, J. Nijlting, I Riess, Specific heat and phase diagram of nonstoichiometric ceria ( $CeO_{2-x}$ ) *Journal of Solid State Chemistry* 54 (1984) 89-99.
43. Nakata, K., Ozaki, T., Terashima, C., Fujishima, A., Einaga, Y, High-yield electrochemical production of formaldehyde from  $CO_2$  and seawater, *Angew. Chem. Int. Ed.* 53 (2014) 871–874.
44. Jiwanti, P.K., Natsui, K., Nakata, K., Einaga, Y, Selective production of methanol by the electrochemical reduction of  $CO_2$  on boron-doped diamond electrodes in aqueous ammonia solution, *RSC Adv.* 6 (2016) 102214-102217.
45. Keisuke Natsui, Hitomi Iwakawa, Norihito Ikemiya, Kazuya Nakata, Yasuaki Einaga, Stable and Highly Efficient Electrochemical Production of Formic Acid from Carbon Dioxide Using Diamond Electrodes *Angew. Chem. Int. Ed.* 57 (2018) 2639–2643.
46. Nayra Sofia Romero Cuellar, Kerstin Wiesner-Fleischer, Olaf Hinrichsen, Maximilian Fleischer, Electrochemical Reduction of  $CO_2$  in Water-Based Electrolytes  $KHCO_3$  and  $K_2SO_4$  Using Boron Doped Diamond Electrodes, *ChemistrySelect* 3 (2018) 3591 – 3595.
47. Madhu Sudan Saha, Tsuneto Furuta, Yoshinori Nishiki, Conversion of carbon dioxide to peroxy carbonate at boron-doped diamond electrode, *Electrochemistry Communications* 6 (2004) 201–204.
48. Yuvraj Y. Birdja, Marc T. M. Koper, The Importance of Cannizzaro-Type Reactions during Electrocatalytic Reduction of Carbon Dioxide, *J. Am. Chem. Soc.* 139 (2017) 2030-2034.
49. Prastika K. Jiwanti, Keisuke Natsui, Kazuya Nakata, Yasuaki Einaga, The electrochemical production of  $C_2/C_3$  species from carbon dioxide on copper-modified boron-doped diamond electrodes, *Electrochimica Acta* 266 (2018) 414-419.
50. Nicolae Spataru, Kenichi Tokuhira, Chiaki Terashima, Tata N. Rao, Akira Fujishima, Electrochemical reduction of carbon dioxide at ruthenium dioxide deposited on boron-doped diamond, *Journal of Applied Electrochemistry* 33 (2003) 1205–1210.
51. R. K. Nagarale, U. Hoss, A. Heller, Mixed-Valence Metal Oxide Nanoparticles as Electrochemical Half-Cells: Substituting the Ag/AgCl of Reference Electrodes by  $CeO_{2-x}$  Nanoparticles, *J. Am. Chem. Soc.* 134 (2012) 20783-20787.
52. Jong Suk Yoo, Rune Christensen, Tejs Vegge, Jens K. Nørskov, Felix Studt, Theoretical Insight into the Trends that Guide the Electrochemical Reduction of Carbon Dioxide to Formic Acid, *ChemSusChem* 9 (2016) 358-363.

## CHAPTER 2: ceria for gas phase catalysis

### 2.1 Introduction

In a recent paper our group, in collaboration with the Combustion Research Institute of CNR, has reported some results on the low/medium temperature catalytic combustion of methanol on Pt-modified Fecralloy foams prepared by electrodeposition [1]. That paper resemble to other applications of the electrochemical preparation of heterogeneous catalysts for high temperature applications that we have done during last few years. Results reported there, suggested that the activation of oxygen molecules on specific metal oxide sites, such as  $\text{FeO}_x$  of Fecralloy support, closely interacting with Pt particles played a synergic role in the catalytic oxidation process. A solution to improve this interaction consists of employing a deliberately deposited oxide with intrinsically good properties as a catalyst or co-catalyst, instead of oxides spontaneously formed on the Fecralloy surface. In this way, we will enhance the interaction between oxide and Pt particles to favour synergic effects.

Core-shell catalysts, consisting of active (noble) metal nanoparticles surrounded by porous oxides, have drawn much attention because of their enhanced activity and (thermal) stability in several catalytic processes [2,3] such as the oxidation of CO [4-5] and hydrocarbons [7-10], the water-gas shift [11], the  $\text{CO}_2$  reforming of methane [12,13], as well as in photocatalysis [14] and electrocatalysis [3,16]. Interactions of metal particles with oxide supports can radically enhance the performance of supported catalysts [17,18]: high catalytic activity is normally ascribed to the formation of particularly active sites at the noble metal-metal oxide interface [2,17,19,20], whose surface area may become very large when nanometric metal cores are encapsulated by porous oxide shells. Ceria, as anticipated in the introduction, is a very attractive candidate to embed noble metal nanoparticles since it generally displays a marked promoting effect [20,21], apart from its own catalytic activity [22,23]. The thermal stability of catalysts based on core-shell particles depends on their ability to withstand extensive morphological changes at high temperatures. Under such conditions, unprotected metal nanoparticles are prone to undergo aggregation [14, 24], to minimize their surface energy, even when dispersed on high surface area supports. This results in the loss of catalytic active centers, degradation of performance and even inactivation [25]. However, the physical separation by the oxides shells can help noble metal nanoparticles to retain their original shape, size, and catalytic activity [2,10,14] and limit their surface diffusion. Since ceria has exceptional crystallographic stability over wide ranges of conditions, with a melting temperature of 2400 °C, the synthesis of Pt core -  $\text{CeO}_2$  shell catalysts, stable at high temperature, has become a very active research area in material science [2-8].

The production of structured catalytic reactors with core-shell noble metal–oxide nanoparticles as active materials meets two significant problems: (i) the synthesis of even small amounts of nanoparticles may be costly and cumbersome [1-11]; (ii) their transfer and firm anchoring directly onto structured reactors is still relatively unexplored [26]. Therefore, alternative routes are being explored. To meet practical needs of gas phase catalysis, noble metal-based catalysts must be dispersed and engineered into structured catalytic reactors. Fe-Cr-Al alloy foams, commercially known as Fecralloy, are ideal supports for catalytic reactors that must work at relatively high temperatures, because they possess outstanding heat and mass transfer properties, and excellent thermal stability [27-29]. The use of Fecralloy foams allows to reduce the size of the catalytic reactor needed to reach high conversions when dealing with a fast, highly exothermic and often diffusion limited process, such as catalytic combustion, and to design lightweight reactors with fast response during load variations and start-ups [28]. Materials combining CeO<sub>2</sub> and Pt have been prepared with various approaches to obtain catalysts for numerous reactions, including electrochemical oxidation of methanol or ethanol in direct alcohol fuel cells [29-35] and partial oxidation of methanol [36-38]. To the best of our knowledge, the use of Pt-CeO<sub>2</sub> catalysts in low-temperature catalytic combustion of methanol has never been reported.

Taking advantage of the metallic nature of Fecralloy foams, some simple preparation methods such as electrochemically induced precipitation [39-41], electrodeposition [42,43] and spontaneous deposition through a galvanic displacement reaction [44-45] have been shown capable to form well-dispersed and homogeneously distributed noble metal particles, strongly interacting with the substrate. Some difficulties might arise in the deposition onto 3D substrates, like Fecralloy foams, because their geometry might have a significant effect on the local pH increase required by the process. We are not aware of reports on the electrodeposition of CeO<sub>2</sub> onto 3D substrates. CeO<sub>2</sub> can be electrodeposited, both anodically [46,47] and cathodically [48-60], on a variety of substrates like e.g. Cu, Au, stainless and carbon steel, Si and Ni superalloys. The cathodic deposition of CeO<sub>2</sub> is particularly interesting for the modification of Fecralloy, as it can be realized in a potential range where this alloy is stable with respect to oxidation and dissolution of its metal components. Therefore, we studied only the cathodic deposition of CeO<sub>2</sub>.

To achieve a better control on the dimension and distribution of the Pt particles, pulsed deposition of Pt was used instead of constant-potential electrodeposition. Three preparation strategies were considered: simultaneous cathodic electrodeposition of Pt and CeO<sub>2</sub>, electrodeposition of CeO<sub>2</sub>, followed by electrodeposition of Pt, Electrodeposition of Pt, followed by electrodeposition of CeO<sub>2</sub>. In particular, after preliminary experiments, we focused on materials obtained with last strategy that was the only to give nanostructured catalysts with appropriate composition and morphologies. Research reported on this chapter, aimed at improving the performance of the methanol combustion over our catalysts. This process is technologically interesting because it is stable in a wide methanol/air operating range, produces ultra low

NO<sub>x</sub>, CO and VOC emissions, is suitable for micro burners and well suited for process intensification via integration with heat-exchangers [61-64]. Furthermore, we have extended investigations to activity and thermal stability measurements up to 800 °C during the oxidation of CO, which is considered a model reaction to test synthesized materials, due to its industrial importance and relevance to environmental issues.

## 2.2. Preparation of Pt-Fecralloy, CeO<sub>2</sub>-Fecralloy and CeO<sub>2</sub>-Pt-Fecralloy catalysts

### 2.2.1. Preliminary experiments

Fig. 1 shows linear voltammograms for the deposition onto Fecralloy sheet electrodes of either Pt, from a H<sub>2</sub>PtCl<sub>6</sub> solution, or CeO<sub>2</sub>, and related compounds, from two media containing either CeCl<sub>3</sub> and H<sub>2</sub>O<sub>2</sub> or Ce(NO<sub>3</sub>)<sub>3</sub>, respectively. In a 0.002 M H<sub>2</sub>PtCl<sub>6</sub> solution, a well-defined cathodic peak due to Pt deposition was seen at -0.685 V, during the first scan. The shoulder at less negative potential was possibly due to the reduction of oxides initially present on the Fecralloy electrode surface. In experiments aimed at depositing CeO<sub>2</sub>, a weak reduction current was observed using a 0.001 M CeCl<sub>3</sub> solution without H<sub>2</sub>O<sub>2</sub> (curve not shown). The curve recorded in 0.001 M CeCl<sub>3</sub>, 0.020 M H<sub>2</sub>O<sub>2</sub> solution showed a broad reduction peak centred at -0.57 V, due to H<sub>2</sub>O<sub>2</sub> reduction to hydroxyl ions which induced precipitation of Ce oxides/hydroxides. A sharper reduction peak, centred at -1.02 V was detected using a 0.1 M Ce(NO<sub>3</sub>)<sub>3</sub> solution, and ascribed to the reduction of nitrate ions, which also induced a local pH increase.

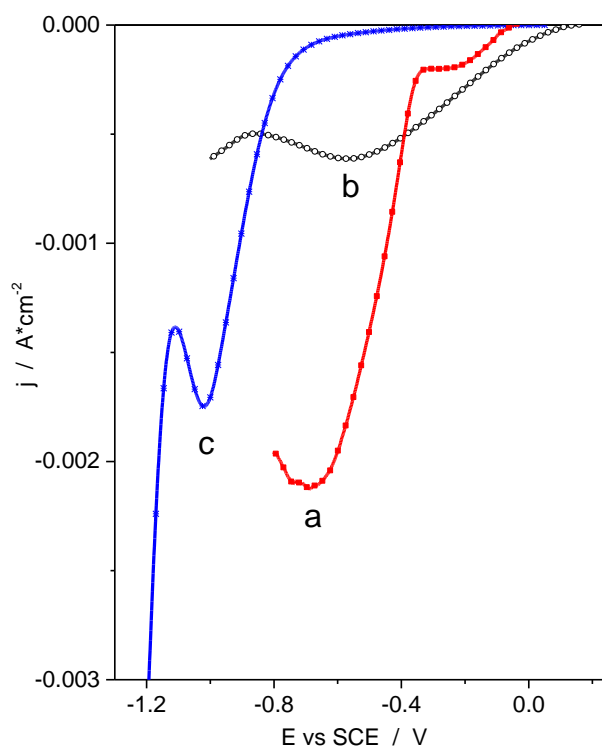
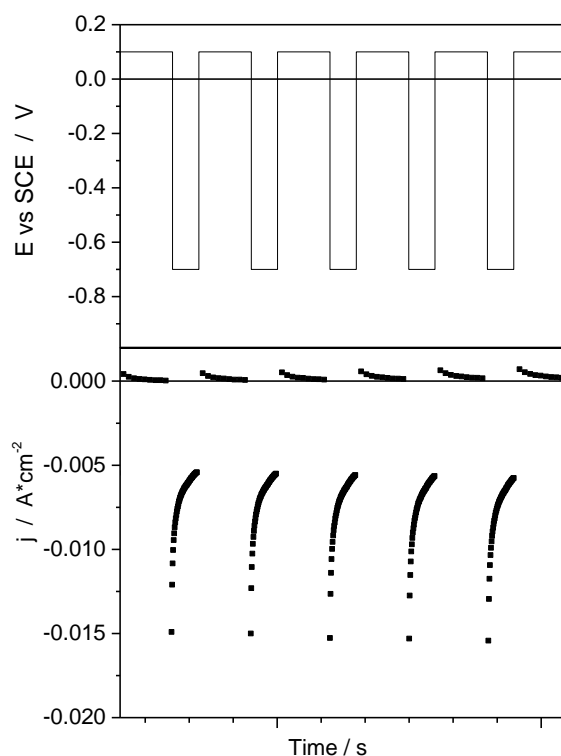


**Fig.1.** Linear sweep voltammograms recorded with Fecralloy sheet electrodes in 0.002 M H<sub>2</sub>PtCl<sub>6</sub> (a); 0.001 M CeCl<sub>3</sub>, 0.020 M H<sub>2</sub>O<sub>2</sub> (b) or 0.100 M Ce(NO<sub>3</sub>)<sub>3</sub> (c). Scan rate: 20 mV s<sup>-1</sup>.

These results showed that the deposition of Pt and CeO<sub>2</sub> could occur in compatible potential ranges, at pH values that were not markedly different (2 for Pt, between 4 and 5 for CeO<sub>2</sub>). Therefore, in principle, deposits containing both Pt and CeO<sub>2</sub> (or its precursors) might be formed onto Fecralloy cathodes in a single co-deposition step, similarly to the process described by Hassannejad et al. [65] for the cathodic electrodeposition of Ni-CeO<sub>2</sub> composites. However, our attempts to use the straightforward co-deposition approach were unsuccessful and did not allow a good control of the deposit properties. Thus, we reverted to procedures involving sequential depositions of the two components, optimizing both the deposition of Pt nanoparticles with well-controlled dimension and distribution and that of CeO<sub>2</sub> layers with appropriate thickness. Henceforth, we will call CeO<sub>2</sub>-Pt-Fecralloy the catalysts obtained by depositing first Pt then CeO<sub>2</sub>. Reverse deposition order was explored but abandoned because Pt electrodeposition onto CeO<sub>2</sub>-Fecralloy caused the removal of a significant fraction of the oxide initially present. Probably, the evolution of hydrogen bubbles that accompanied Pt deposition contributed to detaching the Ce-containing deposit. Each deposition process was initially studied on Fecralloy sheets, then on foam samples appropriate for the preparation of structured catalysts for combustion tests.

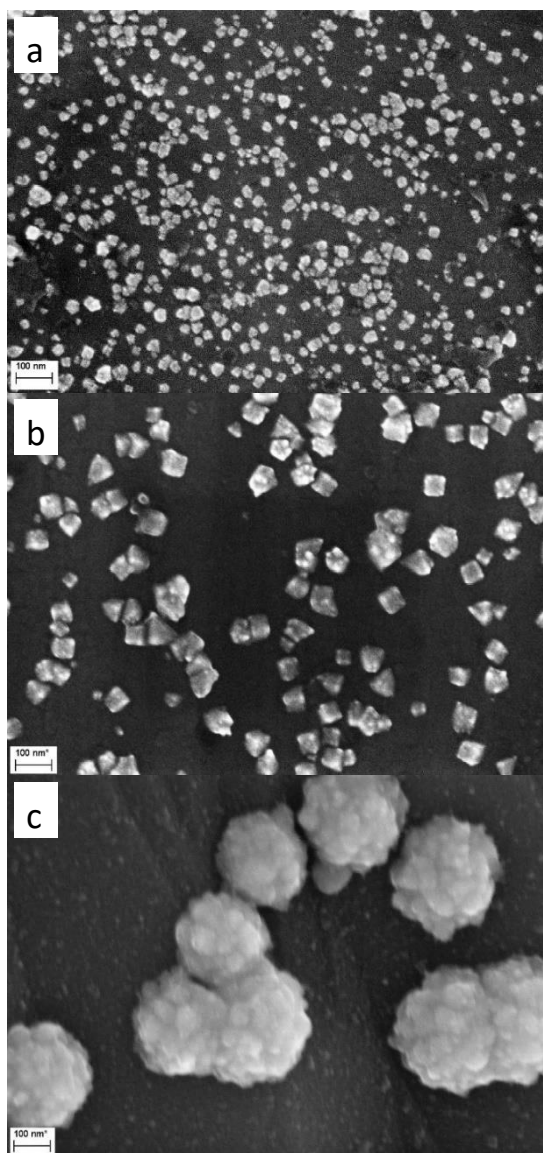
#### 2.2.2. Pulsed deposition of Pt onto Fecralloy

Our previous work on the cathodic deposition of Pt onto Fecralloy [1], as well as on the spontaneous deposition of Pd by galvanic displacement [44,45], showed a strongly heterogeneous reactivity of the foam surface. Noble metal nuclei formed on reactive positions and, upon prolonging the electrolyses (or galvanic displacement reaction), grew in size but not in number, i.e. no further nucleation of new particles was observed. Thus, some areas of the Fecralloy foams remained devoid of Pt particles. To achieve a more regular distribution of Pt particles, the noble metal was deposited by pulsing the potential between two values:  $E_1$  in the Pt deposition region and  $E_2$  where no deposition occurred. Fig. 2 shows, as an example, the potential program applied to a Fecralloy sheet electrode, with  $E_1 = -0.7$  V, held during 0.1 s, and  $E_2 = 0.1$  V, held during 0.2 s (top) and the resulting current transients (bottom). Besides double-layer charging, the reduction current flowing at  $E_1$  was due to Pt deposition and hydrogen adsorption (and possibly hydrogen evolution at lower  $E_1$  values); the weak oxidation current observed at  $E_2$  was due to hydrogen desorption and possibly to oxidation of Fecralloy. The current density measured at the end of the  $E_1$  pulse was higher (i.e. more negative) at more negative  $E_1$  potential and, at each potential, increased during the electrolysis because the noble metal deposition occurred on the Pt particles, already formed in the early stages of the process, whose surface area increased with time.



**Fig. 2.** Time dependence of the potential applied to a Fecralloy sheet electrode (top) and of the resulting current (bottom) during the pulsed electrodeposition of Pt from 0.002 M  $\text{H}_2\text{PtCl}_6$  solution.

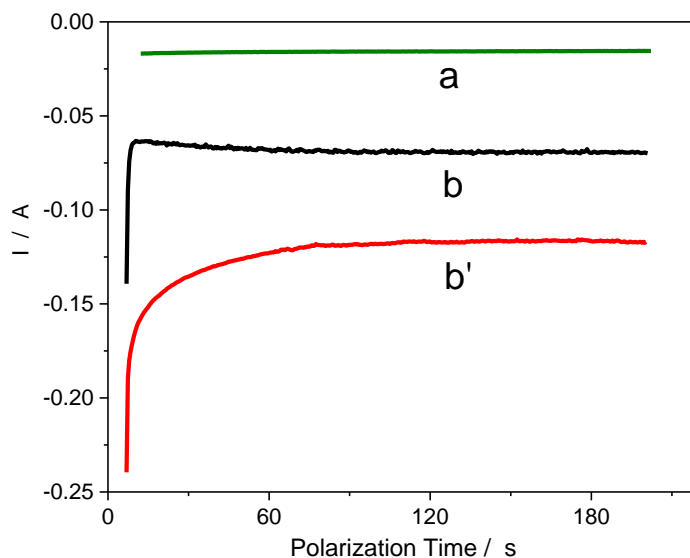
A large number of SEM images of Pt deposits on Fecralloy sheets or foams was collected. Fig. 3 shows a few examples. The comparison of Fig. 3a and 3b, relevant to sheet electrodes, highlights the effect of the  $E_1$  potential value. The number of nuclei per unit surface became larger as  $E_1$  was made more negative, up to reach an asymptotic value around  $E_1 \leq -1.0$  V, and was essentially independent of the number of pulses. The particles dimensions were narrowly distributed, were lower for more negative  $E_1$  potential, and increased with the number of pulses (images not shown). Comparison of Fig. 3b and 3c highlights the effect of the substrate. Pt particles formed onto Fecralloy sheet and foam electrodes under similar conditions (same  $E_1$  value, twice larger number of pulses for the foam) had different morphologies. They were close to cubes for the former and consisted of clusters of quasi-cubical particles for the latter. The nucleation of Pt deposits appeared to be less homogeneous on the foams than on the sheets. However, using foam electrodes, comparable deposits were formed on the struts of their outer and inner cells, with similar surface densities of Pt nuclei.



**Fig. 3.** SEM images of Fecralloy sheet (a,b) and foam (c) electrodes with Pt deposits formed in 0.002 M  $\text{H}_2\text{PtCl}_6$  solution, by varying  $E_1$  (a: -1.0 V; b, c: -0.7 V) and the number of pulses (a,b: 400; c: 800).

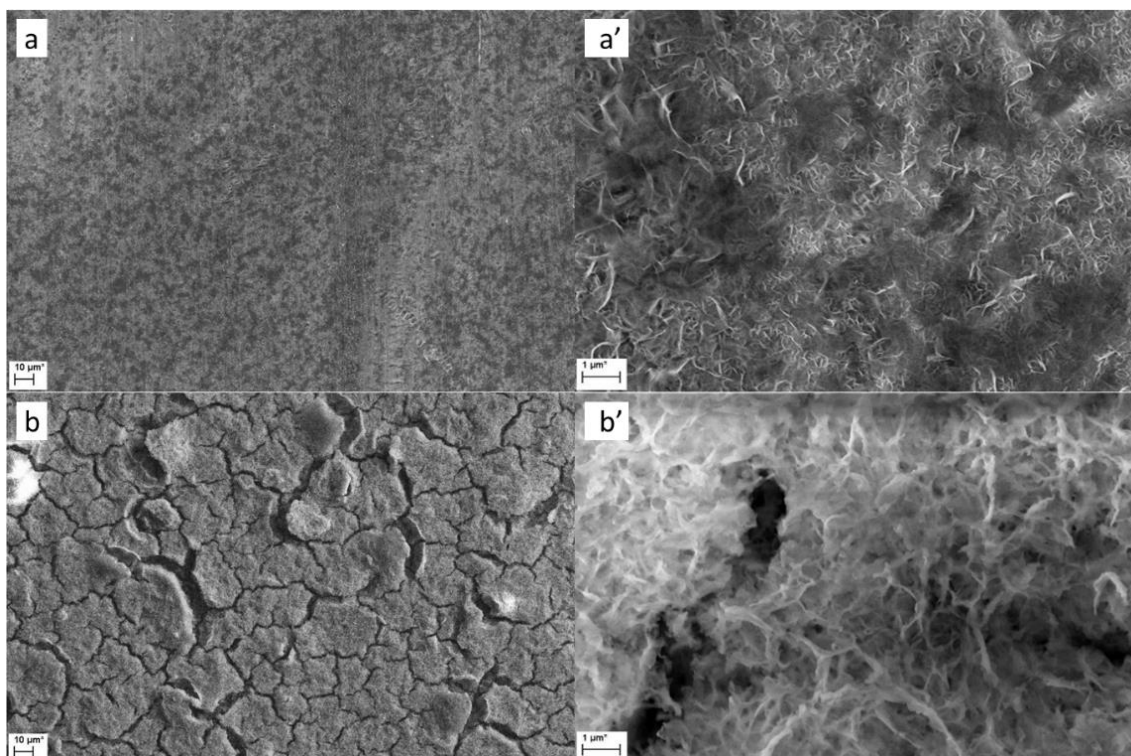
### 2.2.3 Cathodic deposition of $\text{CeO}_2$ onto Fecralloy

Fig. 4 shows chronoamperometric curves recorded with Fecralloy foams electrodes in either 0.001 M  $\text{CeCl}_3$ , 0,020 M  $\text{H}_2\text{O}_2$  (curve a) or in 0.100 M  $\text{Ce}(\text{NO}_3)_3$  (curve b). In both deposition media, after an initial fall, the current became essentially stable because the porous Ce-containing deposits did not induce a marked passivation of the electrodes. Curve b', relevant to  $\text{CeO}_2$  deposition onto Pt-modified Fecralloy sheets, henceforth called Pt-Fecralloy, is discussed below.



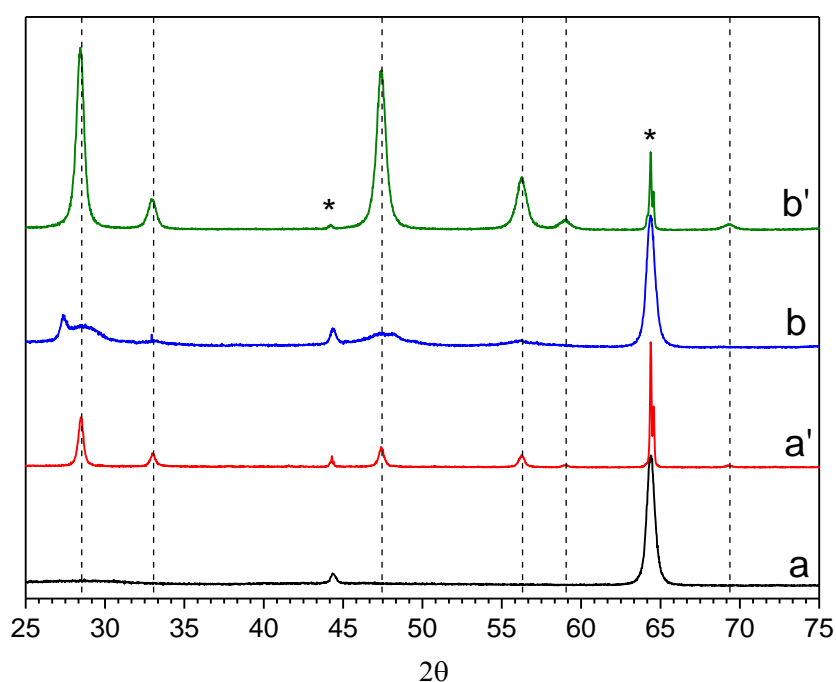
**Fig. 4.** Chronoamperometric curves recorded with Fecralloy (a, b) or Pt-Fecralloy (b') foam electrodes in 0.001 M  $\text{CeCl}_3$ , 0.020 M  $\text{H}_2\text{O}_2$  at -0.8 V (a), or 0.100 M  $\text{Ce}(\text{NO}_3)_3$  at -1.2 V (b, b').

Fig 5 shows that the morphology of the deposits formed onto Fecralloy sheets in the nitrate bath changed with the deposition charge, i.e. with the thickness of the layers, and was similar to that reported by other authors [51-55, 57-59]. Thinner deposits coated the Fecralloy sheets quite homogeneously, though not continuously, but thicker coatings became cracked. Comparable results were obtained using  $\text{CeCl}_3/\text{H}_2\text{O}_2$  solutions and, for both deposition baths, with Fecralloy foam electrodes.



**Fig. 5.**  $\text{CeO}_2$ -Fecralloy deposits formed on sheet electrodes in 0.100 M  $\text{Ce}(\text{NO}_3)_3$  solution with different deposition charges: 0.030 (a, a') and 0.90  $\text{C cm}^{-2}$  (b, b').

In order to assess the chemical nature of the deposits, they were submitted to XRD analyses, which results are shown in Fig. 6. Only reflections due to Fecralloy were seen in the diffractograms of as-prepared layers formed in  $\text{CeCl}_3/\text{H}_2\text{O}_2$  solutions (curve a). However, upon thermal treatment in air at  $600^\circ$  for 1 h, reflections at  $2\theta = 28.5, 33.0, 47.5, 56.3, 59.0$  and  $69.4^\circ$  became visible (curve a'). Both the positions and the relative intensities of these reflections agreed with those expected for  $\text{CeO}_2$  [66], and demonstrated the formation of the desired compound. The thermal treatment may have induced crystallization of amorphous  $\text{CeO}_2$  or conversion and crystallization of an amorphous precursor. Deposits formed in the  $\text{Ce}(\text{NO}_3)_3$  medium showed broad peaks due to  $\text{CeO}_2$  even before thermal treatment (curve b), which became sharper and markedly more intense when the samples were submitted to the thermal treatment described above (curve b'). A reflection at  $2\theta = 27.4^\circ$  in diffractogram b was due to  $\text{Ce}(\text{OH})_3$  [58, 67]. That reflection was no longer visible in diffractogram b' because the thermal treatment in air converted  $\text{Ce}(\text{OH})_3$  to  $\text{CeO}_2$ . Since, as described in the experimental section, all catalysts underwent a pre-treatment at  $600^\circ\text{C}$  in air, before methanol combustion tests, the results in Fig. 6 show that  $\text{CeO}_2$  was the only (crystalline) Ce-containing species in the catalysts, whichever the deposition bath used for their preparation. The following paragraphs refer to  $\text{CeO}_2$  deposits formed in nitrate solutions, because they are more stable and allow a better control of the Ce oxidation state, i.e.  $\text{CeO}_2$  vs.  $\text{Ce}(\text{OH})_3$ .



**Fig. 6.** X-ray diffractograms of deposits formed on Fecralloy sheets from 0.001 M  $\text{CeCl}_3$ , 0.020 M  $\text{H}_2\text{O}_2$  (a, a') or 0.100 M  $\text{Ce}(\text{NO}_3)_3$  (b, b'), either as-prepared (a,b) or after 1-hour thermal treatment in air at  $600^\circ\text{C}$  (a', b'). Reflections marked with \* are due to Fecralloy.

Pt particles were stable under  $\text{CeO}_2$  deposition conditions and were not removed from the Fecralloy substrate. Fig. 7 shows SEM images of  $\text{CeO}_2$ -Pt-Fecralloy samples. The formation of Ce-containing deposit,

assessed through EDS analyses, occurred both on the Pt particles and on the Fecralloy substrate. The b image, obtained with 500k x magnification, shows that a ca. 20 nm thick, probably discontinuous, oxide skin formed on the Pt particles, producing a sort of core-shell system. A discontinuous CeO<sub>2</sub> layer was visible on the Fecralloy substrate too.

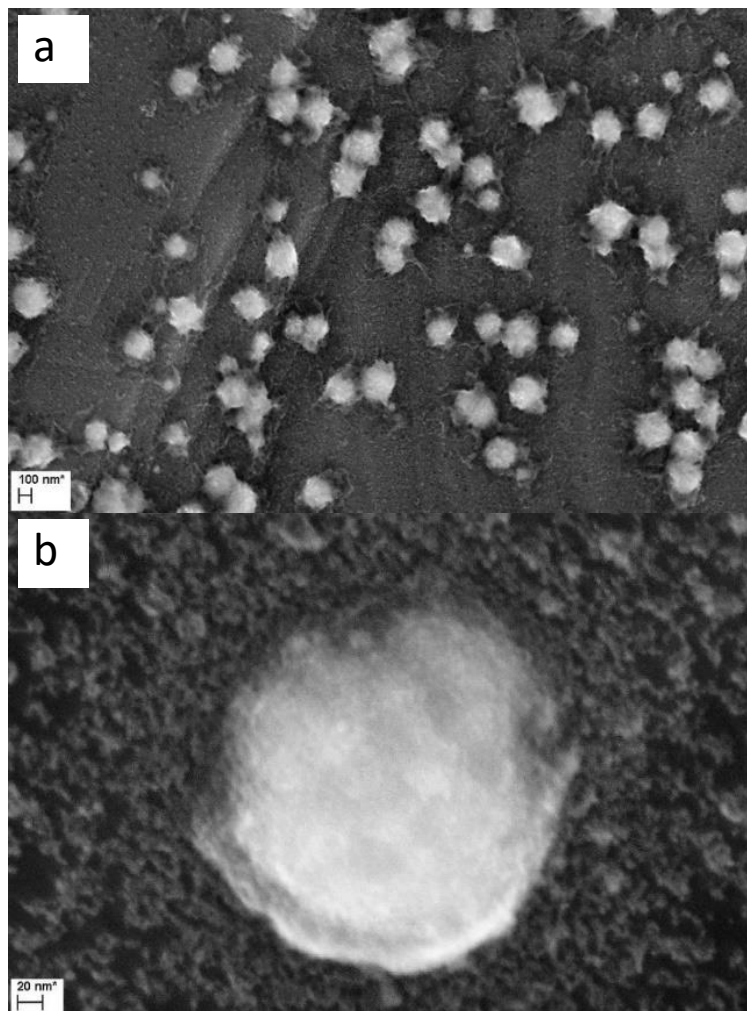


**Fig. 7.** SEM images of CeO<sub>2</sub>-Pt-Fecralloy samples. Deposits were formed onto foam cylinders with 2.3 cm<sup>3</sup> volume. Pt was deposited from 0.002 M H<sub>2</sub>PtCl<sub>6</sub> with E<sub>1</sub> = -0.7 V and 800 pulses. CeO<sub>2</sub> was deposited in 0.100 M Ce(NO<sub>3</sub>)<sub>3</sub> at -1.2 V with 13 C cm<sup>-3</sup> deposition charge.

#### 2.2.4 Pt loading and Pt surface area in Pt-Fecralloy and CeO<sub>2</sub>-Pt-Fecralloy catalysts

Table 1 summarizes data on Pt loading, Pt surface area per unit foam volume ( $S_{v,EC}$ ) and Pt surface area per unit Pt mass ( $S_{w,EC}$ ) of Pt-Fecralloy and CeO<sub>2</sub>-Pt-Fecralloy samples. The Pt loading values of catalysts were determined by ICP-MS, after exhaustive dissolution of Pt-Fecralloy and CeO<sub>2</sub>-Pt-Fecralloy samples. The Pt loadings were well-below those of catalysts described in [1], and remained unchanged after CeO<sub>2</sub> deposition, within the experimental error.

**Table 1.** Pt loading and Pt surface area of Pt-Fecralloy and CeO<sub>2</sub>-Pt-Fecralloy catalysts. Pt was deposited from a 0.002 M H<sub>2</sub>PtCl<sub>6</sub> solution. CeO<sub>2</sub> was deposited from a 0.100 M Ce(NO<sub>3</sub>)<sub>3</sub> solution.

System	Pt Loading / mg cm <sup>-3</sup>	CeO <sub>2</sub> deposition charge / C cm <sup>-3</sup>	S <sub>v,EC</sub> <sup>a</sup> / cm <sup>-1</sup>	S <sub>w,EC</sub> <sup>b</sup> / m <sup>2</sup> g <sup>-1</sup>
Pt-Fecralloy	0.373	0	62	16.6
CeO <sub>2</sub> -Pt-Fecralloy	0.370	7.1	45	12.1
CeO <sub>2</sub> -Pt-Fecralloy	0.370	14.2	15	4.0

a) Pt surface area per unit foam volume, determined by cyclic voltammetry

b) Pt surface area per unit Pt mass, determined by cyclic voltammetry

The Pt surface area was calculated from the H desorption charge, measured in cyclic voltammetry, as in previous work [1], according to a well-established method [68]. Fig. 8 shows voltammograms recorded with a Pt-Fecralloy and two CeO<sub>2</sub>-Pt-Fecralloy samples that differed for their CeO<sub>2</sub> deposition charge. Increasing amounts of CeO<sub>2</sub> progressively depressed the hydrogen adsorption/desorption, but did not entirely prevent those processes. This means that a significant part of the Pt surface remained accessible to electrolyte and, one could speculate, available to catalyse gas-phase reactions. The inset in Fig. 8 shows that the residual Pt surface area was ca. 25% of the initial one for a 14.2 C cm<sup>-3</sup> CeO<sub>2</sub> deposition charge, close to that used in the preparation of the catalysts described in the following section 3.2.

A calculation of the Pt surface area per unit mass for spherical particles with 200 nm diameters (compatible with images in Fig. 7) according to the formula  $a_{Pt} = 6/\rho_{Pt}d$ , where  $\rho_{Pt}$  is Pt density and  $d$  the particles diameter, would yield 1.43 m<sup>2</sup> g<sup>-1</sup>. The experimental value was ca. 12 times higher, this large discrepancy was caused by the assumption that nanoparticles were perfect spheres, with smooth surfaces, whereas they rather appeared to be aggregates of smaller entities, as also observed by other authors [69]. Thus, their surface area per unit Pt mass was as large as that of much smaller, perfectly spherical nanoparticles.

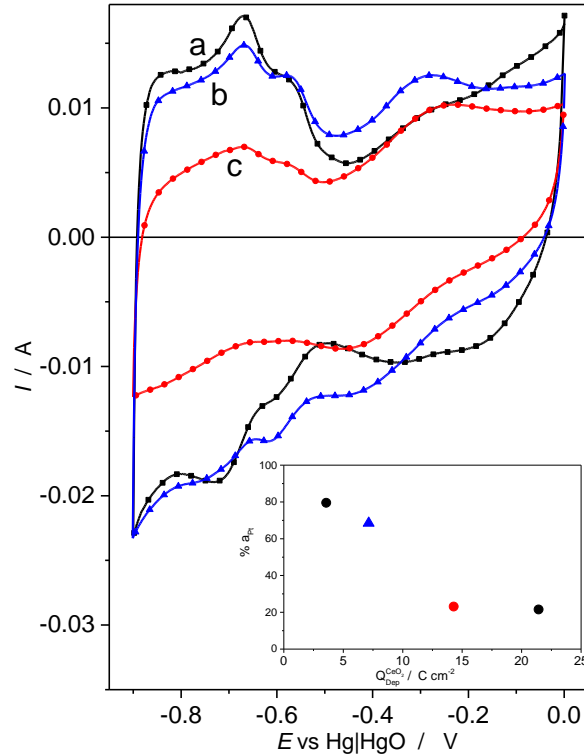


**Fig. 8.** Cyclic voltammograms recorded in 1.0 M KOH solution with Pt-Fecralloy (a) and CeO<sub>2</sub>-Pt-Fecralloy (b,c) samples. CeO<sub>2</sub> Deposition charge: 7.1 (b) or 14.2 C cm<sup>-3</sup> (c). Scan rate 50 mV s<sup>-1</sup>.

For CO oxidation test, the preparation approach was the same described above for samples used for methanol oxidation, but for this application we tried to obtain another set of samples with lower loading and smaller nanoparticles. We slightly changed experimental conditions of platinum nanoparticles electrodeposition on Fecralloy support. Electrolyses carried out in 0.002 M solution, with  $E_1 = -0.7$  V and 800 pulses yielded catalysts with  $370 \pm 30 \mu\text{g cm}^{-3}$  Pt loading, determined by ICP-MS, like previously described. On the other hand, electrolyses were carried out in 0.015 M solution, with  $E_1 = -1.2$  V and 200 pulses in order to obtain catalysts with a lower Pt loading ( $12 \pm 1 \mu\text{g cm}^{-3}$ ) and smaller particle dimensions. Thus, the total Pt content of each structured catalyst cylinder was either 850 or 28  $\mu\text{g}$ , respectively. Catalysts with both Pt loadings were further modified by deposition of CeO<sub>2</sub>. The data in Table 2 show that the deposition of increasing amounts of CeO<sub>2</sub> progressively depressed the exposed surface of Pt measured by voltammetry, thus confirming the formation of thicker and more compact oxide shells on metal nanoparticles: as an example, CeO<sub>2</sub><sup>16.2</sup>-Pt<sub>370</sub> foam catalyst retained only 9% of the exposed metal area displayed by Pt<sub>370</sub>. Nevertheless, even for the highest CeO<sub>2</sub> deposition charge, the oxide shells retained their porosity. Henceforth, the structured catalysts will be labelled as Pt<sub>yy</sub> or CeO<sub>2</sub><sup>xx</sup>-Pt<sub>yy</sub>, where the subscript yy and the superscript xx represent respectively the Pt loading, in  $\mu\text{g cm}^{-3}$ , and the CeO<sub>2</sub> loading, indirectly defined through the charge transferred during the oxide deposition, in C cm<sup>-3</sup>. Table 2 summarizes the catalysts that were investigated toward CO oxidation.

**Table 2.** Pt loading ( $L_{Pt}$ ),  $CeO_2$  deposition charge, specific Pt surface area by cyclic voltammetry (CV) measurements, corresponding average dimension of Pt nanoparticles (by SEM observation or CV), and apparent activation energy for CO oxidation for Pt-Fecralloy and  $CeO_2$ -Pt-Fecralloy catalysts.

Catalyst	$L_{Pt}$ $\mu g\ cm^{-3}$	$CeO_2$ Dep. Charge $C\ cm^{-3}$	$S_{Pt}$ CV $m^2\ g^{-1}$	$d_{Pt}$ SEM nm	$d_{Pt}$ CV nm	$E_{app}$ kJ/mol
Pt <sub>370</sub>	370	-	16.6	100 - 200	17	121
$CeO_2^{4.5}$ -Pt <sub>370</sub>	370	4.5	13.8	100 - 200		118
$CeO_2^{12.5}$ -Pt <sub>370</sub>	370	12.5	5.3	100 - 200		118
$CeO_2^{14.2}$ -Pt <sub>370</sub>	370	14.2	4	100 - 200		116
$CeO_2^{16.7}$ -Pt <sub>370</sub>	370	16.7	1.5	100 - 200		122
Pt <sub>12</sub>	12	-	75	25 - 50	3.8	127
$CeO_2^{6.5}$ -Pt <sub>12</sub>	12	6.5	32	25 - 50		125

Figure 9 shows SEM images of Pt-Fecralloy and  $CeO_2$ -Pt-Fecralloy catalysts. The typical size of the Pt nanoparticles fell in the range 100-200 nm and 25-50 nm for the catalysts with higher and lower Pt loadings, respectively. An increase in the thickness of the  $CeO_2$  layer with increasing deposition charge was visible (Fig.9 a-c). However, the resolution of the images was not high enough to allow an accurate determination of the shell thickness.

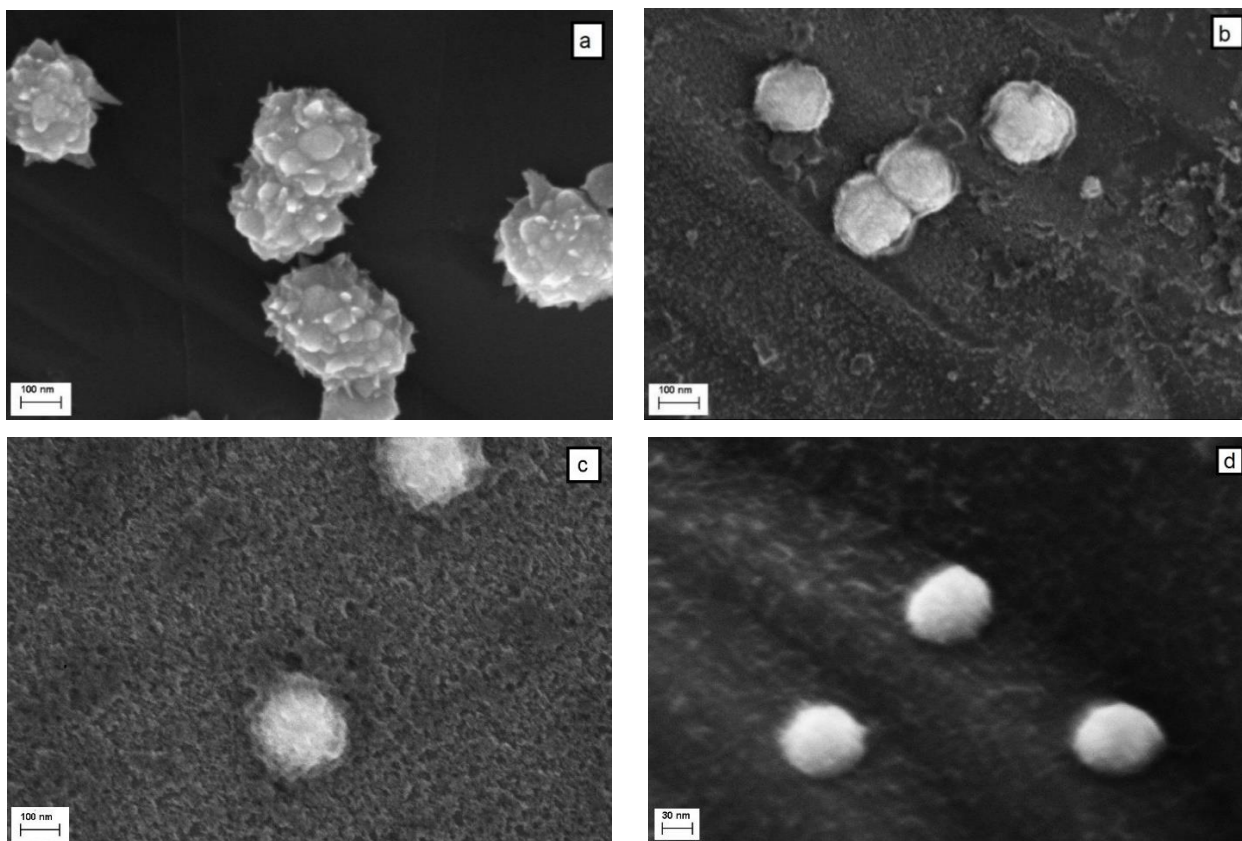


**Fig.9.** SEM images of as-prepared catalysts. a) Pt<sub>370</sub>-Fecralloy; b)  $CeO_2^{4.2}$ -Pt<sub>370</sub>-Fecralloy; c)  $CeO_2^{13.1}$ -Pt<sub>370</sub>-Fecralloy; d)  $CeO_2^{6.5}$ -Pt<sub>12</sub>-Fecralloy.

### 2.3. Catalytic combustion of methanol on Pt-Fecralloy, CeO<sub>2</sub>-Fecralloy and CeO<sub>2</sub>-Pt-Fecralloy

Figure 9 presents the results of the lean methanol combustion tests with foam catalysts in terms of the yield to CO<sub>2</sub> as a function of the reaction temperature. Preliminary tests were run with a bare Fecralloy foam and indicated that, under the investigated experimental conditions, the oxidation of methanol started above 375 °C with the initial production of CO, followed by the formation of CO<sub>2</sub> only above ca 430 °C. Temperatures above 650 °C were required to reach complete methanol conversion leading to the formation of comparable amounts of CO and CO<sub>2</sub>, with a probable significant contribution coming from homogeneous reactions [62].

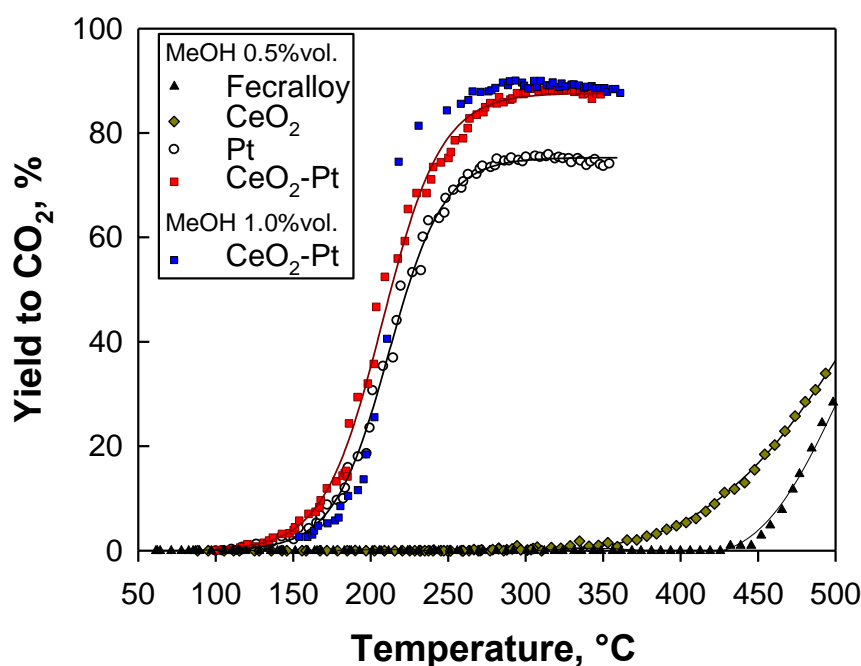


**Fig. 9.** Methanol yield to CO<sub>2</sub> as a function of the reaction temperature over Pt-Fecralloy, CeO<sub>2</sub>-Pt-Fecralloy, CeO<sub>2</sub>-Fecralloy catalysts and a bare Fecralloy foam. Feed conditions: 40 Sdm<sup>3</sup> h<sup>-1</sup>, CH<sub>3</sub>OH 0.5 - 1.0 % in air.

The deposition of CeO<sub>2</sub> on the Fecralloy foam induced a limited improvement in the overall methanol oxidation activity of the system, showing some CO<sub>2</sub> formation from ca. 350 °C (Fig. 9), always accompanied by the production of comparable amounts of CO (not shown). At temperatures above 550 °C, the CO<sub>2</sub> yield over CeO<sub>2</sub>-Fecralloy became comparable to that on bare Fecralloy foam, thus confirming a predominant role of homogeneous oxidation reactions above such threshold temperature.

In contrast, the Pt-based catalysts displayed a significant activity for methanol total oxidation, despite their rather low noble metal content. As shown in Figure 9, CO<sub>2</sub> formation became measurable starting from slightly above 100 °C and its yield increased rather steeply along with the reaction temperature, and eventually reached an asymptotic value above 250 °C. This corresponded to the presence of some unconverted methanol in the exhaust gas leaving the catalyst, whereas no other products were detected.

According to the results in Figure 9, any significant contributions either from the homogeneous gas phase reaction or from surface reactions on CeO<sub>2</sub>-Fecralloy can be safely excluded up to 350 °C.

CeO<sub>2</sub>-Pt-Fecralloy catalyst outperformed its Pt-Fecralloy counterpart with identical noble metal loading, both in terms of catalytic activity before light-off (with a measured difference of ca 10 °C in T<sub>10</sub>, defined as the temperature required for 10 % yield to CO<sub>2</sub>, Table 3), as well as in the final CO<sub>2</sub> yield at high temperatures (87.7 % vs. 75.3 %). Moreover, CO formation was never detected in the exhaust gas from the CeO<sub>2</sub>-Pt-Fecralloy sample, and remained below 20 ppmv with Pt-Fecralloy system, in good agreement with our previous results on similar foam catalysts with higher Pt-loadings [1]. Reactivity measurements were repeated after having exposed the catalysts to reaction conditions at 600°C (2h), and gave substantially identical results (not shown), indicating a good stability of the catalytic activity of Pt-based foams under those experimental conditions.

**Table 3.** Catalytic activity of foam catalysts for methanol combustion.

System	Pt Loading / mg cm <sup>-3</sup>	S <sub>w,EC</sub> / m <sup>2</sup> g <sup>-1</sup>	T <sub>10</sub> <sup>a</sup> / °C	E <sub>a</sub> <sup>b</sup> / kJ mol <sup>-1</sup>	R <sub>v</sub> CO <sub>2</sub> <sup>c</sup> / mmol cm <sup>-3</sup> h <sup>-1</sup>	R <sub>w</sub> CO <sub>2</sub> <sup>c</sup> / mmol g <sub>Pt</sub> <sup>-1</sup> h <sup>-1</sup>	S <sub>v</sub> <sup>d</sup> / cm <sup>-1</sup>	S <sub>w</sub> <sup>d</sup> / m <sup>2</sup> g <sup>-1</sup>
Fecralloy	-	-	470	310		-		
CeO <sub>2</sub> -Fecralloy	-	-	428	88.5		-		
Pt-Fecralloy	0.37	16.6	179	70.4	0.11	296	0.46	0.12
CeO <sub>2</sub> -Pt-Fecralloy	0.37	5.0	169	70.4	0.15	415	0.69	0.19
Pt-Fecralloy <sup>e</sup>	5 - 13	12 - 13	113-133	69.0	0.49 - 2.54	100 - 300	-	-

a) Temperature for 10 % yield to CO<sub>2</sub>; 0.5% MeOH in air, GHSV=16500 h<sup>-1</sup>.

b) Apparent activation energy.

c) R<sub>v</sub>, R<sub>w</sub> are the specific CO<sub>2</sub> formation rates at 150° per unit volume of foam and per gram of Pt, respectively.

d) S<sub>v</sub> and S<sub>w</sub> are the Pt surface areas per unit volume of foam and per gram of Pt, respectively, estimated (after calcination for 2h in air at 600°C) from asymptotic conversion data at 350°C.

e) Catalysts prepared by electrodeposition starting from same batch of Fecralloy foam [1].

As shown in Figure 9 for the case of CeO<sub>2</sub>-Pt-Fecralloy, when the inlet concentration of methanol was increased, the CO<sub>2</sub> yield plots shifted slightly towards higher temperatures, indicating a less than linear dependency of the catalytic combustion rate on fuel concentration at low temperature. Analogous results were also found over the Pt-Fecralloy catalyst.

Figure 10 presents the Arrhenius plots for the specific CO<sub>2</sub> formation rate calculated by eq. (2) for the foam catalysts. Data sets obtained with CeO<sub>2</sub>-Pt-Fecralloy in the low temperature region (under kinetic control) at various inlet methanol concentrations merged into a single line within experimental accuracy, and departed from it above the light-off temperature. The same occurred for the Pt-Fecralloy foams, confirming our previous results [1]. The apparent activation energy was estimated from the slope of the corresponding lines equal to ca 70 kJ mol<sup>-1</sup>, and it was hardly affected by the addition of CeO<sub>2</sub> as a promoter for Pt or by the noble metal content (Table 3). Indeed, this value agrees well with 68 - 70 kJ mol<sup>-1</sup> obtained by us onto Pt-Fecralloy foams with various (higher) metal loadings, and it also compares to the activation energy previously reported in the literature for methanol oxidation on Pt without any support (59-64 kJ mol<sup>-1</sup>) [70]. The apparent zero order dependency of the CO<sub>2</sub> formation rate on methanol concentration, and the rather repeatable estimates for the apparent activation energy suggest that Pt active sites might be saturated at low temperature (and, therefore, poisoned) by an intermediate reaction product (such as in the case of CO) strongly adsorbed on their surface [1,64,71,72,73]. Methanol combustion mechanism on Pt-Fecralloy was qualitatively insensitive to the addition of CeO<sub>2</sub>, although ceria is generally recognized as an effective promoter for noble metal based oxidation catalysts due to its large availability of labile lattice oxygen and its possible spillover from ceria to Pt [5,46].

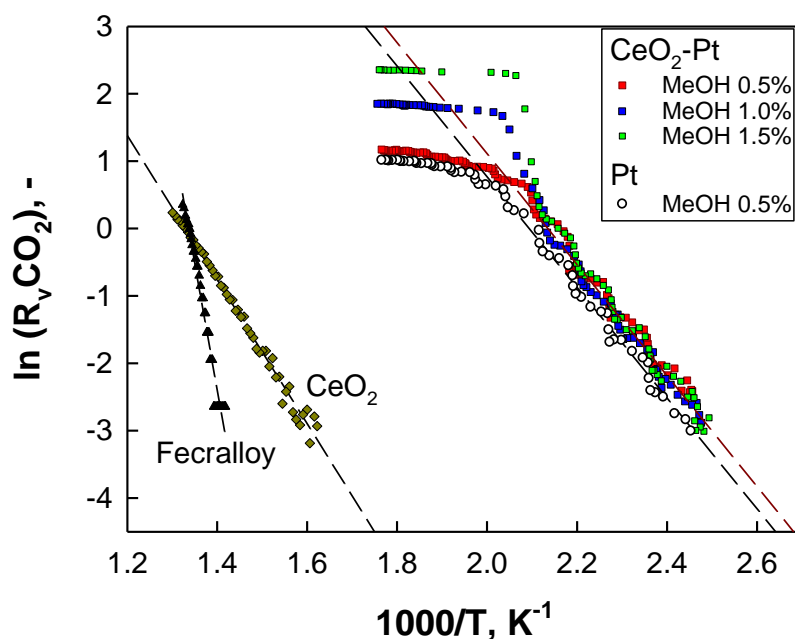


**Fig. 10.** Arrhenius plots for the specific CO<sub>2</sub> production rate per unit volume during methanol combustion over Pt-Fecralloy, CeO<sub>2</sub>-Pt-Fecralloy, CeO<sub>2</sub>-Fecralloy catalysts and a bare Fecralloy foam. Feed conditions: 40 Sdm<sup>3</sup> h<sup>-1</sup>, CH<sub>3</sub>OH 0.5 - 1.5 % in air.

Nevertheless, CeO<sub>2</sub> addition on Pt-Fecralloy catalyst increased the methanol combustion rate ( $R_v$ ) at 150°C by a factor as large as 1.4 (Table 3), due to the formation of some additional active sites most probably located at the interface between the two materials. Moreover, the combustion rate per gram of Pt ( $R_w$ ) increased accordingly, showing an enhanced utilization factor of the costly noble metal also with respect to our previous results with Pt-Fecralloy foams (Table 3).

The asymptotic behaviour of methanol conversion (which is equal to the CO<sub>2</sub> yield) upon light-off suggests the onset of full external mass-transfer control. Indeed, the asymptotic methanol conversion (CO<sub>2</sub> yield) level attained with each foam catalyst was independent of methanol feed concentration (0.5 vs 1.0 % vol. Figure 10). On the other hand, methanol conversion increased to almost 100 % (not shown) when the tests were repeated doubling the contact time at fixed gas velocity, i.e. using two identical catalytic foams in series. All those results point to the onset of a diffusion-controlled regime associated with pseudo-first-order kinetics [74]. Under the assumption of isothermal plug flow behaviour and irreversible reaction, the steady-state mass balance for methanol in the reactor becomes:

$$-\ln(1 - x) = \frac{S_v V_{foam} k_m}{Q} \quad (4)$$

where  $x$  represents methanol conversion,  $S_v$  is the specific area of the active sites per unit volume of the foam [cm<sup>2</sup> cm<sup>-3</sup>],  $V_{foam}$  is the foam volume [cm<sup>3</sup>],  $k_m$  is the mass transfer coefficient [cm h<sup>-1</sup>], and  $Q$  is the volumetric flow [cm<sup>3</sup> h<sup>-1</sup>].

The value of  $k_m$  was estimated equal to 30 cm/s at 350 °C under our experimental conditions with the correlation given by Giani et al. [74], by considering that the approximate diameters of struts ( $d_s$ ) and pores ( $d_p$ ) in the Fecralloy foams were respectively  $1.0 \times 10^{-2}$  cm and  $5.5 \times 10^{-2}$  cm, and the geometric void fraction was 92.2%. Assuming that  $k_m$  was not affected by the addition of the thin CeO<sub>2</sub> overlayer on Pt particles, it was possible to calculate for both catalysts the specific area  $S_v$  of those Pt sites that were active after light-off (Table 3). Noteworthy, CeO<sub>2</sub> addition increased the surface area of active sites by as much as 50%, in good agreement with the already reported activity increase before light-off.

Since CeO<sub>2</sub> was added at the final step of preparation after Pt-deposition so that neither metal loading nor its morphology were significantly affected, it can be argued that the increase in the number of available catalytic active sites in CeO<sub>2</sub>-Pt-Fecralloy was associated to the formation of novel CeO<sub>2</sub>- Pt interface sites that were easily accessible in the nanoparticles with a quasi-core-shell configuration.

Comparing the values of the specific surface area of active Pt sites per gram of metal to the corresponding figures estimated by voltammetric experiments, i.e. comparing  $S_w$  with  $S_{w,EC}$  (Table 3), it is evident that the active sites for methanol catalytic combustion at 350°C were only a small fraction of the total exposed Pt surface, respectively 0.7% and 3.8% for Pt-Fecralloy and CeO<sub>2</sub>-Pt-Fecralloy foams.

In a recent work [72] it was convincingly shown that the active sites for CO oxidation in Pt/CeO<sub>2</sub> catalysts were those atoms located along the perimeter of the boundary (and mostly those located at the corners due to their lower coordination number), rather than all of the Pt exposed atoms. The fundamental role of perimeter and corner Pt atoms is also corroborated by the lack of direct correlation previously reported between methanol combustion rates on Pt-Fecralloy foam catalysts with variable metal loadings and their corresponding total exposed noble metal surface area [1].

In analogy to our results on methanol combustion, Cargnello et al. [72] also observed an apparent activation energy of ca. 65 kJ/mol on their Pt/CeO<sub>2</sub> nanoparticles and a zero-order rate in CO, as a consequence of reaction between CO adsorbed on the noble metal and O<sub>2</sub> provided by CeO<sub>2</sub>, so that the CO on the metal was unable to suppress the rate of O<sub>2</sub> adsorption. A similar synergic role of the Fecralloy support in the catalytic oxidation process was inferred also in the case of CO oxidation over analogous Pd-Fecralloy catalysts [28], possibly through the activation of oxygen molecules on specific sites (such as FeO<sub>x</sub> [75]) on the Fecralloy surface. Therefore, it appears that Pt active sites existed either at the Pt-Fecralloy and CeO<sub>2</sub>-Pt interfaces and they behaved in a similar manner (identical activation energy and apparent reaction order), despite the different nature of the materials.

#### 2.4. CO oxidation activity

Figure 11a presents the results of catalytic oxidation tests carried out with an inlet feed of 0.5% vol. CO and 10% vol. O<sub>2</sub> over CeO<sub>2</sub><sup>xx</sup>-Pt<sub>370</sub> catalysts having variable amounts of CeO<sub>2</sub>, but an equal 370 μg cm<sup>-3</sup> Pt loading. Light-off plots for the unpromoted Pt<sub>370</sub>-Fecralloy foam catalyst and for a CeO<sub>2</sub><sup>13</sup>-Fecralloy foam sample without any Pt are also shown for comparison. All the Pt containing catalysts displayed sharp conversion-temperature curves, characterized by an initially slow increase of CO conversion at low temperature followed by a sudden jump up to 100% (attained during a rather short transient phase with a rapid increase in the temperature of the catalyst and the development of temperature gradients along the axial coordinate of the foam). Although similar to other light-off curves, the one recorded with the CeO<sub>2</sub><sup>4.2</sup>-Pt<sub>370</sub> catalyst, with the lowest ceria content, showed a more complicated pattern, with an ignition phase extending over a larger range of temperature and at least two marked steps, which can be possibly ascribed to two populations of catalytic sites with different activity toward CO oxidation.

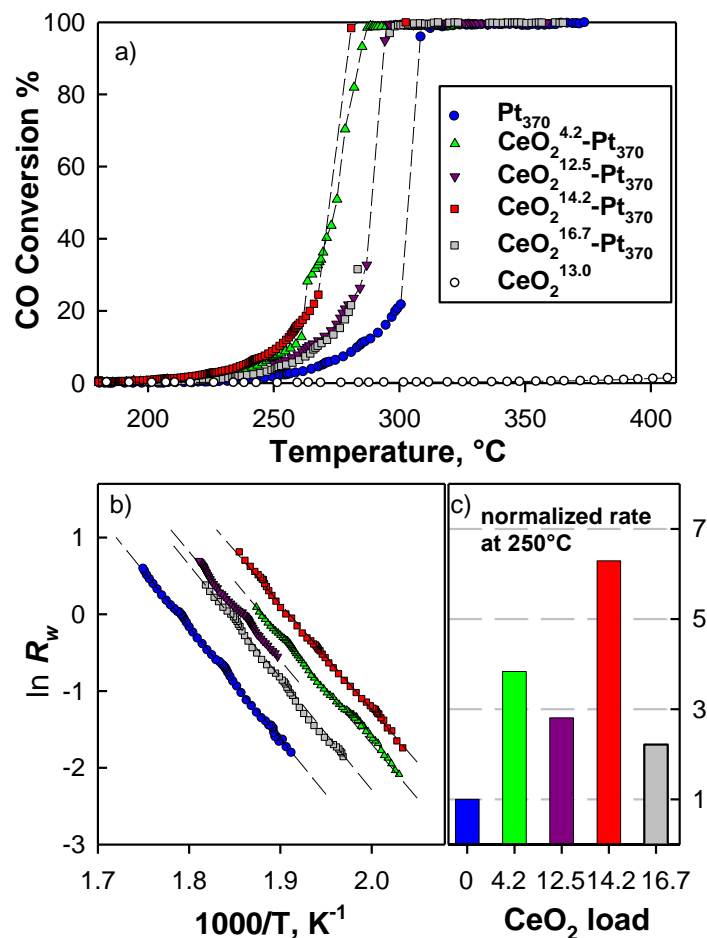


**Fig.11.** a) CO conversion as a function of the reaction temperature and b) corresponding Arrhenius plots for the CO oxidation rate over Pt<sub>370</sub>-Fecralloy and CeO<sub>2</sub><sup>xx</sup>-Pt<sub>370</sub>-Fecralloy foam catalysts with fixed Pt and variable CeO<sub>2</sub> loadings; c) CO oxidation reaction rates, referred to Pt mass, on CeO<sub>2</sub><sup>xx</sup>-Pt<sub>370</sub>-Fecralloy catalysts at 250 °C, normalized with respect to the unpromoted Pt<sub>370</sub>-Fecralloy sample. Feed conditions CO=0.5% O<sub>2</sub>= 10% vol.

It clearly appears from Figure 11 that the deposition of a CeO<sub>2</sub> over-layer onto the Pt nanoparticles induced a marked increase in the catalytic oxidation activity, as shown by the shift of the CO conversion plots towards lower temperature with respect to the unpromoted Pt<sub>370</sub> counterpart. In particular, the temperature required for 10% CO conversion decreased by as much as 35 °C passing from Pt<sub>370</sub> foam to the most active CeO<sub>2</sub><sup>14.2</sup>-Pt<sub>370</sub> system. Inspection of the light-off curve relevant to CeO<sub>2</sub>-Fecralloy sample allows to exclude that the enhancement in activity derived from a mere contribution of CO oxidation occurring on additional CeO<sub>2</sub> active sites. Indeed, CO oxidation on this sample was detected only above 350 °C (a temperature at which CO conversion was already 100% even on the least active unpromoted Pt<sub>370</sub> foam catalyst), and 5% conversion was only attained at 510 °C.

Low conversion data acquired under differential and pseudo isothermal conditions were used to estimate values of the apparent activation energy from the slopes of the corresponding Arrhenius plots reported in Figure 11b. In the temperature range 200 – 300 °C, the activation energy for CO oxidation on Pt<sub>370</sub> foam

catalyst was equal to  $121 \pm 5$  kJ/mol, in good agreement with literature data on Pt single crystals, Pt wires or high surface area supported catalysts [35-37] and close to the binding energy of adsorbed CO [38]. Remarkably, the observed activation energies for all  $\text{CeO}_2^{\text{xx}}\text{-Pt}_{370}$  catalysts (Table 2) were not affected by the presence of  $\text{CeO}_2$  nor by its loading and remained substantially equal to the value recorded for the unpromoted  $\text{Pt}_{370}$  system, in the same temperature range.

Further temperature programmed oxidation tests were run on the best performing  $\text{CeO}_2^{14.2}\text{-Pt}_{370}$  system, using different inlet concentrations of CO and  $\text{O}_2$ . The results (Figure 12) clearly indicated that the reaction rate was negative first order with respect to CO and positive with roughly 0.85 order with respect to  $\text{O}_2$ , in excellent agreement with previously reported data at similar temperatures [35,39]. The apparent activation energy for all the feed conditions explored was highly repeatable showing an average value of  $116 \pm 4$  kJ/mol. The CO oxidation rate was not affected by the presence of  $\text{CO}_2$  (5% vol.) or humidity in the feed stream.

The negative first-order kinetics, typical for CO oxidation on platinum group metals, is caused by the strong binding of CO to the metal surface, which inhibits further reaction. In general, the reaction proceeds through a Langmuir-Hinshelwood mechanism involving adsorbed CO and O atoms. Under reaction conditions typically used in most high-pressure supported catalyst studies, and most low-pressure (UHV) studies on model catalysts, the surface is almost entirely covered by CO, which acts as a poisons so that the reaction rate is determined by the rate of its desorption [76-78]. Indeed, oxygen can only adsorb at sites where CO has desorbed, leading to first-order dependence in oxygen partial pressure, negative-first-order dependence in CO partial pressure, and zero-order total pressure dependence [76]. When CO is removed from the surface, the catalyst 'lights-off' with a rate that increases quickly with increasing reaction temperature. The exothermic reaction makes the process autocatalytic, allowing 100% conversion to be achieved rapidly [27,28,76].

Therefore, it appears that CO oxidation mechanism on  $\text{Pt}_{370}$ -Fecralloy catalysts was insensitive to the addition of  $\text{CeO}_2$ , in the temperature range explored in this work. Nevertheless, the specific reaction rate per gram of Pt increased significantly, by a factor comprised between 2 and 7, due to the deposition of the ceria overlayer on Pt nanoparticles (Figure 12c). Since  $\text{CeO}_2$  was deposited as an outer shell over preformed Pt nanoparticles firmly anchored onto the Fecralloy foam, the overall noble metal loading and the initial nanoparticle morphology were preserved. Therefore, the rate increase should be a consequence of an increase in the number of available catalytic active sites. This effect can be associated to the formation of novel sites at the  $\text{CeO}_2\text{-Pt}$  interface [18], which are less prone to be "poisoned" by strongly adsorbed CO molecules. Accordingly, Zhang et al. [6] reported a higher CO oxidation activity for  $\text{Pt@CeO}_2$  core-shell catalysts compared to conventional  $\text{Pt/CeO}_2$  prepared by co-precipitation, which was attributed to the increased extension of the interface between the metal nanoparticles and transition metal oxide. In analogy to our result, Lee et al. [8] found a maximum in the methane oxidation activity of their  $\text{Pt@CeO}_2$  core-shell

nanoparticles for a shell thickness between 14 nm and 20 nm, whereas thinner CeO<sub>2</sub> layers were less effective to contrast Pt sintering during catalyst annealing.

Table 2 shows that, in contrast to the reaction rate, the values of the Pt surface area per unit mass progressively decreased for increasing contents of CeO<sub>2</sub> oxide. This highlights a lack of correlation between the CO oxidation rate and the total exposed noble metal surface area, which was already observed for methanol combustion onto same Pt-Fecralloy and CeO<sub>2</sub>-Pt-Fecralloy catalysts, and was also reported for the case of CH<sub>4</sub> combustion on Pd@CeO<sub>2</sub> and Pt@CeO<sub>2</sub> core-shell nanoparticles [8,9].

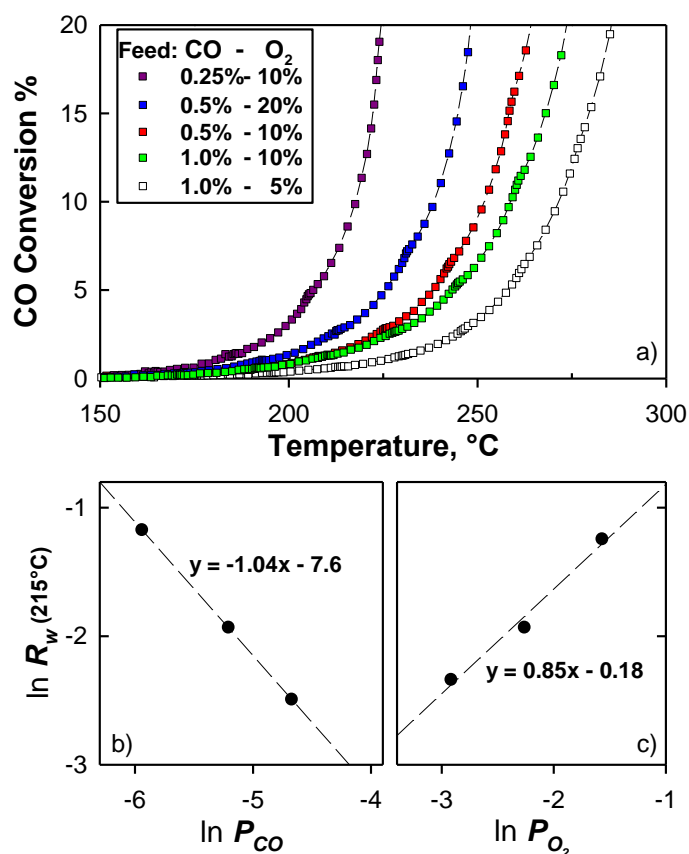


**Fig.12.** a) CO conversion as a function of temperature over CeO<sub>2</sub><sup>14.2</sup>-Pt<sub>370</sub>-Fecralloy foam catalyst for various inlet concentrations of CO and O<sub>2</sub>; b, c) effect of the partial pressure of CO and O<sub>2</sub> on the catalytic oxidation rate at fixed temperature (215 °C).

In order to check this result, we also measured the specific CO oxidation rate of two additional foam catalysts with a very low loading of Pt (12 μg cm<sup>-3</sup>) and nanoparticle size in the range 25-50 nm (Pt<sub>12</sub>-Fecralloy and CeO<sub>2</sub><sup>6.5</sup>-Pt<sub>12</sub>-Fecralloy). As expected from geometrical considerations, for the unpromoted catalysts the measured Pt surface area per unit mass scaled with the inverse of the average diameter (Table 2). On the other hand, the CO oxidation rate per gram of Pt increased by as much as a factor 11 (Figure 13c), while the observed activation energy of the reaction remained the same (Table 2). This suggests that Pt sites along the perimeter of the Pt-Fecralloy boundary were the main responsible for CO oxidation before light-off, because

the observed variation in the reaction rate was consistent with the increase in their total number, which scales with  $d_{Pt}^{-2}$  [18], rather than on the metal surface area (scaling with  $d_{Pt}^{-1}$ ). Notably, also in the case of Pt nanoparticles supported onto  $CeO_2$ , it was demonstrated that the active sites for CO oxidation at low temperature were those Pt atoms located along the perimeter of the Pt- $CeO_2$  boundary, rather than all exposed atoms, for their lower coordination number [18].

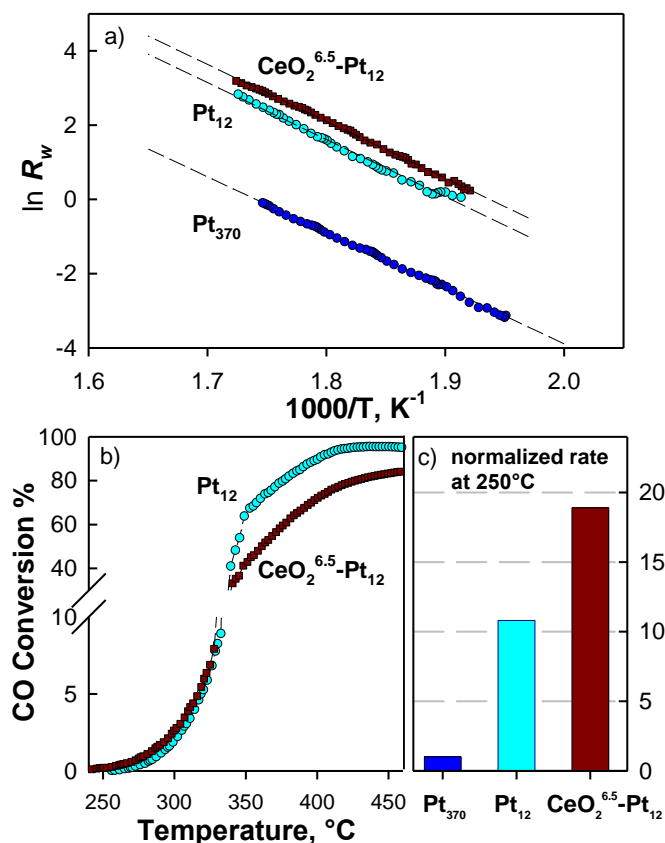


**Fig. 13.** a) Arrhenius plots for the specific CO oxidation rate per gram of Pt over  $Pt_{370}$ -Fecralloy,  $Pt_{12}$ -Fecralloy and  $CeO_2^{6.5}$ - $Pt_{12}$ -Fecralloy catalysts; b) Light-off plots for CO oxidation over  $Pt_{12}$ -Fecralloy and  $CeO_2^{6.5}$ - $Pt_{12}$ -Fecralloy catalysts; c) normalized catalytic reaction rate over the same catalysts at fixed temperature of 250 °C. Feed conditions  $CO=1\%$   $O_2=10\%$  vol.

The results in Figure 13b allowed the determination of reliable, purely kinetic data at relatively high temperatures (up to ca. 250 – 300 °C depending on the type of catalyst and feed conditions). This is due to: i) low Pt loadings of the structured catalysts (28  $\mu g$ ); ii) absence of a thick porous catalytic washcoat layer excluding the occurrence of internal mass transfer limitations [78]; iii) very effective gas–solid mass transfer features of the Fecralloy open cell foams [74]. The deposition of a  $CeO_2$  over-layer enhanced the observed specific reaction rate by a factor close to 2 also in the case of Pt nanoparticles with diameters of 25-50 nm. Notably, the curves in Figure 13b relevant to  $Pt_{12}$  and  $CeO_2^{6.5}$ - $Pt_{12}$  catalysts cross each other. This behaviour may be explained by remarking that Pt superficial sites, which are poisoned by strongly adsorbed CO molecules up to the light-off point, can activate once CO gets desorbed at higher temperatures. Thereafter,

the observed reaction rate becomes proportional to the total exposed surface area of Pt, since the overall process is limited by the external mass transfer phenomena and the active phase is dispersed on the top of the Fecralloy foam without any thick porous washcoat [78]. In fact, under such conditions, the unpromoted Pt catalyst can outperform its counterpart with a  $\text{CeO}_2$  shell, due to its higher exposed metal surface area, as indeed observed for those  $\text{Pt}_{12}$  and  $\text{CeO}_2^{6.5}\text{-Pt}_{12}$  foams with very low Pt loadings. Obviously, this effect can be observed only if the CO conversion reaches a plateau level well below 100%, which generally requires operation at rather low contact times over noble metal catalysts [74].

## 2.5. Thermal stability

### 2.5.1. Characterization of used $\text{CeO}_2\text{-Pt}$ -Fecralloy catalysts

Fig. 14 compares SEM images of as-prepared  $\text{CeO}_2\text{-Pt}$ -Fecralloy catalysts with those, prepared under the same conditions, that were used as catalysts form methanol oxidation. The images show that there was no Pt particles loss, and that the shape and size of the particles remained unchanged. A change in the morphology of the  $\text{CeO}_2$  deposit on Fecralloy, presumably due to crystallization, was detected. These results agree with the observed stable catalytic activity of the samples when they were used in successive methanol combustion tests.

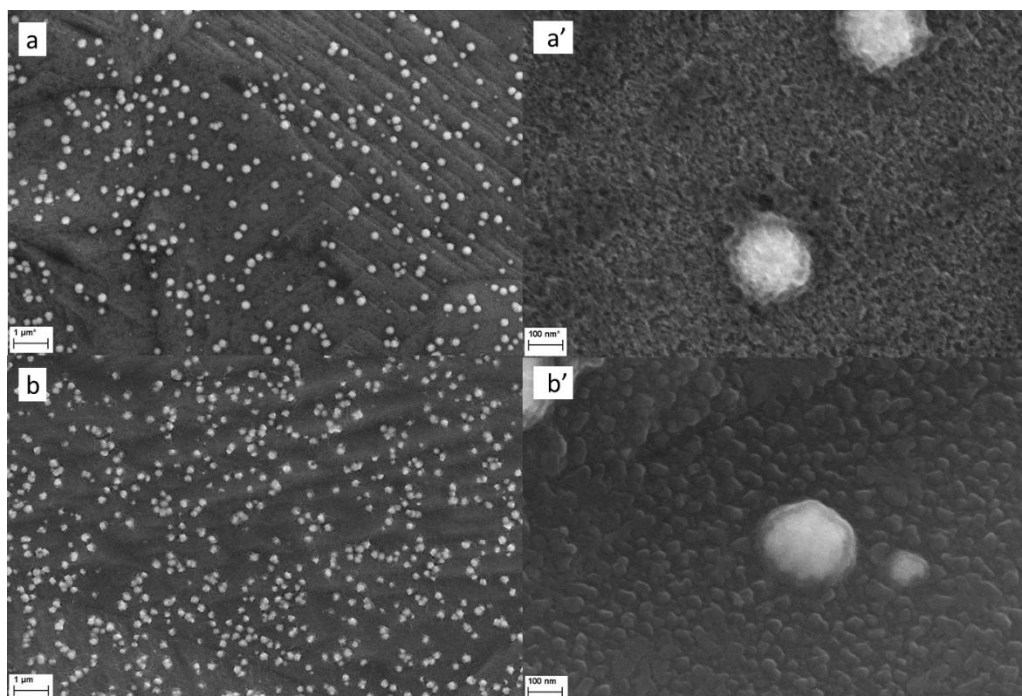


Fig.14. SEM images of  $\text{CeO}_2\text{-Pt}$ -Fecralloy catalysts taken before (a, a') and after use in methanol catalytic combustion (b, b'). Preparation conditions were the same as for Fig. 7.

To check the stability of the core-shell particles at high-temperature, we repeated temperature programmed oxidation tests on the best performing  $\text{CeO}_2^{14.2}\text{-Pt}_{370}$ -Fecralloy foam catalyst after exposing it at 800 °C in air for increasing times up to a total of 24h. Figure 15a shows that the temperature required to attain 10% CO conversion ( $T_{10}$ ) did not vary upon ageing the catalyst at 800 °C up to 24 h, indicating a remarkable stability of its intrinsic catalytic activity, which, in turn, confirmed the high sintering resistance of those core-shell nanoparticles [3, 5, 6, 8] also when they were directly anchored onto a structured Fecralloy foam reactor. On the contrary, the unpromoted  $\text{Pt}_{370}$ -Fecralloy catalyst showed an initial increase in activity after a calcination treatment at 800 °C for 12 h, testified by a corresponding decrease in the value of  $T_{10}$  by ca 20 °C (Figure 15a). Aging the catalyst for further 12 h at 800 °C induced a partial loss of activity, and an increase of  $T_{10}$  by ca.10 °C. Such results reveal a lower thermal stability of the unprotected Pt particles anchored onto the Fecralloy support, that are prone to extensive reconstruction, sintering and vaporization under oxidizing conditions at 800 °C [23, 24, and ref. therein].

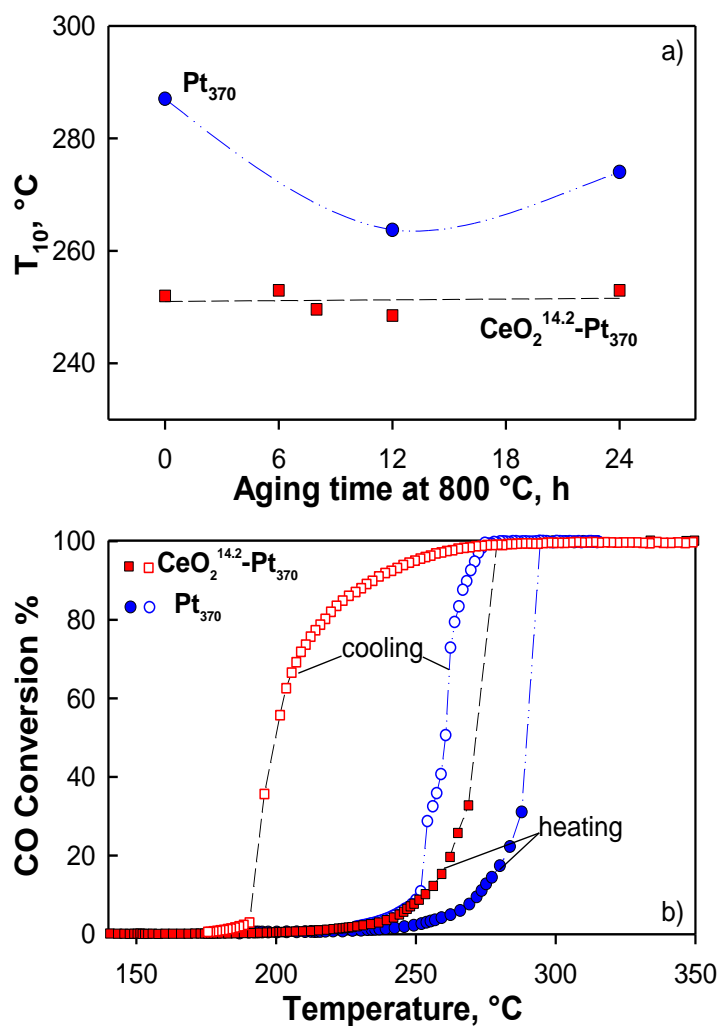


Fig.15. Effect of the progressive aging at 800 °C on the temperature required to achieve 10% CO conversion over  $\text{Pt}_{370}$ -Fecralloy and  $\text{CeO}_2^{14.2}\text{-Pt}_{370}$ -Fecralloy catalysts; b) Light-off and blow-out plots for CO oxidation over aged foam catalysts (24 h at 800 °C) recorded respectively during heating-up or cooling-down phases at 3 °C/min. Feed conditions  $\text{CO} = 0.5\%$   $\text{O}_2 = 10\%$  vol.

At the end of this rather demanding thermal cycling, catalysts were studied by SEM. Figure 16 compares images recorded with Pt<sub>370</sub>-Fecralloy and CeO<sub>2</sub><sup>14.2</sup>-Pt<sub>370</sub>-Fecralloy aged catalysts. Pt<sub>370</sub>-Fecralloy, Figure 16a, appears to have been significantly deteriorated. Not surprisingly [23,24], after prolonged exposure at 800 °C, the Pt particles were evidently reconstructed, with an overall decrease of surface area, and their number decreased, possibly due to the detachment of some of them from the substrate, apparently with some size selectivity, i.e. with preferential loss of larger particles. Instead, in CeO<sub>2</sub><sup>14.2</sup>-Pt<sub>370</sub>-Fecralloy, both the surface density and the typical size of Pt nanoparticles was maintained. For both catalysts, EDS analyses of the Fecralloy substrate showed a strong Al enrichment, in agreement with literature reporting the formation of Al<sub>2</sub>O<sub>3</sub> scales [79]. Pt loss might have been caused by poor adhesion between Pt and those scales. If so, the CeO<sub>2</sub> layer, besides providing a direct protective action on Pt nanoparticles, preventing their sintering, might have contributed to retain firm Pt-substrate adhesion.

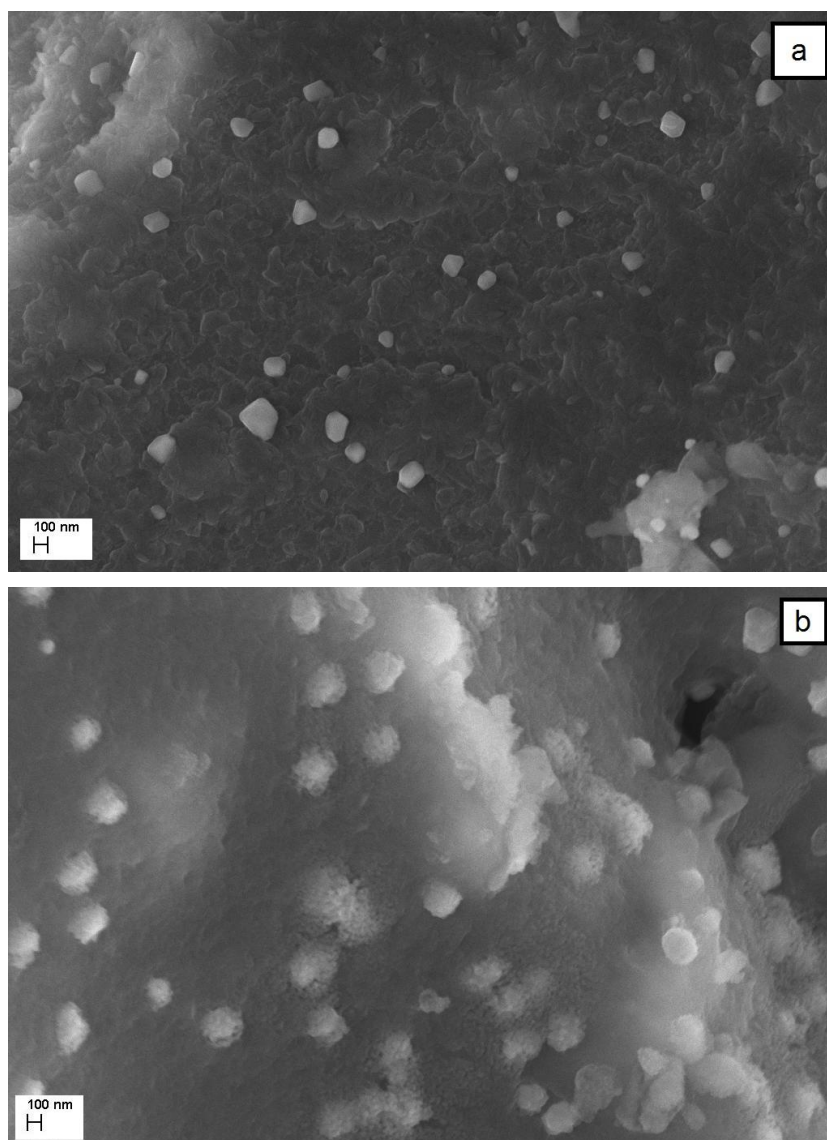


Fig.16. SEM images of aged catalysts. a: Pt<sub>370</sub>-Fecralloy; b: CeO<sub>2</sub><sup>13.1</sup>-Pt<sub>370</sub>-Fecralloy.

CO conversion data retrieved during a cooling temperature ramp (at 3 °C min<sup>-1</sup>) starting from 100% at 400 °C revealed the occurrence of a typical hysteresis loop between light-off (ignition) and blow-out (extinction) branches over both unpromoted Pt<sub>370</sub>-Fecralloy and CeO<sub>2</sub><sup>14.2</sup>Pt<sub>370</sub>-Fecralloy catalysts, with an apparent higher catalytic activity during the cooling down. This phenomenon has several simultaneous origins including both macroscopic effects (e.g. heat and mass transfer effects, temperature and concentration gradients along the reactor), as well as mechanistic and structural effects related to the slow transition from an oxygen-enriched surface and platinum oxide formation during extinction, to a CO-covered surface including Pt reduction and self-inhibition [80 and ref. therein]. Noteworthy, when comparing the characteristic ignition-extinction loop for Pt<sub>370</sub>-Fecralloy and CeO<sub>2</sub><sup>14.2</sup>Pt<sub>370</sub>-Fecralloy samples (both aged at 800 °C for 24h) it clearly appears that the presence of ceria over Pt nanoparticles enlarged the hysteresis from ca. 30 °C to as much as 60 °C, indicating a strong promoting interaction between Pt cores and their reducible oxide shell [80, 81]. In particular, it was shown by *Operando* X-ray absorption spectroscopy that ceria supplied oxygen to the Pt surface in Pt-CeO<sub>2</sub>/Al<sub>2</sub>O<sub>3</sub>, helping to maintain high activity during cooling down by retarding and contrasting the CO self inhibition effect, thus significantly enhancing the catalyst operability under transient conditions [81].

## 2.6 Conclusions

In this work, we have demonstrated how the cathodic deposition of noble metal nanoparticles followed by that of discontinuous oxide layers may be an original and effective way to use electrochemistry for the preparation of active catalysts for low-temperature catalytic combustion processes. Platinum and CeO<sub>2</sub> were deposited, in this order, onto Fecralloy foams to obtain structured catalysts for methanol combustion. The reverse order and the simultaneous deposition of noble metal and metal oxide were not equally successful. The pulsed deposition of Pt enabled us to control size and surface distribution of nanoparticles. The CeO<sub>2</sub> deposit thickness and porosity were controlled through the deposition charge, in order to maintain a significant part of the Pt surface accessible to electrolyte or gaseous reactants.

The CeO<sub>2</sub>-Pt-Fecralloy catalysts were superior to Pt-Fecralloy catalysts with the same noble metal loading. Methanol combustion to yield CO<sub>2</sub> (with negligible CO formation), started around 100°C and reached an asymptotic value, limited by external diffusion mass transfer, around 250°C. Conversion to CO<sub>2</sub> attained 100% when the contact time was sufficiently long. The catalysts were stable and their performance was constant during successive cycles involving temperatures up to 600°C.

The increase in the number of available catalytic active sites in CeO<sub>2</sub>-Pt-Fecralloy was associated to the formation of novel CeO<sub>2</sub>-Pt interface sites that remained easily accessible in the nanoparticles with a quasi-core-shell configuration. Experimental evidence was found that active sites for methanol catalytic combustion represent only a small fraction of the total exposed Pt surface, thus highlighting the fundamental role of those atoms, located at the Pt-Fecralloy and Pt-CeO<sub>2</sub> interfaces, which were accessible to methanol.

Results related to this part of the chapter, including preparation of catalysts and methanol catalytic combustion were reported in [83].

The catalytic oxidation of CO was selected to investigate the effects induced by the core-shell configuration of CeO<sub>2</sub>-Pt nanoparticles on the intrinsic activity of the synthesized materials in the temperature range 200 – 300 °C and on the thermal stability under oxidizing conditions up to 800 °C.

The CO oxidation mechanism was insensitive to the addition of CeO<sub>2</sub> overlayer on Pt particles, as confirmed by the unchanged apparent activation energy and reaction order with respect to both CO and O<sub>2</sub>. Nevertheless, the specific reaction rate per gram of Pt increased significantly, by a factor comprised between 2 and 7, due to the formation of novel active sites at the CeO<sub>2</sub>-Pt interface which are less prone to be “poisoned” by strongly adsorbed CO molecules. The strong promoting interaction between Pt cores and their reducible oxide shell was also testified by a marked widening of the typical temperature hysteresis loop between light-off (ignition) of CO oxidation and its blow-out (extinction).

In fact, it was found that the activity order between CeO<sub>2</sub>-covered Pt catalyst and their bare counterpart can be reverted at high temperature (after ignition, when the Pt surface is free from CO) due to the significant reduction of the total exposed Pt surface area in core-shell systems.

Temperature programmed oxidation tests performed along with the ageing of the CeO<sub>2</sub>-Pt-Fecralloy catalyst at 800 °C in air for increasing times up to a total of 24h indicated a remarkable stability of the intrinsic low temperature CO oxidation activity. In turn, this confirmed the high resistance of core-shell nanoparticles against detachment from Fecralloy, sintering and extensive reconstruction. Activity toward CO oxidation including ceria influence on stability performance were reported in [84].

## 2.7. Bibliography

1. S. Cimino, A. Gambirasi, L. Lisi, G. Mancino, M. Musiani, L. Vázquez-Gómez, E. Verlato, Catalytic combustion of methanol on Pt-Fecralloy foams prepared by electrodeposition, *Chem. Eng. J.* 285 (2016) 276-285.
2. Z. Li, M. Li, Z. Bian, Y. Kathiraser, S. Kawi, Design of highly stable and selective core/yolk-shell nanocatalysts—A review, *Appl. Catal. B Environ.* 188 (2016) 324–341.
3. M.B. Gawande, A. Goswami, T. Asefa, H. Guo, A. V. Biradar, D. Peng, R. Zboril, R.S. Varma, Core-shell nanoparticles: synthesis and applications in catalysis and electrocatalysis, *Chem. Soc. Rev.* 44 (2015) 7540–7590.
4. X. Wang, D. Liu, S. Song and H. Zhang, Pt@CeO<sub>2</sub> Multicore@Shell Self-Assembled Nanospheres: Clean Synthesis, Structure Optimization, and Catalytic Applications. *J. Am. Chem. Soc.* 135 (2013) 15864–15872.
5. N. Almana, S.P. Phivilay, P. Laveille, M.N. Hedhili, P. Fornasiero, K. Takanabe and J.M. Basset, Design of a core-shell Pt-SiO<sub>2</sub> catalyst in a reverse microemulsion system: Distinctive kinetics on CO oxidation at low temperature, *J. Catal.* 340 (2016) 368–375.
6. C. Zhang, S. Li, T. Wang, G. Wu, X. Ma and J. Gong, Pt-Based Core-Shell Nanocatalysts with Enhanced Activity and Stability for CO Oxidation. *Chem. Commun. (Camb).* 49 (2013) 10647-10649.
7. Z. Zhang, J. Li, W. Gao, Z. Xia, Y. Qin, Y. Qu and Y. Ma, Thermally stable sandwich-type catalysts of Pt nanoparticles encapsulated in CeO<sub>2</sub> nanorod/CeO<sub>2</sub> nanoparticle core/shell supports for methane oxidation at high temperatures. *RSC Adv.* 6 (2016) 40323–40329.
8. M. Cargnello, J.J. Delgado Jaén, J.C. Hernández Garrido, K. Bakhmutsky, T. Montini, J.J. Calvino Gámez and P. Fornasiero, Exceptional activity for methane combustion over modular Pd@CeO<sub>2</sub> subunits on functionalized Al<sub>2</sub>O<sub>3</sub>, *Science* 337 (2012) 713–717.
9. S. Lee, J. Seo and W. Jung. Sintering-resistant Pt@CeO<sub>2</sub> nanoparticles for high-temperature oxidation catalysis, *Nanoscale* 8 (2016) 10219–10228.
10. P. Fornasiero, T. Montini, M. Graziani, S. Zilio, M. Succi, Development of functionalized Fe-Al-Cr alloy fibers as innovative catalytic oxidation devices, *Catalysis Today* 137 (2008) 475–482
11. M. Cargnello, T. Montini, S. Polizzi, N.L. Wieder, R.J. Gorte, M. Graziani and P. Fornasiero, Novel embedded Pd@CeO<sub>2</sub> catalysts: a way to active and stable catalysts. *Dalton Trans.* 39 (2010) 2122–2127.
12. Z. Li, L. Mo, Y. Kathiraser, and S. Kawi, Yolk-Satellite-Shell Structured Ni-Yolk@Ni@SiO<sub>2</sub> Nanocomposite: Superb Catalyst toward Methane CO<sub>2</sub> Reforming Reaction. *ACS Catal.* 4 (2014) 1526–36.
13. L. Mo, K.K.M. Leong, S. Kawi, A highly dispersed and anti-coking Ni-La<sub>2</sub>O<sub>3</sub>/SiO<sub>2</sub> catalyst for syngas production from dry carbon dioxide reforming of methane. *Catal. Sci. Technol.* 4 (2014) 2107.
14. Q. Zhang, I. Lee, J.B. Joo, F. Zaera, Y. Yin, Core-shell nanostructured catalysts. *Acc. Chem. Res.* 46 (2013) 1816–24.
15. C.K. Ngaw, Q. Xu, T.T.Y. Tan, P. Hu, S. Cao, J.S.C. Loo, A strategy for in-situ synthesis of well-defined core-shell Au@TiO<sub>2</sub> hollow spheres for enhanced photocatalytic hydrogen evolution, *Chem. Eng. J.* 257 (2014) 112–121.
16. M. Shao, Q. Chang, J.-P. Dodelet, R. Chenitz, Recent advances in electrocatalysts for oxygen reduction reaction, *Chem. Rev.* 116 (2016) 3594-3657.
17. G.N. Vayssilov, Y. Lykhach, A. Migani, T. Staudt, G.P. Petrova, N. Tsud, T. Skála, A. Bruix, F. Illas, K.C. Prince, V. Matolín, K.M. Neyman and J. Libuda, Support nanostructure boosts oxygen transfer to catalytically active platinum nanoparticles. *Nat. Mater.* 10 (2011) 310–315.
18. S. Cimino, L. Lisi, R. Pirone and G. Russo, Dual-Site Pd/Perovskite Monolithic Catalysts for Methane Catalytic Combustion. *Ind. Eng. Chem. Res.* 43 (2004) 6670–6679.
19. M. Cargnello, V.V.T. Doan-Nguyen, T.R. Gordon, R.E. Diaz, E.A. Stach, R.J. Gorte, P. Fornasiero, C.B. Murray, Control of Metal Nanocrystal Size Reveals Metal-Support Interface Role for Ceria Catalysts, *Science* (80-. ). 341 (2013) 771–773.

19. J.A. Rodriguez, D.C. Grinter, Z. Liu, R.M. Palomino and S.D. Senanayake, Ceria-based model catalysts: fundamental studies on the importance of the metal–ceria interface in CO oxidation, the water–gas shift, CO<sub>2</sub> hydrogenation, and methane and alcohol reforming. *Chem. Soc. Rev.* 46 (2017) 1824–1841.
20. A.M. Gänzler, M. Casapu, P. Vernoux, S. Loridant, F.J. Cadete Santos Aires, T. Epicier, B. Betz, R. Hoyer and J.D. Grunwaldt, Tuning the Structure of Platinum Particles on Ceria In Situ for Enhancing the Catalytic Performance of Exhaust Gas Catalysts. *Angew. Chemie – Int. Ed.* 56 (2017) 13078–13082.
21. A. Trovarelli, Catalytic properties of ceria and CeO<sub>2</sub>-containing materials, *Catal. Rev.* 38 38 (1996) 439–520.
22. M. Lykaki, E. Pachatouridou, E. Iliopoulou, S.A.C. Carabineiro and M. Konsolakis, Impact of the synthesis parameters on the solid state properties and the CO oxidation performance of ceria nanoparticles. *RSC Adv* 7 (2017) 6160–6169.
23. J. Jones, H. Xiong, A.T. DeLaRiva, E.J. Peterson, H. Pham, S.R. Challa, G. Qi, S. Oh, M.H. Wiebenga, X.I. Pereira Hernandez, Y. Wang, A.K. Datye, Thermally stable single-atom platinum-on-ceria catalysts via atom trapping, *Science* (80- ). 353 (2016) 150–154.
24. M. Argyle, C. Bartholomew, Heterogeneous Catalyst Deactivation and Regeneration: A Review, *Catalysts*. 5 (2015) 145–269..
25. V. Meille, Review on methods to deposit catalysts on structured surfaces. *Appl. Catal. A Gen.* 315 (2006) 1–17.
26. R. J. Farrauto, Y. Liu, W. Ruettinger, O. Ilinich, L. Shore and T. Giroux, Precious Metal Catalysts Supported on Ceramic and Metal Monolithic Structures for the Hydrogen Economy. *Catal. Rev.* 49 (2007) 141–196.
27. L. Giani, G. Groppi and E. Tronconi, Mass-Transfer Characterization of Metallic Foams as Supports for Structured Catalysts. *Ind. Eng. Chem. Res.* 44 (2005) 4993–5002.
28. S. Cimino, R. Gerbasi, L. Lisi, G. Mancino, M. Musiani, L. Vázquez-Gómez and E. Verlato, Oxidation of CO and CH<sub>4</sub> on Pd–Fecralloy foam catalysts prepared by spontaneous deposition. *Chem. Eng. J.* 230 (2013) 422–431.
29. C. Xu, P.K. Shen, Electrochemical oxidation of ethanol on Pt–CeO<sub>2</sub>/C catalysts, *J. Power Sources* 142 (2005) 27–29.
30. C.L. Campos, C.Roldan, M. Aponte, Y. Ishikawa, C.R. Cabrera, Preparation and methanol oxidation catalysis of Pt–CeO<sub>2</sub> electrode, *J. Electroanal. Chem.* 581 (2005) 206–215.
31. D.J. Diaz, N. Greenletch, A. Solanki, A. Karakoti, S. Seal, Novel nanoscale ceria-platinum composite electrodes for direct alcohol electro-oxidation, *Catal. Lett.* 119 (2007) 319–326.
32. J. Wang, X. Deng, J. Xi, L. Chena, W. Zhua, X. Qiu, Promoting the current for methanol electro-oxidation by mixing Pt-based catalysts with CeO<sub>2</sub> nanoparticles, *J. of Power Sources* 170 (2007) 297–302.
33. M.A. Scibioh, S.-K. Kim, E.A. Cho, T.-H. Lim, S.-A. Hong, H.Y. Ha, Pt–CeO<sub>2</sub>/C anode catalyst for direct methanol fuel cells, *Appl. Catal. B: Environ.* 84 (2008) 773–782.
34. Y. Zhou, Y. Gao, Y. Liu, J. Liu, High efficiency Pt–CeO<sub>2</sub>/carbon nanotubes hybrid composite as an anode electrocatalyst for direct methanol fuel cells, *J. Power Sources* 195 (2010) 1605–1609.
35. D.-J. Guo, Z.-H. Jing, A novel co-precipitation method for preparation of Pt–CeO<sub>2</sub> composites on multi-walled carbon nanotubes for direct methanol fuel cells, *J. Power Sources* 195 (2010) 3802–3805.
36. S. Imamura, T. Higashihara, Y. Saito, H. Aritani, H. Kanai, Y. Matsumura, N. Tsuda, Decomposition of methanol on Pt-loaded ceria, *Catal. Today* 50 (1999) 369±380
37. G. Avgouropoulos, J. Papavasiliou, T. Ioannides, Hydrogen production from methanol over combustion-synthesized noble metal/ceria catalysts, *Chem. Eng. J.* 154 (2009) 274–280.
38. G. Avgouropoulos, Isotopic transient study of methanol decomposition over noble metal/ceria catalysts, *Catal. Comm.* 10 (2009) 682–686.
39. F. Basile, P. Benito, P. Del Gallo, G. Fornasari, D. Gary, V. Rosetti, E. Scavetta, D. Tonelli, A. Vaccari, Highly conductive Ni steam reforming catalysts prepared by electrodeposition, *Chem. Commun.* (2008) 2917–2919.

40. F. Basile, P. Benito, G. Fornasari, V. Rosetti, E. Scavetta, D. Tonelli and A. Vaccari, Electrochemical synthesis of novel structured catalysts for H<sub>2</sub> production, *Applied Catalysis B: Environmental* 91 (2009) 563–572.
41. P. Benito, G. Nuyts, M. Monti, W. De Nolf, G. Fornasari, K. Janssens, E. Scavetta and A. Vaccari, Stable Rh particles in hydrotalcite-derived catalysts coated on FeCr alloy foams by electrosynthesis, *Appl. Catal. B Environ.* 179 (2015) 321–332.
42. S. Cimino, A. Gambirasi, L. Lisi, G. Mancino, M. Musiani, L. Vázquez-Gómez and E. Verlato, Catalytic combustion of methanol on Pt-Fecralloy foams prepared by electrodeposition, *Chem. Eng. J.* 285 (2016) 276–285.
43. E. Verlato, S. Barison, S. Cimino, F. Dergal, L. Lisi, G. Mancino G, M. Musiani and L. Vázquez-Gómez, Catalytic partial oxidation of methane over nanosized Rh supported on Fecralloy foams. *Int J Hydrogen Energy* 39 (2014) 11473–11485.
44. L. Vázquez-Gómez, S. Cattarin, N. Comisso, P. Guerriero, M Musiani, E. Verlato, Spontaneous deposition of Pd onto Fe-Cr-Al alloys, *Electrochim. Acta*, 68 (2012) 114-122.
45. S. Cimino, R. Gerbasi, L. Lisi, G. Mancino, M. Musiani, L. Vázquez-Gómez, E. Verlato, Oxidation of CO and CH<sub>4</sub> on Pd-Fecralloy foam catalysts prepared by spontaneous deposition, *Chem. Eng. J.* 230 (2013) 422-431.
46. A.Q. Wang, T.D. Golden, Anodic Electrodeposition of Cerium Oxide Thin Films I. Formation of Crystalline Thin Films, *J. Electrochem. Soc.* (2003) 150 C616-C620.
47. T.D. Golden, A.Q. Wang, Anodic Electrodeposition of Cerium Oxide Thin Films II. Mechanism studies, *J. Electrochem. Soc.* (2003) 150 C621-C624.
48. A. J. Aldykiewicz, Jr., A. J. Davenport, H. S. Isaacs, Studies of the Formation of Cerium-Rich Protective Films Using X-Ray Absorption Near-Edge Spectroscopy and Rotating Disk Electrode Methods, *J. Electrochem. Soc.* 143 (1996) 147-154.
49. Y. Zhou, Jay A. Switzer, Growth of cerium(IV) oxide films by the electrochemical generation of base method, *Journal of Alloys and Compounds* 237 (1996) 1-5.
50. F.-B. Li, R. C. Newman, G. E. Thompson, In situ atomic force microscopy studies of electrodeposition mechanism of cerium oxide films: nucleation and growth out of a gel mass precursor, *Electrochim. Acta*, 42 (1997) 2455-2464.
51. J. Creus, F. Brezault, C. Rebere, M. Gadouleau, Synthesis and characterisation of thin cerium oxide coatings elaborated by cathodic electrolytic deposition on steel substrate, *Surface & Coatings Technology* 200 (2006) 4636 – 4645.
52. Y. Hamlaoui, F. Pedraza, L. Tifouti, Investigation of electrodeposited cerium oxide based films on carbon steel and of the induced formation of carbonated green rusts, *Corrosion Science* 50 (2008) 2182–2188.
53. V. Fernandes, J. J. Klein, W. H. Schreiner, N. Mattoso, D. H. Mosca, Electrodeposition of Nanocrystalline CeO<sub>2</sub> on Si(001), *J. Electrochem. Soc.* 156 (2009) E199-E204.
54. Y. Hamlaoui, F. Pedraza, C. Remazeilles, S. Cohendoz, C. Rébéré, L. Tifouti, J. Creus, Cathodic electrodeposition of cerium-based oxides on carbon steel from concentrated cerium nitrate solutions Part I. Electrochemical and analytical characterisation, *Materials Chemistry and Physics* 113 (2009) 650–657.
55. Y. Hamlaoui, L. Tifouti, C. Remazeilles, F. Pedraza, Cathodic electrodeposition of cerium based oxides on carbon steel from concentrated cerium nitrate. Part II: Influence of electrodeposition parameters and of the addition of PEG, *Materials Chemistry and Physics* 120 (2010) 172–180.
56. B. Bouchaud, J. Balmain, G. Bonnet, F. Pedraza, pH-distribution of cerium species in aqueous systems, *J. Rare Earths* 30 (2012) 559-562.
57. B. Bouchaud, J. Balmain, G. Bonnet, F. Pedraza, Optimizing structural and compositional properties of electrodeposited ceria coatings for enhanced oxidation resistance of a nickel-based superalloy, *Applied Surface Science* 268 (2013) 218– 224.
58. B. Bouchaud, J. Balmain, G. Bonnet, F. Pedraza, Correlations between electrochemical mechanisms and growth of ceria based coatings onto nickel substrates, *Electrochimica Acta* 88 (2013) 798–806.

59. D. Stoychev, Corrosion protective ability of electrodeposited ceria layers, *J. Solid State Electrochem.* 17 (2013) 497–509.
60. F. Faisal, A. Toghan, I. Khalakhan, M. Vorokhta, V. Matolin, Jörg Libuda, Characterization of thin CeO<sub>2</sub> films electrochemically deposited on HOPG, *Applied Surface Science* 350 (2015) 142–148.
61. M. Haruta, A. Ueda, S. Tsubota, R.M. Torres Sanchez, Low-temperature catalytic combustion of methanol and its decomposed derivatives over supported gold catalysts, *Catalysis Today* 29 (1996) 443–447.
62. N.S. Kaisare, D.G. Vlachos, A review on microcombustion: fundamentals, devices and applications, *Prog. Energy Combust. Sci.* 38 (2012) 321–359.
63. X. Wang, C. Zhang, Z. Zeng, Z. Hu, Preparation of supported noble metal catalysts for methanol catalytic combustion at room temperature, *Combust. Sci. Technol.* 184 (2012) 842–849
64. S. Cimino, R. Nigro, U. Weidmann, R. Holzner, Catalytic Combustion of Methanol over La, Mn-Hexaaluminate Catalysts, *Fuel Process. Technol.* 133 (2015) 1-7.
65. H. Hassannejad, C. Mele, T. Shahrabi, B. Bozzini, Electrodeposition of Ni/ceria composites: an in situ visible reflectance investigation, *J. Solid State Electrochem.* 16 (2012) 3429–3441.
66. ICDD Card 34-0394.
67. ICDD Card 74-0665.
68. R. Woods, Chemisorption at electrodes: hydrogen and oxygen on noble metals and their alloys, in: A.J. Bard (Ed.), *Electroanalytical Chemistry*, vol. 9, Marcel Dekker, New York, 1976, pp. 1–162.
69. M. Fernandez-Garcia, A. Martinez-Arias, L.N. Salamanca, J.M. Coronado, J.A. Anderson, J.C. Conesa, J. Soria, Influence of Ceria on Pd Activity for the CO+O<sub>2</sub> Reaction, *J. Catal.* 187 (1999) 474–485.
70. J. Pasel, B. Emonts, R. Peters, D. Stolten, A structured test reactor for the evaporation of methanol on the basis of a catalytic combustion, *Catal. Today* 69 (2001) 193–200.
71. F. Duprat, Light-off curve of catalytic reaction and kinetics, *Chem. Eng. Sci.* 57 (2002) 901–911.
72. K. Ding, A. Gulec, A.M. Johnson, N.M. Schweitzer, G.D. Stucky, L.D. Marks, P.C. Stair, Identification of active sites in CO oxidation and water-gas shift over supported Pt catalysts, *Science* 350 (2015) 189–192.
73. M. Cargnello, V.V.T. Doan-Nguyen, T.R. Gordon, R.E. Diaz, E.A. Stach, R.J. Gorte, P. Fornasiero, C.B. Murray, Control of Metal Nanocrystal Size Reveals Metal-Support Interface Role for Ceria Catalysts, *Science* 341 (2013) 771–773.
74. L. Giani, G. Groppi, E. Tronconi, Mass-transfer characterization of metallic foams as supports for structured catalysts, *Ind. Eng. Chem. Res.* 44 (2005) 4993–5002.
75. L. Liu, F. Zhou, L. Wang, X. Qi, F. Shi, Y. Deng, Low-temperature CO oxidation over supported Pt, Pd catalysts: Particular role of FeOx support for oxygen supply during reactions, *J. Catal.* 274 (1) (2010) 1–10.
76. P.J. Berlowitz, C.H.F. Peden and D.W. Goodman, Kinetics of Carbon Monoxide Oxidation on Single-Crystal Palladium, Platinum, and Iridium. *J. Phys. Chem.* 92 (1988) 5213–5221.
77. T. Bunluesin, E.S. Putna and R.J.A. Gorte, Comparison of the Dynamics of CO Oxidation on Pt and Pd. *Catal. Letters* 41 (1996) 1-5.
78. F. Duprat, Light-off curve of catalytic reaction and kinetics, *Chem. Eng. Sci.* 57 (2002) 901–911.
79. I. Kvernes, M. Oliveira, P. Kofstad, High temperature oxidation of Fe-13Cr-xAl alloys in air/H<sub>2</sub>O vapour mixtures, *Corros. Sci.* 17 (1977) 237–252.
80. M. Casapu, A. Fischer, A.M. Gänzler, R. Popescu, M. Crone, D. Gerthsen, M. Türk, and J.D. Grunwaldt, Origin of the Normal and Inverse Hysteresis Behavior during CO Oxidation over Pt/Al<sub>2</sub>O<sub>3</sub>. *ACS Catal.* 7 (2017) 343–355.
81. F. Benzi, T.L. Sheppard, D.E. Doronkin, D.M. Meira, A.M. Gänzler, S. Baier, S. and J.D. Grunwaldt, Transient Structural and Catalytic Behaviour of Pt-Particles Probed by Operando Spectroscopy during a Realistic Driving Cycle. *Catal. Sci. Technol.* 7 (2017) 3999–4006.
82. Enrico Verlato, Simona Barison, Stefano Cimino, Luciana Lisi, Gabriella Mancino, Marco Musiani, Francesco Paolucci, Electrochemical preparation of nanostructured CeO<sub>2</sub>-Pt catalysts on Fe-Cr-Al alloy foams for the low-temperature combustion of methanol, *Chemical Engineering Journal* 317 (2017) 551–560.

- 83.** S. Cimino, L. Lisi, G. Totarella, S. Barison, M. Musiani, Highly stable core–shell Pt-CeO<sub>2</sub> nanoparticles electrochemically deposited onto Fecralloy foam reactors for the catalytic oxidation of CO, *Journal of Industrial and Engineering Chemistry* 66 (2018) 404–410.

## CHAPTER 3: CO<sub>2</sub>RR on Cu-based graphenide

### 3.1. Introduction

As described in 1.1, there are two distinct groups of metal catalysts for CO<sub>2</sub> electrochemical reduction: CO forming metals (Cu, Au, Ag, Zn, Pd, Ga, Ni, and Pt) and formate forming metals (Pb, Hg, In, Sn, Cd, and Tl). Copper has a special place, with its capacity of generating a wide range of CO<sub>2</sub> reduction products and promoting carbon-carbon coupling, producing HCOOH, CH<sub>4</sub>, C<sub>2</sub>H<sub>4</sub> and alcohols with very good efficiencies [1, 2]. If we consider CO heats of adsorption, copper is intermediate between Ni and Pt, that strongly adsorb CO, and Au that barely interact with CO. This means that copper adsorb CO with moderate strength and so can produce hydrocarbons through reduction of CO intermediate. Prof. Hori group published the first report of the direct reduction of CO<sub>2</sub> to hydrocarbons on a copper electrode, with focus on obtaining reasonable current densities and efficiencies [3]. The authors obtained 69% of methane and ethylene at 0°C with currents of 10-20 mA/cm<sup>2</sup>. CO<sub>2</sub> Electrochemical reduction attracted recently a great attention and many reviews have covering the literature about transition metal electrodes have been published [2, 4, 5]. More specifically, Gupta and Cottrell in 2006 published an in depth review focused on copper electrodes in aqueous electrolytes, including a comprehensive literature description [6]. They observed that CO<sub>2</sub> reduction over copper electrode lead to hydrocarbons following multiple different multi-step pathways sharing different intermediates. The reaction yield and the products distribution strongly depend on electrolyte pH, composition and temperature, on CO<sub>2</sub> pressure and on surface structure [2]. For polycrystalline copper, usually a large applied overpotential is required to obtain hydrocarbons. At potential values around -0.6V vs SHE, Cu electrodes generate low currents and HER strongly prevails. Under these conditions, reduction of CO<sub>2</sub> produce at most 20% of CO or HCOOH. Decreasing potential to -0.8V vs SHE, the onset of hydrocarbons production is observed, which is related to further reduction of adsorbed CO\* to intermediates that are less strongly adsorbed [3, 7]. To enhance the catalytic activity of Cu, many authors have proposed approaches that included a surface activation mainly based on surface oxidation/reduction steps [8-12]; this activation was performed electrochemically or by thermal and plasma treatments. The activation consists in producing surface oxides and then reducing them to induce a surface reconstruction. In all cases these activation procedures caused an increase in CO<sub>2</sub> reduction currents, due to increased roughness, and sometimes an increase of efficiency and/or selectivity. The best results with this approach were obtained by Li and co-workers who prepared their electrodes by annealing a Cu foil and successively reducing it electrochemically. They obtained more than 40% of formate at potentials around -0.5V vs RHE [8].

Different attempts aimed at increasing the performance of copper electrodes were done using alloys or nanostructured materials [12-15]. One of their main advantages on nanostructure for CO<sub>2</sub> electrochemical reduction is related to surface poisoning. Nanomaterials have very large surface/mass ratios, so the presence

on impurities that poison the electrode by surface adsorption, becomes more tolerable. Another key aspect of nanostructures is related to the tailoring of electrode surface; in fact, nanoparticles can be prepared with high amounts of grain boundaries and with preferential lattice orientations that can lead to better performance without the need of activation processes. Wang and co-workers reported a study on different etched nanocubes, obtaining for specific enriched facets more than 60% methane selectivity but they did not report faradaic efficiencies nor described prolonged electrolyses [15]. Reske and co-workers studied the relation between activity and nanoparticle dimension, and reported no significant variations and poor performances compared to bulk copper [13]. On the contrary, Li and co-workers using 1:1 or 1:2 mixtures of copper nanoparticles and pyridinic-N rich graphene obtained, for potential of -0.8 vs RHE, close to 60% formate. However, they obtained similar values for just the pyridinic-N rich graphene phase that resulted very active toward CO<sub>2</sub> [14]. The mechanism of reaction on different types of electrode remain under debate. Some proposed mechanisms are summarized in Raciti and Wang review, based on studies on single crystal or highly oriented electrodes [2]. Alloys also produce a change of reaction mechanism; when copper is coupled with gold or silver, HER is suppressed and reaction lead to an increase of efficiencies for multi-carbon products [16] or, in case of gold-copper nanoparticles, for CO [17]. However, in general, efficiencies toward products like formate or methane remains low, below those measured for polycrystalline copper.

In electrochemistry nanostructures advantages are widely recognised, but notoriously, they have also some major drawbacks. The main limitations for application in electrochemical processes are related to their limited stability due their tendency to aggregate and form cluster. The use of a fine nanoparticle dispersion on porous support like alumina or zeolites was successful for some higher temperature catalysis applications but for electrochemistry, where a support with good conductivity is essential, carbon materials are the preferred choice. Unfortunately, carbon powders show limited stabilization effect on nanoparticles used in fuel cell. After extended experiments under operational conditions, catalysts showed nanoparticle aggregation and leaching [18]. To prevent such drawback, nanoparticles grown on template carbon materials seem to be ideal, thanks to their intrinsic high surface area and to their co-catalytic effect [19]. Recently, Hof and co-workers have published the preparation and electrochemical application of iron oxide nanoparticle embedded on graphene sheets, obtained taking advantage of reducing potential of graphite intercalation compounds (GICs). The iron-graphene composite material showed remarkable activity and stability [20]. Dr. Hof, from Dr. Alain Penicaud group, prepared similar materials containing copper instead of iron [21]. We used this innovative copper/graphenide material to perform a preliminary study on CO<sub>2</sub> electrochemical reduction. We briefly report the preparation and characterization of electrodes and some preliminary results about their use toward CO<sub>2</sub> electrochemical reduction. We focused our attention mainly on formate production and on the relation between current efficiency and overpotential applied.

### 3.2. Preparation

Graphite intercalated with alkali metals are belongs to the group of graphite intercalation compound (GICs) [22].  $KC_8$  is a stage 1 intercalation compound and is structurally composed by alternating layers of graphene and the intercalant potassium. A full charge separation is occurring generating one negative charge for eight carbon atoms, which can be exploited to exfoliate the material to graphenide solutions containing sheets stabilized energetically [22]. This graphenide solution is a strong reducing agent. Our starting carbon material was obtained from microwave plasma splitting of biogas [23] and was intercalated with metal potassium under inert gas conditions (step A). Graphenide solutions were obtained upon dissolving a nanocarbon intercalation compound of formula  $KC_8$  in THF (step B). Scheme 1 and 2 resume the preparation steps of graphenide solution. The lateral size of the nanocarbons in solution is 15-30 nm wide and is 0.5-1.5 nm thick, measured by AFM.

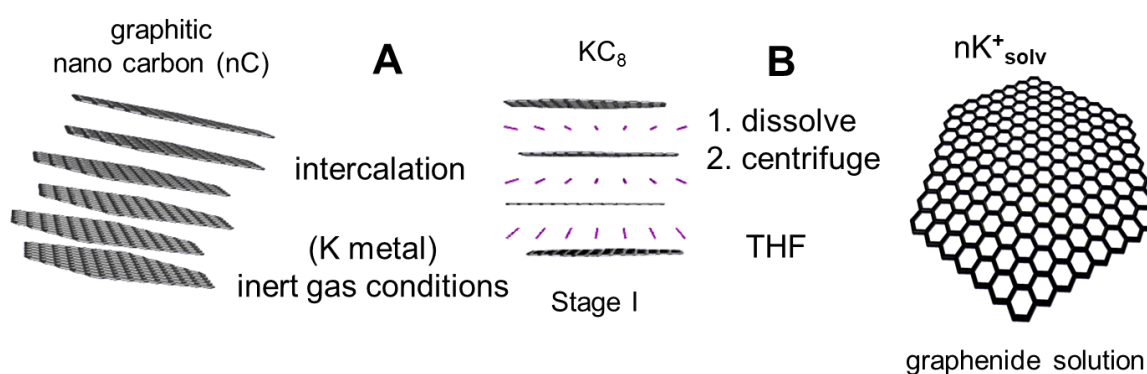


**Fig.1.** Scheme of preparation of the graphenide solution

As shown in Figure 2, the composite material henceforth called  $Cu(nP)/nC$ , was obtained by reacting graphenide solutions with equimolar amounts of anhydrous copper-chloride solutions in THF (step C). This lead to the precipitation of what we assume are copper nanoparticles on the carbon framework. The final powder of composite was obtained by freeze-drying isolation after some cycles of centrifugation/redispersion in water; this procedure leads to further oxidation of nanoparticles to copper oxides/hydroxides. The twofold role of the graphenide solution was to reduce the metal salt, to form nanostructured material and, simultaneously, to control the size of copper nanoparticles.

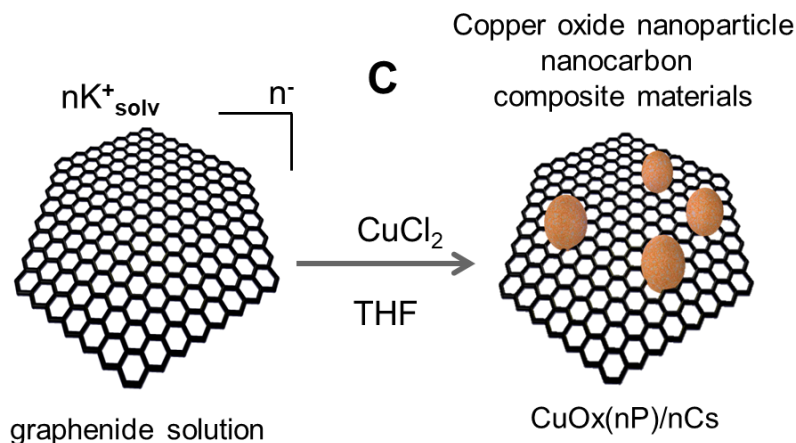


**Fig.2.** Scheme of preparation of the copper/carbon composite material from graphene solution.

### 3.3. Characterization

Morphological characterization was performed by HR-TEM analysis. Copper nanoparticles showed sizes between 1 and 5 nm, with a fairly narrow distribution, as shown in Figure 3.

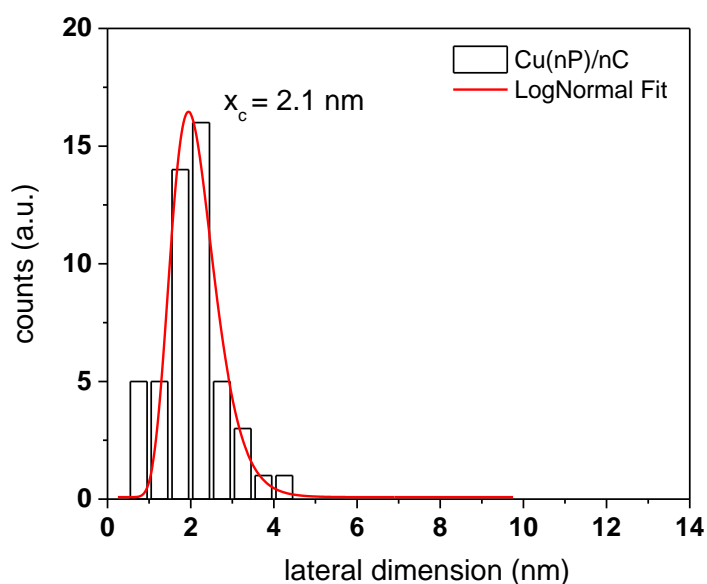


**Fig.3.** Lateral size statistics of  $\text{Cu}(nP)/nC$  composite materials. The statistical basis is 50 counts of individual objects (metal oxide nanoparticles) in about 20 HR-TEM images with atomic resolution.

Fig.4a shows a low magnification TEM image that perfectly matches the EDX map registered on the same sample (Fig.4b); copper was detected just in correspondence of carbon phase, demonstrating that no free nanoparticles were present. This aspect is of particular importance for electrocatalysis applications, as it is known that free nanoparticles are prone to leaching during operational conditions. Moreover, when

composite materials are obtained from reduced graphene oxide or from solutions of graphene stabilized by surfactants, nanoparticle and carbon matrix are bonded through weak Wan der Walls interactions. In contrast, copper nanoparticles in our samples seem to graft strongly on carbon, probably because they grow directly on carbon framework, and this could lead to a carbide-like bond. Higher magnification images (Fig.4c,d) show how nanoparticles were distributed on the carbon matrix, with relatively limited agglomeration.

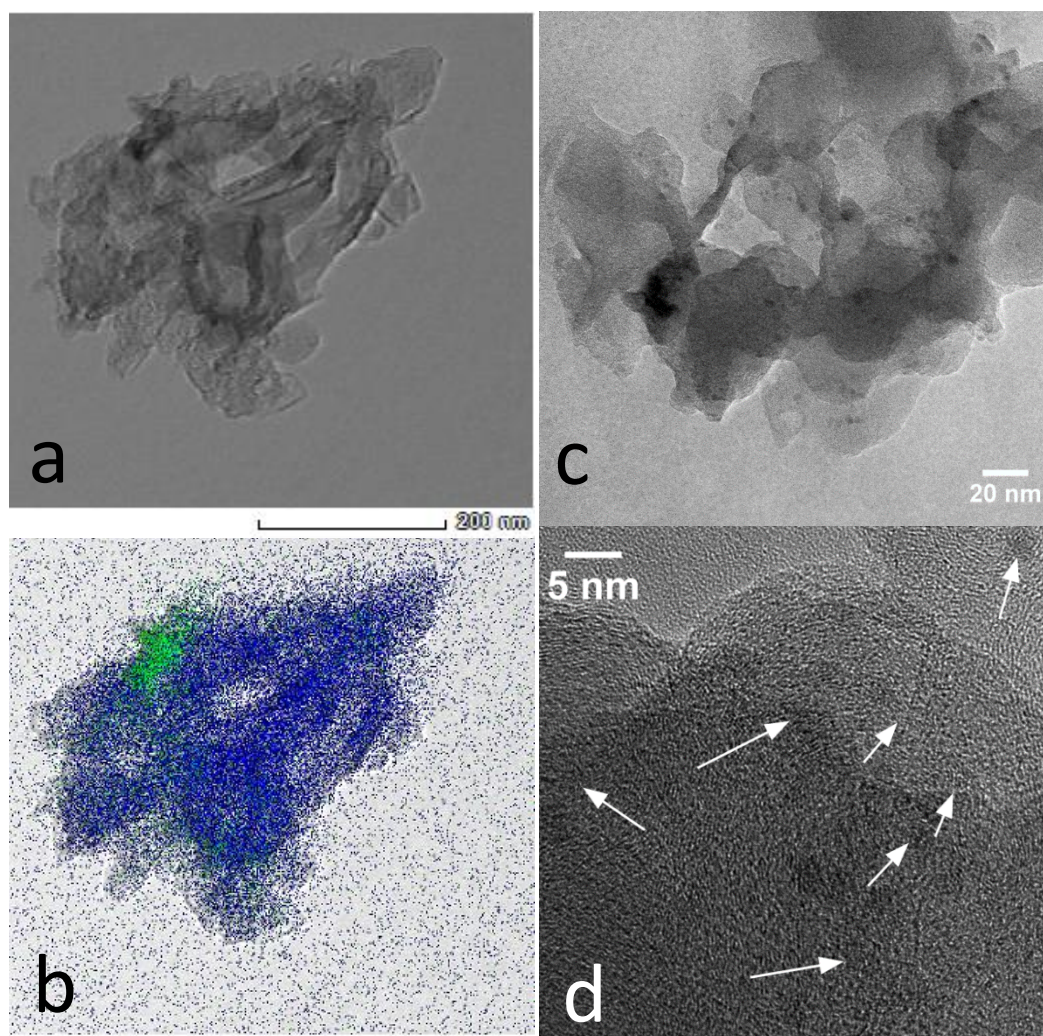


**Fig.4.** (a) Lower magnification bright field HR-TEM image of an aggregate of the Cu(nP)/nC composite sample and (b) the corresponding EDX map. (c, d) Respectively lower and higher magnification HR-TEM image of the Cu(nP)/nC.

To determine different phases present in our composite material and their crystal structure we registered some XRD spectra (Figure 5). As expected, reflections peak were broad due to nanometric nature on copper and carbon obtained. However, the diffractograms showed several reflections due to the compounds constituting the composites material. The starting carbon exhibited a peak at  $25.9^\circ$  that origins from the (002)

peak of turbostratic graphite; three reflections at 29.5°, 36.5° and 42.3° were generated, respectively, by Cu<sub>2</sub>O (110), Cu<sub>2</sub>O (111) and Cu<sub>2</sub>O (200) [24]. At 16.3° there was a weak reflection due to Cu(OH)<sub>2</sub> (020) [25].

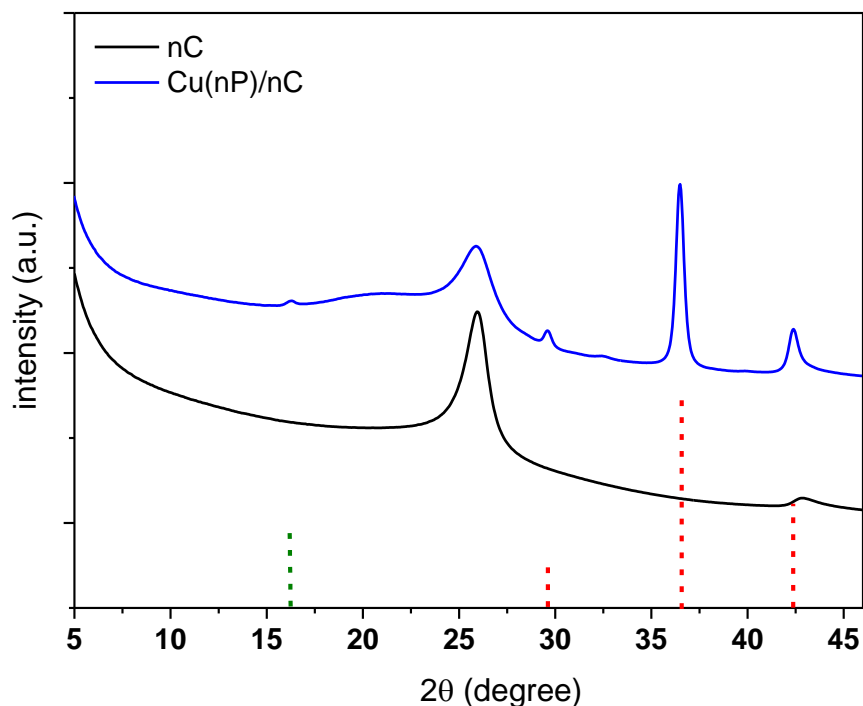


**Fig.5.** Powder X-ray diffraction measurement between 5 and 46° on the graphitic nano carbon (black trace) and on the Cu(nP)/nC composite (blue trace). Green and red dotted lines represent, respectively, reflection of Cu(OH)<sub>2</sub> and Cu<sub>2</sub>O PDF card.

XPS spectra (Figure 6) confirm the presence of copper species [26], and a minor presence of oxygen on the nanocarbon matrix. A quantitative analysis performed calculating the ratio between different peak areas obtained by fitting XPS spectra gave the following rough composition: C<sub>1s</sub> [at %]=91%, O<sub>1s</sub> [at %]=6% and Cu<sub>2p</sub> [at %]=3%.

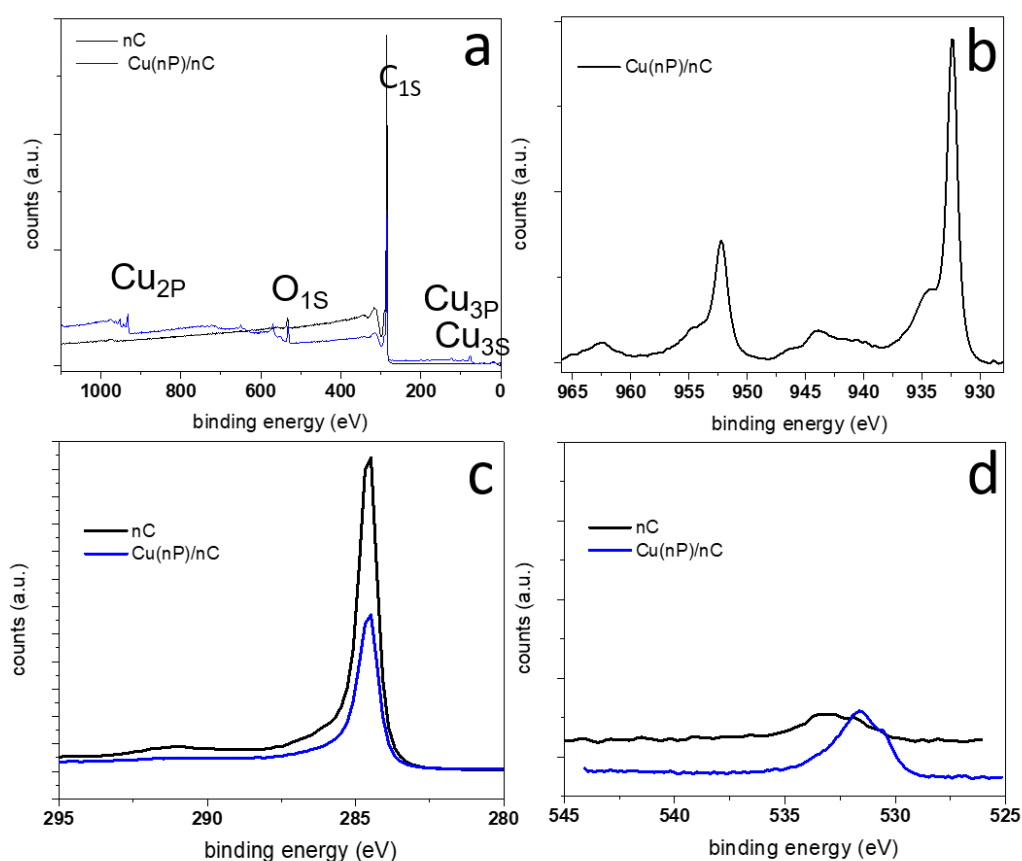


**Fig.6.** (a) XPS measurements on the Cu(nP)/nC composite materials (blue) in comparison to the starting carbon material (black). XPS high-resolution measurements of respectively: copper (b), carbon (c) and oxygen (d) regions of the Cu(nP)/nC composite materials and the starting carbon material.

An accurate peak fitting of Cu2p region (Figure 7) confirmed the presence of two copper species: copper (I) oxide and copper (II) hydroxide, in agreement with what we found through the XRD analyses. Integration of Cu2p peaks of the phases gives an atomic percentage composition of roughly 45% of copper (I) and 55% of copper (II), that correspond to molar composition, respectively, of 38% and 62%. We don't know how the phases are distributed in the nanoparticle volume but we can speculate that, since copper (I) would be oxidized in air, Cu(nP)/nC contained core-shell nanoparticles, with a Cu<sub>2</sub>O nucleus covered by a shell of Cu(OH)<sub>2</sub>.

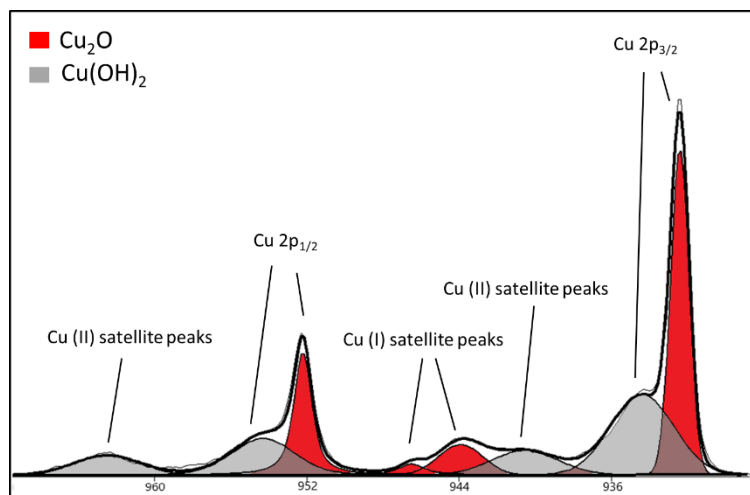


**Fig.7.** XPS high-resolution measurements and spectral fits of the Cu  $2p_{3/2-1/2}$  region.

Assuming copper nanoparticles to be spheres and considering crystal densities reported in literature [27, 28] we calculated volume composition from mass composition and the thickness of both copper compounds layers in the core-shell particles. Values are reported in Table 1.

**Table 1**

Copper phases	XPS area Cu $2p_{1/2}$	XPS area Cu $2p_{3/2}$	Cu At.% amount %	Mass amount %	Crystal Density gr/cm <sup>3</sup>	Volume composition %	Thickness nm
Cu(OH) <sub>2</sub>	16807	8403	45	53	3.95	64	≈1.35
Cu <sub>2</sub> O	19906	9953	55	47	6.1	36	≈0.75

To perform electrochemical experiments a suspension of 0.5 mg/mL of Cu(nP)/nC in THF was prepared and then different volumes of solution were transferred and fixed on a glassy carbon electrode by a drop-cast procedure. The nature of this electrode preparation implies a certain variability in the amount of material deposited on each electrode. Therefore, mass or surface area of copper nanoparticles must be measured to normalize electrocatalytic activities and compare them with literature data. Atomic emission spectroscopy can be employed to measure loading after electrocatalysis experiments but the destructive nature of the technique, the difficult dissolution of the electrode with danger of losing material and the very low quantity of copper present at the electrode, can limit its application. Electrochemical techniques such voltammetries, polarography, electrochemical impedance spectroscopy, EQCM were widely employed to measure electrochemical active surface area or electrode loading [29]. Our approach consists in measuring the total reduction charge of copper oxide/hydroxides during a slow LSV. When the scan rate is sufficiently low, we can assume, due to the dimension of copper nanoparticles, that almost all copper (I) or (II) species are

reduced to metallic copper [30]. In fact, considering the  $\approx 2$  nm average size of our copper nanoparticles and the crystal dimensions of  $\text{Cu}(\text{OH})_2$  ( $2.94 \times 10.59 \times 5.256 \text{ \AA}$ ) and  $\text{Cu}_2\text{O}$ , ( $4.267 \times 4.267 \times 4.267 \text{ \AA}$ ) [24, 25], the reduction of a few monolayers of hydroxide/oxide copper is sufficient to exhaustively reduce all copper based nanoparticles. Fig.8a report a LSV recorded in carbonate buffered solution on an electrode prepared by drop-cast. During the first scan, we observed only a single reduction peak starting at  $-0.2\text{V}$  vs HgO, whereas a second sweep did not show any peak but just a current due to concomitant HER and  $\text{CO}_2$  reductions. We calculated the reduction charge, that was proportional to number of moles reduced at the electrode. Drop casting of different amounts of catalyst dispersion lead to different reduction charges that were roughly proportional to volume deposited. In Fig.8b it is shown that two electrodes prepared with different amounts of catalysts gave reduction charges that scaled very well with the drop cast volume used.

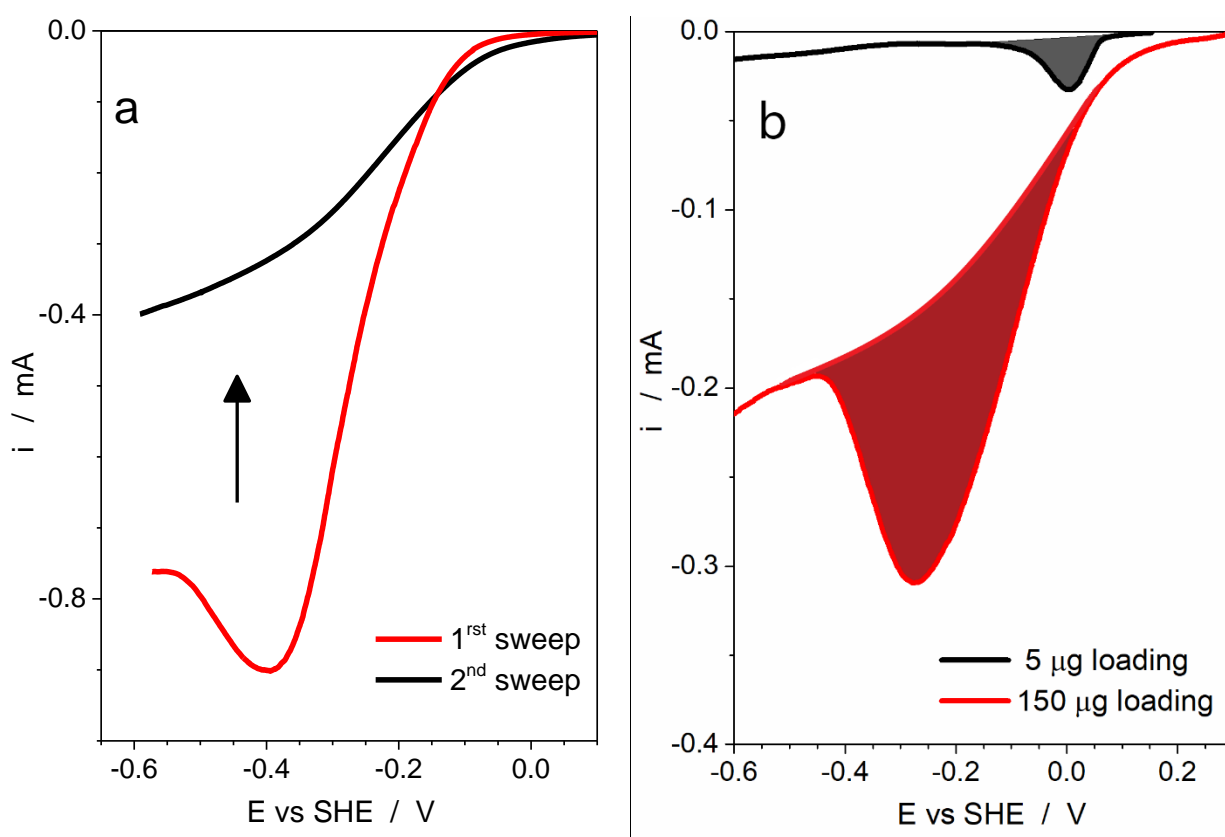
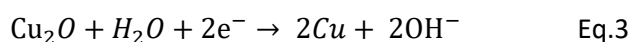
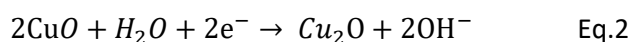
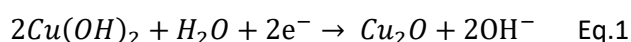


**Fig.8.** LSV in 0.1M  $\text{KHCO}_3$  saturated with  $\text{CO}_2$  scan rate  $1\text{mV/s}$ . (a) report two consecutive experiments, (b) LSV on two electrode prepared by drop-cast with transferred volumes of 300 (red, 150  $\mu\text{g}$ ) and 10 (black, 5  $\mu\text{g}$ )  $\mu\text{L}$ .

Possible reactions involved while sweeping cathodically the electrode are:



Based on XRD data presented above and on the Pourbaix diagram of copper (Fig.9) the  $\text{Cu}(\text{nP})/\text{nC}$  samples

should contain only  $\text{Cu}(\text{OH})_2$  and  $\text{Cu}_2\text{O}$ , so the occurrence of equation 2 may be neglected. The single peak that we observed was probably due to reduction of copper hydroxide and cuprous oxide to metallic copper. Such a broad reduction peak covering a wide potential range was already reported in literature for copper electrodes in alkaline media and attributed to complex multistep reactions that include both equation 1 and 3 and ultimately lead to metallic copper [31-32].

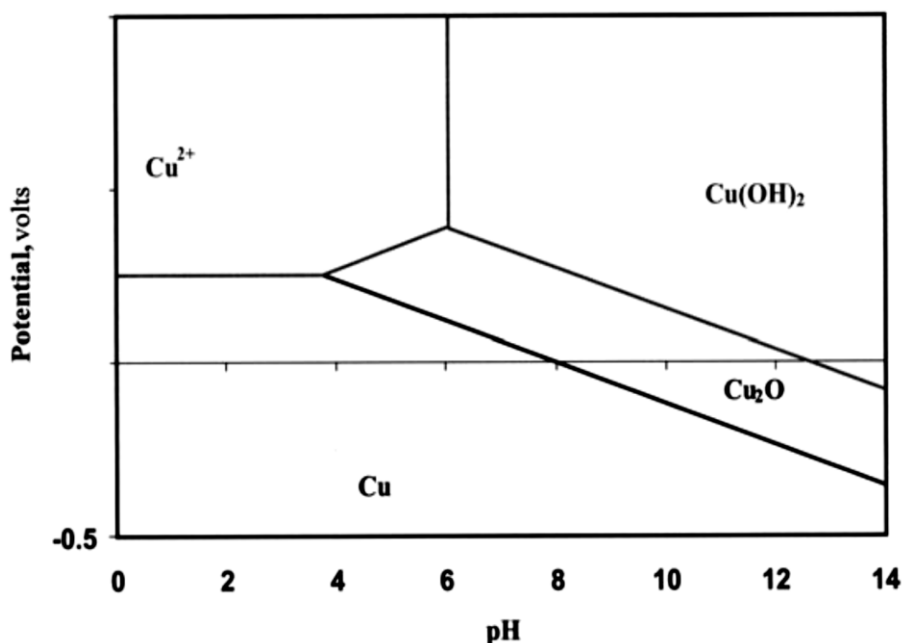
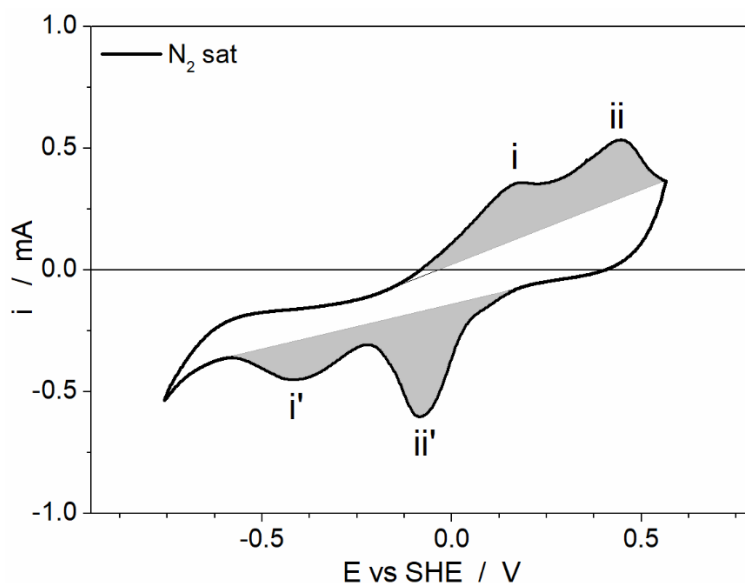


Fig.9. Pourbaix diagram of Cu species in water.[33]

This behaviour is strongly related to the presence of copper (II) hydroxide; when we cycle between 0.5V and -0.7V (Figure 10) we observe the typical behaviour of bulk copper electrodes with oxidation of Cu to  $\text{Cu}_2\text{O}$  (i) and  $\text{Cu}_2\text{O}$  to  $\text{CuO}$  (ii) and the corresponding well separated reduction peaks (i' and ii'). Anodic and cathodic charges keep the same value while cycling, thus evidencing no loss of copper while cycling in that potential window. From reduction peak charge obtained with LSV (Figure 8), we were able to calculate electrode loading. We considered that the copper nanoparticles were made of different amounts of  $\text{Cu}_2\text{O}$  and  $\text{Cu}(\text{OH})_2$  (quantified thanks to XPS data). We calculated moles and mass of copper obtained by reducing both phases to metal Cu and found that our samples showed loadings between 14  $\mu\text{g}$  and 21  $\mu\text{g}$ , with an average of 17  $\mu\text{g}$ . That value, considering a total loading of 150  $\mu\text{g}$  correspond to a Cu atom percentage of 2.2% very close to the one obtained by XPS fitting analysis.



**Fig.10.** CV on a Cu(np)/nC electrode after an electrolysis in 0.1M KHCO<sub>3</sub> scan rate 50 mV/s. In grey, anodic and cathodic peaks area of copper redox systems.

When a bicarbonate solution is saturated with CO<sub>2</sub>, its pH decreases from 8.2 to 6.8. If we perform LSV on Cu(np)/nC electrodes, while gradually saturating the solution, we obtain an increase of cathodic current, due to HER enhancement, and a shift of peak reduction potential towards less negative values (Fig.11). Both effects are related to pH decrease since: (i) HER is favoured when pH is lower and (ii) the standard reduction potential of copper (II) oxide increases according to:  $E_0 = 0.669 - 0.0591 * pH$ .

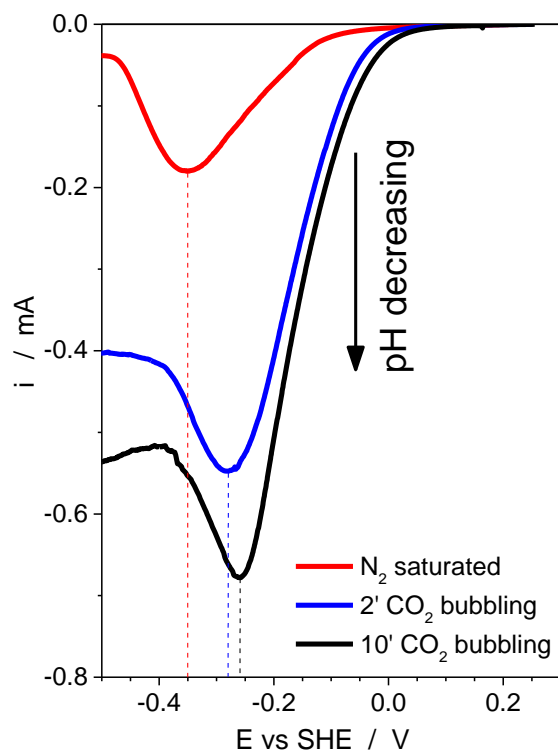


**Fig.11.** LSV of different Cu(np)/nC electrodes in 0.1M KHCO<sub>3</sub> solution. Each LSV was registered with increasing CO<sub>2</sub> bubbling time. Dotted lines indicate peak potentials.

### 3.4. Study of electrochemical CO<sub>2</sub>RR

Even if the reaction mechanisms are still unclear, it is widely recognised that electrode active sites for CO<sub>2</sub> electrochemical consist of metallic copper. Therefore, a pre-treatment that causes the reduction of Cu(I) and Cu(II) species is necessary to obtain metallic copper that can efficiently reduce CO<sub>2</sub>. Reduction through a slow linear voltammetry (as shown in Figure 8) is a viable approach. Since the reduction potential of copper oxides/hydroxides is generally less negative than the potential of CO<sub>2</sub>RR, metallic Cu can be obtained by just polarising the electrode at the electrolysis potential and let it reduce copper oxide before or while reducing CO<sub>2</sub>. However, this approach has two major drawbacks: (i) is difficult to estimate electrolysis charge and separate the contribution of copper reduction, (ii) for very large overpotentials, rapid reduction can induce the detachment of nanoparticles, due to the rapid change of molar volume of copper phases. Moreover it seems that the reduction of copper oxide and the formation of highly active surface sites for CO<sub>2</sub> reduction are not strictly related [34]. We performed electrolysis with both procedures and observed that when we performed a pre-electrolysis by linear sweep, the electrodes showed increased current stability, probably due to reduced loss of materials.

As we observed on chapter 1, studies on CO<sub>2</sub> electrochemical reduction carried out with voltammetries may lead to misleading interpretation of the processes. For this reason, we prefer to study activity of our material mainly with potentiostatic techniques. In Fig.12 we reported a chronoamperogram recorded during a 2-hour electrolysis. After 1 hour we shifted from nitrogen to carbon dioxide bubbling, obtaining a reduction current increase. The enhancement was greater than expected as a result of the pH decrease. This is the evidence that the Cu(nP)/nC electrode showed activity toward CO<sub>2</sub> reduction at potentials as low as -0.54V vs SHE.

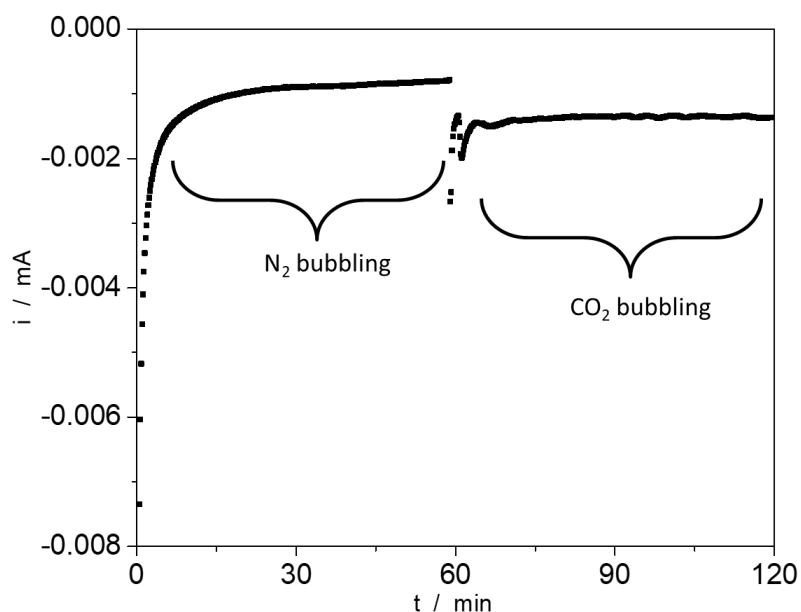


**Fig.12.** Chronoamperogram registered on a Cu(nP)/nC electrode at  $E=-0.540V$  vs SHE. After 1h of polarization gas bubbling was switched from  $N_2$  to  $CO_2$ .

The electrochemical reduction of CO<sub>2</sub> was studied at potentials from -0.56V to -1.26V vs SHE. Chronoamperometries showed stable currents and an increase of noise for the more cathodic potential values, probably due larger amount of gas evolved on the electrode surface. Fig.13a shows chronoamperograms recorded at various potentials and Fig.13b shows two couples of experiments performed with or without pre-electrolysis. Electrodes that were not pre-reduced by LSV showed a longer transient to reach a stable current and a worse stability, thus confirming concerns, mentioned above, about directly performing CO<sub>2</sub> reduction without reducing first the copper species at the electrode.

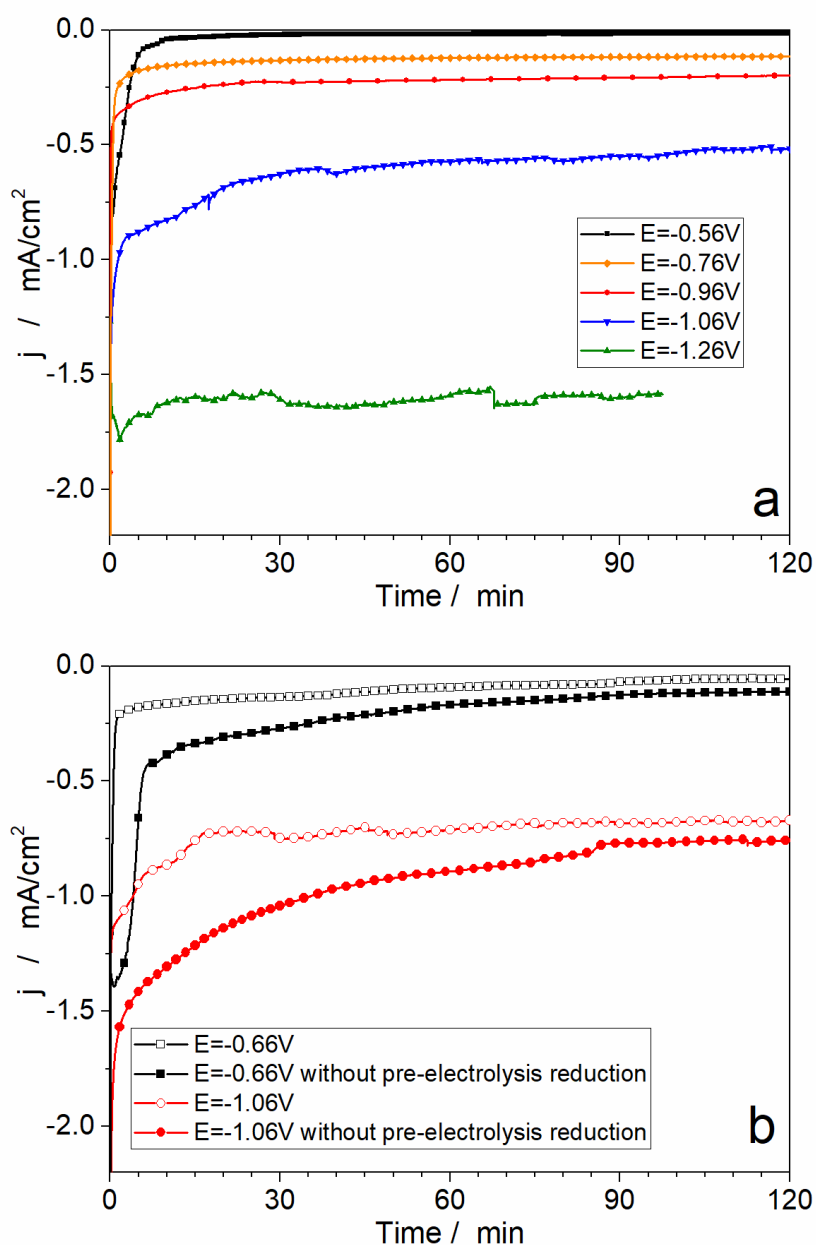


**Fig.13.** CO<sub>2</sub> electrolysis performed in 0.1 carbonate buffer solution on Cu(nP)/nC electrodes with theoretical loading of 150  $\mu$ g. Registered: (a) at different potentials, (b) at different potentials with (full symbols) or without (empty symbols) pre-electrolysis reduction. Potentials applied reported vs SHE.

Despite performing a pre-electrolysis to purify electrolyte, we observed a 20-30% decrease of current during a 4h long electrolysis. We know from literature that this phenomenon can be related to electrode surface poisoning [1]. Even if purified by pre-electrolysis, electrolyte can be contaminated by residual THF used in the drop cast procedure (and possibly impurities present in it) as the copper amount is so small that even diluted impurities may be enough to contaminate part of its surface. Another hypothesis is the loss of composite material during prolonged electrolysis; we are still evaluating this possibility performing some post-electrolysis characterization. Fig.14 shows values of stationary currents obtained at different potentials over different electrodes, with or without LSV pre-electrolysis. A clear trend shows how a reduction process occurred from ca. -0.5V. This process was not related to copper oxides reduction, because the current values plotted in Figure 14 were measured after 2h of electrolysis, when copper oxides/hydroxides were fully reduced. Several electrolysis performed in a row on the same electrode, corresponding to 16-20 h of total electrolysis time, shown electrode degradation, still maintaining some activity.

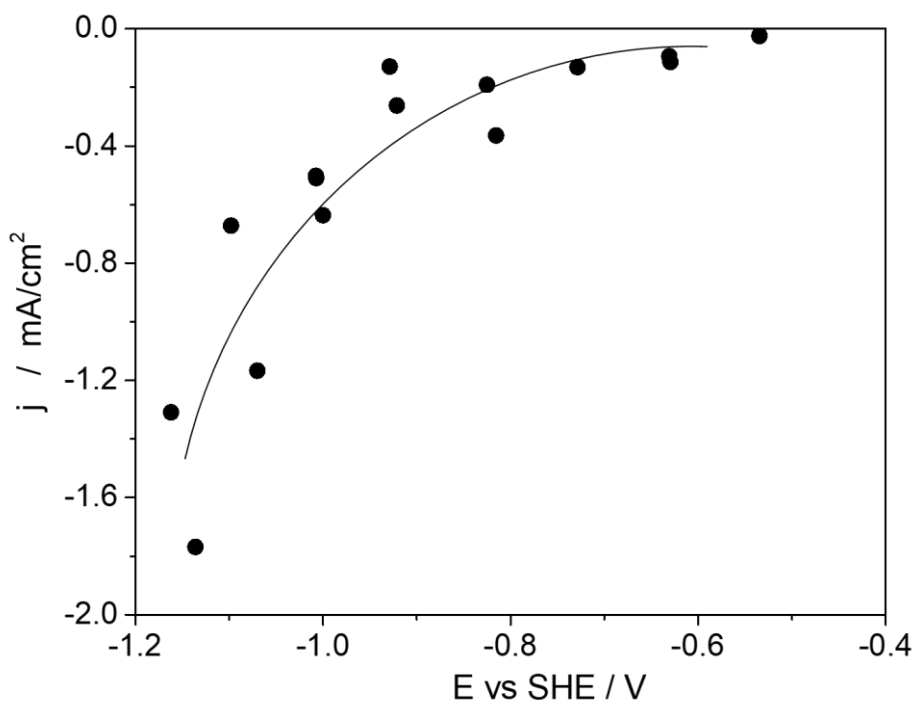


**Fig.14.** Stationary currents registered after 2h of electrolysis on Cu(nP)/nC electrodes with theoretical loading of 150  $\mu\text{g}$  at different potentials corrected for ohmic drop, electrolyte resistance measured with EIS as described in appendix. Black line is just an aid for eye

Regarding selectivity of  $\text{CO}_2$  reduction process we analysed the liquid phase with ion chromatography (Appendix A1.x) to determine formate production. We tried also to measure methane and hydrogen production, but the cell geometry prevented an accurate estimation. We accumulated gas in the cell for 1h and then we analysed it to determine the concentration of  $\text{H}_2$ . In this way we were able to obtain a trend of hydrogen production, though with low quantitative accuracy. The formate production started at an overpotential around 270 mV, with a yield of few percent; yield increased progressively with the overpotential, attaining values of ca. 50% at  $\eta \approx 700$  mV. This remarkable result exceed what Hori obtained

with polycrystalline copper and what Kanan and co-workers obtained with copper-activated electrode. Although, a direct comparison between very different electrodes is difficult, mechanism of reaction seems to be the same of electrodes that have a high amount of grain boundaries, where presumably CO adsorb [2, 8]. The potential of formation of formate matches those already reported for copper nanostructured materials [8]. We calculate turnover number and turnover frequency with following formulas:

$$TON = \frac{mol_{formate}}{mol_{Cu}} \quad TOF = \frac{TON}{t}$$

where  $mol_{Cu}$  are the moles of metallic copper present in the electrode calculated from table 1 and  $mol_{formate}$  are the number of moles of formate produced during the electrolysis. They are calculated from electrolysis total charge  $Q_{tot}$  multiplied by formate faradaic efficiency  $F.E._{formate}$  and divided by faraday constant and by  $n$ , the number of electrons involved in the process (in our case 2, eq.):

$$mol_{formate} = \frac{Q_{tot} \times F.E._{formate}}{96485 \times n}$$

TON values are in the order 35 for the best catalysts; TOF reaches 18 as best value. In the insert of Fig.15 we reported TOF values for several  $CO_2$  reduction potentials. We found that HER, estimated by GC, became relatively less important at higher overpotentials. We speculate that some methane may be formed together with formate and that the yield of both these chemicals would drop over a certain overpotential. Further confirmation could be achieved by exploring more negative potentials, to observe formate efficiency drop when other hydrocarbons are produced, but we were restricted by limited mechanical stability of electrodes under heavy gas evolution.

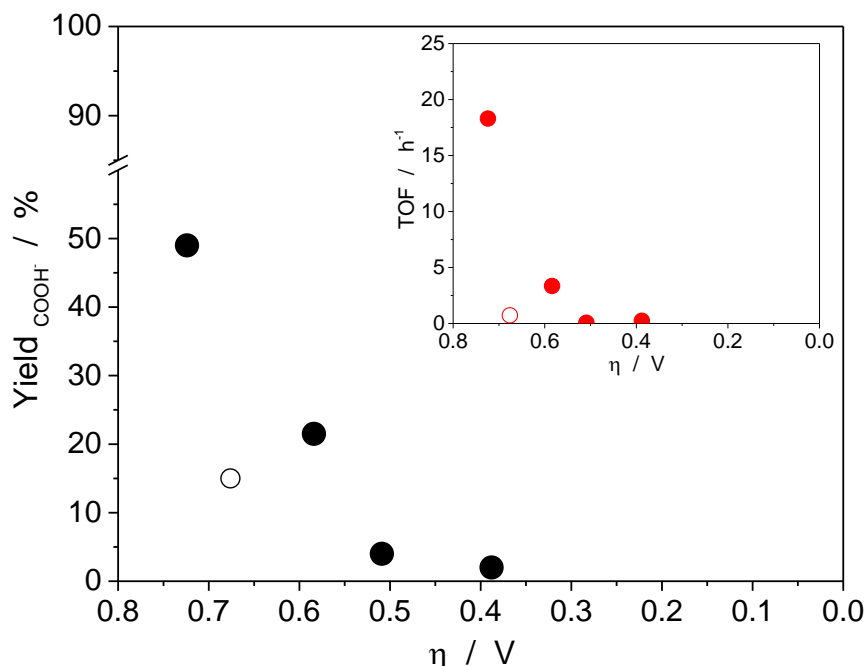


**Fig.15.** Formate faradaic efficiency calculated from experiments at different overpotentials. Insert show TOF values in function of overpotential. Empty symbol represents electrode used several times.

### 3.5. Conclusions & Outlooks

Graphenide solutions from nanocarbons provided small-sized copper nanoparticles, ideal for electrocatalytic purposes. The preparation process is robust and controllable, in contrast to nanoparticle synthesis involving reduced graphene oxide (RGO) or surfactant-stabilized few-layer graphene. Electrochemical reduction of CO<sub>2</sub> at Cu(np)/nC gave a formate yield as high as 50% at an overpotential of 680mV. Prolonged electrolyses showed stable currents with limited poisoning of the electrode. These results place these materials among the best copper-based electrocatalysts reported in literature, in terms of formate efficiency. Future perspective include a complete analysis of gas phase during CO<sub>2</sub>RR and a post reaction characterization of electrodes, to verify how much composite material was lost during experiments.

### 3.6. Bibliography

1. Hori Y. In: Vayenas C.G., White R.E., Gamboa-Aldeco M.E. Modern Aspects of Electrochemistry n°42 (Springer, New York 2008).
2. David Raciti, Chao Wang, Recent Advances in CO<sub>2</sub> Reduction Electrocatalysis on Copper, ACS Energy Lett. 3 (2018) 1545–1556.
3. Hori, Y.; Murata, A.; Takahashi, R. , Formation of Hydrocarbons in the Electrochemical Reduction of Carbon-Dioxide at a Copper Electrode in Aqueous-Solution, J. Chem. Soc., Faraday Trans. 1 (1989) 2309–2326.
4. James W. Vickers, Dominic Alfonso, Douglas R. Kauffman, Electrochemical Carbon Dioxide Reduction at Nanostructured Gold, Copper, and Alloy Materials, Energy Technol. 5 (2017) 775 –795.
5. Ruud Kortlever, Jing Shen, Klaas Jan P. Schouten, Federico Calle-Vallejo, Marc T. M. Koper, J. Phys. Chem. Lett. 2015, 6, 20, 4073-4082, Catalysts and Reaction Pathways for the Electrochemical Reduction of Carbon Dioxide.
6. M. Gattrell, N. Gupta, A. Co, A review of the aqueous electrochemical reduction of CO<sub>2</sub> to hydrocarbons at copper, J. Electroanal. Chem. 594 (2006) 1-19.
7. Yoshio Hori, Akira Murata, Ryutaro Takahashi, Shin Suzuki, Enhanced formation of ethylene and alcohols at ambient temperature and pressure in electrochemical reduction of carbon dioxide at a copper electrode, J. Chem. Soc., Chem. Commun. 0 (1988) 17-19.
8. Li, C. W., Kanan, M. W., CO<sub>2</sub> Reduction at Low Overpotential on Cu Electrodes Resulting from the Reduction of Thick Cu<sub>2</sub>O Films. J. Am. Chem. Soc. 134 (2012) 7231–7234.
9. Lee, S., Kim, D., Lee, J., Electrocatalytic Production of C3-C4 Compounds by Conversion of CO<sub>2</sub> on a Chloride-Induced Bi-Phasic Cu<sub>2</sub>O-Cu Catalyst., Angew. Chem. Int. Ed. 54 (2015) 14701–14705.
10. Dutta, A., Rahaman, M., Luedi, N. C., Mohos, M., Broekmann, P. Morphology Matters: Tuning the Product Distribution of CO<sub>2</sub> Electroreduction on Oxide-Derived Cu Foam Catalysts. ACS Catal. 6 (2016) 3804–3814.
11. Lum, Y. W.; Yue, B. B.; Lobaccaro, P.; Bell, A. T.; Ager, J. W. Optimizing C-C Coupling on Oxide-Derived Copper Catalysts for Electrochemical CO<sub>2</sub> Reduction. J. Phys. Chem. C 121 (2017) 14191–14203.
12. Kas, R., Kortlever, R., Milbrat, A., Koper, M. T. M., Mul, G., Baltrusaitis, J. Electrochemical CO<sub>2</sub> Reduction on Cu<sub>2</sub>O-derived Copper Nanoparticles: Controlling the Catalytic Selectivity of Hydrocarbons. Phys. Chem. Chem. Phys. 16 (2014) 12194–12201.
13. Reske, R., Mistry, H., Behafarid, F., Cuenya, B. R., Strasser, P., Particle Size Effects in the Catalytic Electroreduction of CO<sub>2</sub> on Cu Nanoparticles, J. Am. Chem. Soc. 136 (2014) 6978–6986.
14. Li, Q., Zhu, W. L., Fu, J. J., Zhang, H. Y., Wu, G., Sun, S. H. Controlled Assembly of Cu Nanoparticles on Pyridinic-N Rich Graphene for Electrochemical Reduction of CO<sub>2</sub> to ethylene, Nano Energy 24 (2016) 1–9.
15. Wang, Z. N., Yang, G.; Zhang, Z. R., Jin, M. S., Yin, Y. D., Selectivity on Etching: Creation of High-Energy Facets on Copper Nanocrystals for CO<sub>2</sub> Electrochemical Reduction, ACS Nano 10 (2016) 4559–4564.
16. Kim, D., Resasco, J., Yu, Y., Asiri, A. M., Yang, P. D., Synergistic Geometric and Electronic Effects for Electrochemical Reduction of Carbon Dioxide using Gold-Copper Bimetallic Nanoparticles, Nat. Commun. 5 (2014) 4948.
17. Ezra L. Clark, Christopher Hahn, Thomas F. Jaramillo, Alexis T. Bell, Electrochemical CO<sub>2</sub> Reduction over Compressively Strained CuAg Surface Alloys with Enhanced Multi-Carbon Oxygenate Selectivity, J. Am. Chem. Soc. 139 (2017) 15848-15857.
18. S. Cherevko, S. Geiger, O. Kasian, N. Kulyk, J.-P. Grote, A. Savan, B.R. Shrestha, S. Merzlikin, B. Breitbach, A. Ludwig, K.J. Mayrhofer, Oxygen and hydrogen evolution reactions on Ru, RuO<sub>2</sub>, Ir, and IrO<sub>2</sub> thin film electrodes in acidic and alkaline electrolytes: a comparative study on activity and stability, Catal. Today 262 (2016) 170-180.
19. Kou, R., Shao, Y., Mei, D., Nie, Z., Wang, D., Wang, C., Viswanathan, V.V., Park, S., Aksay, I.A., Lin, Y., Wang, Y., Liu, J, Stabilization of electrocatalytic metal nanoparticles at metal-metal oxide-graphene triple junction points, J. Am. Chem. Soc. 133 (2011) 2541-2547.

20. Ferdinand Hof, Alessandro Boni, Giovanni Valenti, Kai Huang, Francesco Paolucci, Alain Penicaud, From Food Waste to Efficient Bifunctional Nonprecious Electrocatalyst, *Chem. Eur. J.* 23 (2017) 15283-15288.
21. Ferdinand Hof, Alain Penicaud, Graphenide Solutions: A Chemical Platform for Nanoparticle–Nanocarbon Composites, *Chem. Eur. J.* 24 (2018) 1–6.
22. George Bepete, Ferdinand Hof, Kai Huang, Katerina Kampioti, Eric Anglaret, Carlos Drummond, Alain Pénicaud, "Eau de graphène" from a KC8 graphite intercalation compound prepared by a simple mixing of graphite and molten potassium, *Phys. Status Solidi RRL* 10 (2016) 895–899.
23. Conductive inks of graphitic nanoparticles from a sustainable carbon feedstock Ferdinand Hof, Katerina Kampioti, Kai Huang, Christèle Jaillet, Alain Derré, Philippe Poulin, Hisham Yusof, Thomas White, Krzysztof Koziol, Catharina Paukner, Alain Pénicaud, *Carbon* 111 (2017) 142-149.
24. ICSD #63281
25. ICSD #15455
26. Mark C. Biesinger, Advanced analysis of copper X-ray photoelectron spectra, *Surf. Interface Anal.*, 49 (2017) 1325–1334.
27. Jaggi, H., Oswald, H.R., Die Kristallstruktur des Kupferhydroxids,  $\text{Cu}(\text{OH})_2$ , *Acta Crystallographica* 14 (1961) 1041-1045.
28. Restori, R.;Schwarzenbach, D., Charge density in Cuprite,  $\text{Cu}_2\text{O}$ , *Acta Crystallographica B* 42 (1986) 201-208.
29. Trasatti, Real Surface area measurements, *J. of Electroanal. Chem.* 327 (1992) 353-376.
30. Wei Zhe Teo, Adriano Ambrosi, Martin Pumera, Direct electrochemistry of copper oxide nanoparticles in alkaline media, *Electrochem. Comm.* 28 (2013) 51–53.
31. Shaojun Dong, Yuanwu Xie, Guangjin Cheng, Cyclic voltammetric and spectroelectrochemical studies of copper in alkaline solution, *Electrochimica Acta* 37 (1992) 17-22.
32. Yangchun Lan, Sichao Ma, Jiaying Lu, Paul J.A. Kenis, Investigation of a Cu(core)/CuO(shell) Catalyst for Electrochemical Reduction of  $\text{CO}_2$  in Aqueous Solution, *Int. J. Electrochem. Sci.* 9 (2014) 7300-7308.
33. Marcel Pourbaix, *Atlas of Electrochemical Equilibria in Aqueous Solutions*, Pergamon, New York, 1966.
34. Alejandro J. Garza, Alexis T. Bell, Martin Head-Gordon, Is Subsurface Oxygen Necessary for the Electrochemical Reduction of  $\text{CO}_2$  on Copper?, *J. Phys. Chem. Lett.* 9 (2018) 601–606.

# APPENDIX

## Appendix Chapter 1

### A.1.1 Electrodes preparation

Electrodes were prepared by depositing CeO<sub>2</sub> onto BDD and glassy carbon electrodes. Deposition of CeO<sub>2</sub> was carried out in two-compartment cells. The working electrodes and a Pt wire counter electrode were placed in the main cell compartment, a Saturated Calomel Electrode (SCE) in the lateral compartment. Voltammeteries were performed in the same cell. Electrochemical experiments were performed with an Autolab PGSTAT 302N potentiostat. Solutions used to study the deposition of CeO<sub>2</sub> range from 0.4 mM to 0.1 M Ce(NO<sub>3</sub>)<sub>3</sub>, with or without 0.1M NaNO<sub>3</sub>. The solution used for the deposition of CeO<sub>2</sub> for samples used in electrocatalysis was: 0.004 M Ce(NO<sub>3</sub>)<sub>3</sub>, 0.1M NaNO<sub>3</sub>.

The boron doped polycrystalline diamond films were grown on p-type (111) silicon wafers (Furuya metal Co.) using a commercial microwave plasma-assisted chemical vapour deposition (MP-CVD) method with commercial microwave plasma reactors (Model AX6500 and AX5400, CORNES Technologies Corp.). The substrates were pre-treated by abrading with diamond powder (~ 1 μ, Kemet corp.), and were then washed with ultrasonication in distilled water and in isopropyl alcohol. Methane and trimethoxyborane (B(OCH<sub>3</sub>)<sub>3</sub>) were used as main carbon and boron sources. The vapor of the liquid mixture of them was introduced into the reactor with bubbling hydrogen. Boron-to-carbon (B/C) ratios in the gas phase were controlled according to Raoult's law. The individual vapor pressure for each chemical component in the mixed solutions is given by:

$$P_i = P_i^* \times \chi_i$$

where  $P_i$  is the partial pressure for each component,  $P_i^*$  is the vapor pressure of the pure component and  $\chi_i$  is the mole fraction of the component in solution. B/C is varied from 0.1 to 5% by appropriate mixing ratios of the liquid source. The microwave power and deposition pressure were 5000 W and 16.0 kPa (120 torr), respectively. Deposition time for films with B/C up to 1% was 6 h.

### A.1.2. Characterization techniques

SEM images and EDS analyses were obtained with a Zeiss SIGMA instrument, equipped with a field-emission gun, operating under high vacuum conditions, at an accelerating voltage variable from 5 to 30 keV, depending on the observation needs. X-Ray diffraction (XRD) patterns were obtained by using a Philips X-PERT PW3710 diffractometer with a Bragg-Brentano geometry, employing a CuK $\alpha$  source (40 kV, 30 mA). High Resolution Transmission Electron Microscopy (HRTEM) and High-Angle Annular Dark-Field Scanning TEM (HAADF-STEM) were performed on a JEOL JEM-2200FS microscope, working at 200 kV. Elemental maps were obtained by energy dispersive X-ray spectroscopy (EDXS). X-ray photoelectron spectroscopy (XPS) characterization was performed using a JPS-9000 MC (JEOL) equipped with a Mg K $\alpha$  line source.

### A.1.3 Electrochemical Cell for the study of CO<sub>2</sub>RR

Electrolysis were performed in CO<sub>2</sub> saturated 0.1M carbonate buffer (CB) solution prepared with 0.1M KHCO<sub>3</sub> (pH=6.8). Analyses of the products were performed by means of a Metrohm model 850 Professional IC Ion Chromatograph equipped with a conductivity detector. CB was pre-electrolyzed to avoid electrode poisoning from contaminants.

Electrolysis were performed in a custom-made three electrodes electrochemical cell specifically designed and realized in the facilities of the “Centre de Recherche Paul Pascal” (CRPP) in Pessac (France) thanks to a long-standing collaboration between the EMFM group in Bologna and the research group of Dr. Alain Penicaud in that institution.

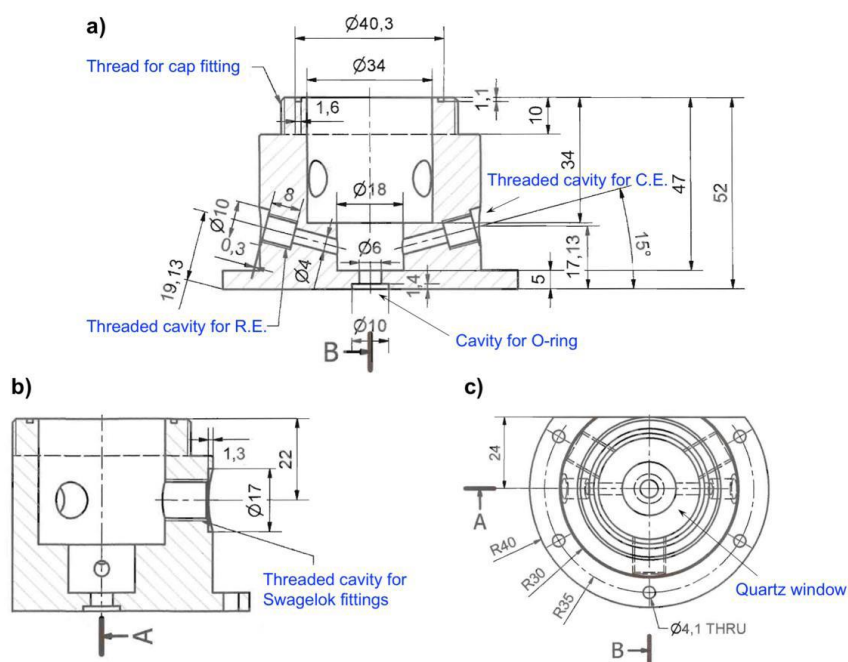


**Figure A.1:** Front, **a)**, lateral **b)** and top **c)** views of the electrochemical cell. **d)** 3D rendering of the electrochemical cell, with highlighted the main components. The working electrode is not visible, but the interchangeable basal plate can accommodate planar SPE as well as rod-like electrodes with  $\varnothing = 6$  mm. The drawings are not in scale.

As can be seen in Fig. **A.1**, the cell presents two threaded cavities near the bottom of the main body, where the R.E. and the C.E. can be accommodated. Both electrodes are placed into glass tubes and isolated from the electrolytic solution with medium size porous frits. To ensure the gas-tightness at the electrode-cell body junction, Teflon or Viton O-rings are placed around the glass tubes and fitted into PEEK nut connectors (Upchurch Scientific Ltd.) which are screwed directly into the body of the cell.

A peculiar characteristic of the cell is also the bottom part, that consists of circular interchangeable adapters into which different W.E. can be placed. These adapters are tightened with 6 screws to the main body and allow to use different W.E. with different geometries. In this work only BDD sheet electrodes have been used, but commercial SPEs and in general plane electrodes, can be used as well. The top of the cell is closed with a cap that is screwed on the main body. Two Viton sealing are placed between the cell and the cap to avoid the escape of gases. Connection with the gas line from the cylinders ( $N_2$  or  $CO_2$ ) is assured by two Swagelok stainless steel connectors, that also in this case are screwed into the main body and have Viton O-rings to prevent gas leaks.

## Appendix Chapter 2

### A.2.1. Preparation and characterization of catalysts

Catalysts were prepared by depositing Pt,  $CeO_2$  or both onto Fe-Cr-Al foams (commercial name Fecralloy, purchased from Porvair, Metpore). Preliminary studies were made using 0.05 mm thick Fecralloy sheets. Foams and sheets consisted of alloys with very similar compositions, close to: Fe 70; Cr 21; Al 9 % (mass). The foams had 50 pores per linear inch,  $0.34 \text{ g cm}^{-3}$  apparent density, ca. 95% void volume, and approximate diameters of struts and pores  $1.0 \times 10^{-2}$  cm and  $5.5 \times 10^{-2}$  cm, respectively. Before use, both sheets and foams were successively washed with dichloromethane, acetone, water, and dried with a nitrogen stream. Sheet electrodes were 1.0 cm x 1.0 cm squares. Fecralloy cylinders (1.8 cm diameter and  $2.3 \pm 0.05 \text{ cm}^3$  volume) used in the preparation of catalysts were waterjet cut from large foam samples, 0.9 cm thick.

Pt and  $CeO_2$  were sequentially deposited onto Fecralloy foam cathodes, under the following conditions:

- I. Pt nanoparticles were deposited from  $\text{H}_2\text{PtCl}_6$  solutions containing 1.0 M NaCl and HCl to yield pH 2.0, by pulsing the cathode potential between two values,  $E_1$  causing Pt deposition and  $E_2$  where no faradaic process occurred [33]. Experimental variables were the  $\text{H}_2\text{PtCl}_6$  concentration, the number of pulses and the  $E_1$  value. Depositions were performed, using an Autolab PGSTAT 302N potentiostat, in a two-compartment cell, with Fecralloy-foam working electrodes, a Pt wire counter electrode and a Saturated Calomel Electrode (SCE) located in a lateral compartment. All potential values refer to SCE.
- II.  $\text{CeO}_2$  was deposited onto Pt-modified foam cathodes, from 0.100 M  $\text{Ce}(\text{NO}_3)_3$ , pH 4.5 to 5.0. Potentiostatic electrolyses caused local pH increase and triggered the precipitation of mixtures of  $\text{Ce}(\text{OH})_3$  and  $\text{CeO}_2$ , entirely converted to  $\text{CeO}_2$  by thermal treatment [33]. The  $\text{CeO}_2$  loading was controlled through the charge transferred during the electrolyses.

Electrodeposition of either  $\text{CeO}_2$  or Pt was carried out in two-compartment cells. The Fecralloy-foam working electrode and a Pt wire counter electrode were placed in the main cell compartment, a Saturated Calomel Electrode (SCE) in the lateral compartment. The solutions used for the deposition of  $\text{CeO}_2$ , similar to those employed by other workers [18-30], were: (i) 0.001 M  $\text{CeCl}_3$ , (ii) 0.001 M  $\text{CeCl}_3$ , 0.020 M  $\text{H}_2\text{O}_2$ , or (iii) 0.100 M  $\text{Ce}(\text{NO}_3)_3$ . Electrolyses were performed at constant potential. Platinum was deposited from 0.002 M  $\text{H}_2\text{PtCl}_6$  solutions containing 1.0 M NaCl and HCl to yield pH 2.0. Electrolyses were performed by pulsing the working electrode potential between  $E_1$ , in the range -0.6 to -1.2 V, inducing Pt electrodeposition, and  $E_2$ , variable between 0.1 and -0.1 V. The number of cycles was varied to control the deposition charge and hence the Pt loading.

Cyclic voltammograms aimed at assessing the Pt surface area were recorded using either Pt-Fecralloy or  $\text{CeO}_2$ -Pt-Fecralloy samples as working electrodes, a Pt wire as counter-electrode and an Hg/HgO/1 M KOH reference electrode. Voltammograms were recorded in 1.0 M KOH, over a potential range where the adsorption/desorption of hydrogen onto/from the Pt surface could be measured with good precision because redox processes due to Fecralloy were negligible. To obtain the Pt surface area, the hydrogen desorption charges were divided by  $190 \text{ C cm}^{-2}$ , i.e. by the hydrogen desorption charge relevant to an ideally flat Pt electrode [36]. Electrochemical experiments were performed with an Autolab PGSTAT 302N potentiostat.

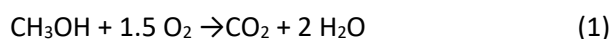
SEM images and EDS analyses were obtained with a Zeiss SIGMA instrument, equipped with a field-emission gun, operating under high vacuum conditions, at an accelerating voltage variable from 5 to 30 keV, depending on the observation needs. Pt loading was determined by microwave-assisted dissolution of Pt-Fecralloy and CeO<sub>2</sub>-Pt-Fecralloy samples in hydrochloric/nitric acid mixtures and analysis of the resulting solution with an ICP-MS Thermo Elemental X7-series mass spectrometer equipped with Plasma Lab software. Multi-element standard solutions for instrument calibration were purchased from Accustandard. X-Ray diffraction (XRD) patterns of Fecralloy sheets electrolyzed in CeCl<sub>3</sub> or Ce(NO<sub>3</sub>)<sub>3</sub> solutions, both as-prepared and after 1-hour thermal treatment in air at 600°C, were obtained by using a Philips X-PERT PW3710 diffractometer with a Bragg-Brentano geometry, employing a CuK $\alpha$  source (40 kV, 30 mA).

#### A.2.2. Methanol combustion tests

The catalytic combustion of methanol over foam catalyst disks (D x L = 1.8 x 0.9 cm) was investigated under dry lean feed conditions (0.5 – 2.0 % vol. in air) using a lab scale test rig already described elsewhere [1]. The reactor was operated at nearly atmospheric pressure, under pseudo-isothermal conditions, by ramping up the temperature with an electric furnace, starting from 50°C, at ca. 3°C min<sup>-1</sup>. Temperatures at the inlet and outlet section of the catalytic foams were measured by 2 K-type thermocouples with their tips in contact with the solid structure. The inlet flow-rate was regulated by mass flow controllers at 40 Sdm<sup>3</sup> h<sup>-1</sup>, corresponding to a Gas Hourly Space Velocity (GHSV) = 16500 h<sup>-1</sup>. Before activity tests, the catalysts were calcined for 2 h in flowing air at 600°C.

The effluent gas was dried and continuously analysed with an ABB Advance Optima2020 and a GEIT FLUE GAS, equipped with ND-IR detectors for CO, CO<sub>2</sub>, CH<sub>4</sub> and an electro-chemical cell for O<sub>2</sub>. In fact the CH<sub>4</sub> detector gave a linear response to methanol, thus it was used to measure its concentration in the feed stream after a specific calibration.

Methanol conversion to CO<sub>2</sub> (yield) through reaction (1) was simply defined as the molar ratio between CO<sub>2</sub> formed (outlet) and methanol in the feed.



Possible by-products at low temperature/conversion, such as formaldehyde (CH<sub>2</sub>O) or methyl formate (CHOOCH<sub>3</sub>), were not measured directly.

The CO<sub>2</sub> production rate was estimated from low conversion data (before rapid ignition,  $\Delta T_{\text{out-in}} < 15^\circ\text{C}$ ) assuming differential conditions, isothermal plug flow reactor, and constant molar flow. Reaction rates were normalized with respect to foam volume and Pt mass, according to equations (2)-(3):

$$R_v \text{CO}_2 \cong \frac{F \cdot y_{\text{CO}_2}}{V_{\text{Foam}}} \quad [\text{mol cm}^{-3} \text{ h}^{-1}] \quad (2)$$

$$R_w \text{CO}_2 \cong \frac{F \cdot y_{\text{CO}_2}}{W_{\text{Pt}}} \quad [\text{mol g}_{\text{Pt}}^{-1} \text{ h}^{-1}] \quad (3)$$

where  $F$  is the total inlet molar flow rate ( $\approx 1.67 \text{ mol h}^{-1}$ ),  $V_{\text{Foam}}$  is the catalyst volume,  $W_{\text{Pt}}$  is the weight of Pt in the foam catalyst and  $y_{\text{CO}_2}$  is the outlet molar fraction of CO<sub>2</sub>. The apparent activation energy of the catalytic deep oxidation was estimated by Arrhenius plots of  $R_v \text{CO}_2$ .

### A.2.3. CO oxidation tests

Catalytic foam cylinders were tested for the oxidation of CO in a lab scale quartz reactor operated at atmospheric pressure [33] by ramping up the temperature with an electric tubular furnace from 100 °C to 600 °C at 3 °C/min. The temperature of the catalyst was measured by two K-type thermocouples (diameter = 0.5 mm) placed in contact with the front and back face of the foam. The fluxes of high-purity gases (CO, O<sub>2</sub>, N<sub>2</sub>) from cylinders were calibrated via Brooks 5850-MFCs. The gases were pre-mixed to give inlet concentrations of CO and O<sub>2</sub> respectively comprised in the ranges 0.25 – 1 % and 5 – 20 % by volume. The CO was cleaned by passing it through an activated-carbon trap to remove eventual metal carbonyls. Some catalytic tests were also performed at fixed preheating and/or using a feed stream pre-humidified at room temperature or comprising 5% vol. of CO<sub>2</sub>. The total inlet flow rate  $Q$  was set at 40 dm<sup>3</sup> h<sup>-1</sup> at standard conditions (unless otherwise specified), corresponding to a Gas Hourly Space Velocity (GHSV) = 17000 h<sup>-1</sup>. Before activity tests, the catalysts were calcined for 2 h in flowing air at 600 °C. The concentration of CO and CO<sub>2</sub> in the product gas stream was continuously analysed with an ABB Advance Optima 2020 instrument equipped with ND-IR detectors.

Separate tests run at fixed temperature levels (not shown) confirmed that CO conversion corresponded to what measured during temperature programmed experiments. Low conversion data (<10%,  $\Delta T^{\text{out-in}} < 5^\circ\text{C}$ ) were used to estimate the catalytic reaction rate per mass of Pt ( $R_w$ ) under the assumption of differential conditions, isothermal plug flow reactor, and constant molar flow, according to equation (1):

$$R_w \cong \frac{Q \cdot y_{CO_2}}{W_{Pt}} \quad [dm^3 g_{Pt}^{-1} h^{-1}] \quad (1)$$

where  $W_{Pt}$  is the mass of Pt in the foam catalyst and  $y_{CO_2}$  is the outlet molar fraction of  $CO_2$ . The apparent activation energy of the catalytic CO oxidation was estimated by Arrhenius plots of  $R_w$ , while the orders of reaction with respect to CO and  $O_2$  were estimated by plots of  $\ln R_w$ , at fixed temperature, vs.  $\ln P_{CO}$  and  $\ln P_{O_2}$ , respectively.

## Appendix Chapter 3

### A.3.1 Cu(np)/nC preparation

All chemicals have been purchased from Sigma Aldrich. THF was purified prior use by means of Pure Solv 400-4-MD solvent purification system that is attached directly to the Glove box. Anhydrous metal chlorides, at least 99.99 % purity, have been obtained from Sigma Aldrich and have been used without further treatment.

#### Synthesis of intercalation compound

120 mg (10.0 mmol) of purified graphitic nano carbon (nC), generated through the plasma splitting of methane,[1] and 48.8 mg (1.25 mmol) cleaned potassium (stoichiometry KC8) were placed together in a vial inside an argon filled glove box and heated for 5 hours at 180°C on a heating plate under occasional stirring. Afterwards, the vial was allowed to cool down to room temperature and the intercalated graphitic nano carbon (KC8) was collected. [23 chapter 3].

#### Dispersion of intercalated nano carbon (KC8) and isolation of the graphenide solution

150 mg of the as prepared intercalated graphitic nano carbon (KC8) were mixed with 150 mL of absolute THF under inert conditions in a 250 mL Erlenmeyer flask and the dispersion was stirred for 1 day by the aid of a glass coated magnetic stirring bar. Then the dispersion was centrifuged at 4500 rpm for 30 min under inert conditions and the faint yellowish upper solution was retained. The concentration of the graphenide solution was determined by dry extracts as  $0.20 \text{ mg/mL} \pm 0.02 \text{ mg/mL}$ .

## Synthesis of the composite compound Cu(nP)/nC

The as prepared graphenide solution has been used directly as reduction agent for the Cu(nP)/nC composite synthesis. Equimolar amounts of recrystallized metal(II) chloride dissolved in 10 mL of absolute THF were added dropwise to 100 mL graphenide solution in a 250 mL Erlenmeyer flask inside an argon filled glove box. After 5-15 min, aggregation and precipitation occurred and the respective dispersion was stirred for 24 hours. Afterwards, the dispersion was removed from the glove box and 100 mL of deionized water was added to the dispersion under ambient conditions. The sample was purified by repeated centrifugation and re-dispersing steps (4 times, 1 h at 10 000 rpm, 15300 g) and the final composite material M(np)/nCs was isolated by freeze drying.

### A.3.2 Characterization

X-ray powder diffraction (XRD). XRD patterns were collected on a Rigaku Nanoviewer (XRF microsourcegenerator, MicroMax007HF), with a 1200W rotating anode coupled to a confocal Max-FluxOsmic Mirror (Applied Rigaku Technologies, Austin, USA) and a MAR345 image plate detector (MARResearch, Norderstedt, Germany); samples were filled into glass capillaries and were exposed to the X-ray beam ; the detector was placed at a distance of 156 mm providing access to  $2\theta$  angles in the range between  $0.9^\circ$  and  $48^\circ$ .

X-ray photoelectron spectroscopy (XPS): A ThermoFisher Scientific K-ALPHA spectrometer was used for surface analysis with a monochromatized AlK $\alpha$  source ( $h\nu = 1486.6$  eV) and a 200 microns spot size. A pressure of  $10^{-7}$  Pa was maintained in the chamber during analysis. The full spectra (0-1150 eV) were obtained with constant pass energy of 200 eV and high resolution spectra at constant pass energy of 40 eV. Charge neutralization was applied for all samples. High resolution spectra were fitted and quantified using the AVANTAGE software provided by ThermoFisher Scientific and the Scofield sensitivity factors available from the internal database.

Transmission electron microscopy (TEM): TEM measurements were performed on a TEM-FEG HR (JEOL2200FS). TEM grids have been prepared by drop casting 20 ml of nanocomposite dispersion in THF directly onto SF400-CU or SF400-NI (for the copper component) TEM grids, silicon monoxide membranes on 400 mesh copper grids (Electron microscopy science). Size statistics have been obtained using a combination of ImageJ (v1.50 b) and Origin 9.2.

### A.3.3. Electrochemical CO<sub>2</sub> reduction

Apparatus and cell used were the same reported in the Appendix of chapter 1. All electrodes were prepared through a drop-cast procedure. Glassy carbon plates, that acts like support electrodes, were polished with a 1 $\mu$ m alumina suspension, accurately rinsed with water and sonicated, after that they were rinsed again with water and acetone and dried. We prepared a suspension in THF with 0.5 mg/mL of Cu(np)/nC material, suspension was repeatedly sonicated before deposition. 300  $\mu$ L of suspension were transferred onto GC plates, with 5  $\mu$ L aliquots, giving a nominally catalyst loading of 150  $\mu$ g that included 15  $\mu$ g of copper. THF was evaporated under mild vacuum conditions.

## ACKNOWLEDGMENTS

First I want to thank Marco that for first, gave me a chance to take a look at scientific research to see if it I liked it...10 years after we can say I definitely did it! And thanks for supporting me during PhD and for deeply reviewing this thesis.

A very big thank to Francesco and Giovanni that let me do this doctoral course experience, in a way that it was never over-stressing (excluding last month of writing!), it was a nice trip full of stimulating conversation and opportunities.

Regarding scientific contributions to this thesis I need to acknowledge Simona Barison for SEM analysis, Lucia Nasi for TEM analysis and Stefano Fasolin for GC analysis. A special mention to Stefano Cimino for its big contribution to the gas phase catalysis part of this work. A special thanks goes also to Prof. Einaga who kindly hosted me in his lab during the couple of months I spent at Keio University and to Dr. Ferdinand Hof for supplying all those nice carbon materials.

I need to thanks my colleagues at ICMATE at all the people I met at Lab2 (they were a lot!) that always let me enjoy the time we spent together.

I want to strongly thank my family and all my friends, they are always there when I need them, and that's the key to overcome troubles we encounter in life.

Finally I need to thank D, for what we shared, for what we will share and because you let me understand that no man is island.

### **'No Man is an Island'**

No man is an island entire of itself; every man  
is a piece of the continent, a part of the main;  
if a clod be washed away by the sea, Europe  
is the less, as well as if a promontory were, as  
well as any manner of thy friends or of thine  
own were; any man's death diminishes me,  
because I am involved in mankind.  
And therefore never send to know for whom  
the bell tolls; it tolls for thee.

*MEDITATION XVII*

*Devotions upon Emergent Occasions*

*John Donne*